# CHAPTER 4
# MATHEMATICAL MODELING OF TWO DIMENSIONAL FLUID FLOW IN A FLEXIBLE TUBE WITH INTERNAL FLEXIBLE LEAFLETS

Dynamics of fluid flow within flexible tube with internal flexible structures has several biological and industrial application as mentioned in chapter 1. In this chapter, the general mathematical formulation of the dynamics involving both solid (i.e. flexible structures) and fluid domains is presented. Then, a specific case study of human veins and the venous valve found in the legs is introduced as an example where this model can be applied.

The organization of the chapter is as follows. Section 4.1 gives a overview of the general model for dynamics of fluid flow within a flexible tube with internal flexible structures, here a pair of leaflets. Next, section 4.2 provides a definition of the problem to be solved. Sections 4.3 and 4.4 develop a mathematical description of the general problem. The case study is introduced in section 4.6. Lastly, section 4.7 summarizes the important contributions of this chapter.

## 4.1 Overview of Fluid Flow in Flexible Tubes with Internal Flexible Structure

The dynamic behavior of Newtonian fluid flow in flexible tubes has been extensively researched [14, 23, 28, 32, 35, 36, 37, 53, 57]. When the wall of a flexible tube undergoes a deformation, the fluid flow within the tube deforms accordingly affecting the local fluid flow properties [21]. In general, flexible structures exhibit anisotropic elastic properties [22]. Previous theoretical and experimental studies by Pedley and co-workers [6, 31, 35, 58], Kececioglu and co-workers [23, 24] and by Wijeratne and Hoo [59] on fluid flow in a collapsible tube show that fluid flow tend to separate due to the collapse of the tube wall alone, which may lead to localized pooling of the

fluid. The presence of an internal flexible structure further promotes conditions for flow separation [41] in addition to modulating fluid flow inside the tube.

With the understanding of the fluid flow behavior in a collapsible channel, this study considers a structure that consists of a *tube* with internal symmetric leaflets where the movements of the leaflets are determined by the magnitude and the direction of the forces acting on them. Thus, the model development integrates the fundamental principles of solid and fluid mechanics to describe the fluid/structure interactions.

The mathematical representation of the system is formulated in a two dimensional framework. Two domains, fluid and solid must be accounted for, and time to represent unsteady behavior. The assumptions include: non-Newtonian fluid flow, laminar fluid flow, and isothermal conditions. Additionally, the analysis will focus on fluid flow behavior at different flow conditions and at different viscoelastic properties. Numerical solutions provide a means of predicting the impact of these variables (i.e. material properties of both fluid and structure) on the overall fluid dynamics. Such insights can provide useful design and performance information to the medical and pharmaceutical industries, material industries, and device manufacturers.

The fluid domain is modeled using momentum and mass conservation principles [21] while the fluid viscosity is described using the concept of a non-Newtonian fluid. The stresses and forces on the flexible structures and the boundary displacements are related by Newton's second law [22]. It follows that the mathematical description of this system involves multi-dimensional fluid dynamics and nonlinear solid mechanics resulting in a system of nonlinear partial differential equations with moving boundaries. To address the non-stationary boundary conditions, an Arbitrary Lagrangian-Eulerian (ALE) formulation is used to represent the governing equations in the fluid domain [2]. Then, the numerical method of finite elements is employed to

find a solution to the ALE formulation [60]. The ALE representation combines the best features of both pure Lagrangian and pure Eulerian approaches. Thus, numerical computation with the ALE formulation succeeds in reducing the computational burden experienced with the pure formulations while capturing the fluid and structural dynamics in the presence of significant distortions.

## 4.2 General Problem Definition

The geometry of the system resembles a flexible tube with two flaps embedded within the tube. Each flap represents a leaflet (see Figure 4.1). Note that the tube diameter is not constant. Specifically, the portion of the tube wall that contains the leaflet expands to provide more space for movement of the leaflets. The free edge of the leaflet protrudes towards the centerline of the tube and in the direction of fluid flow (see Figure 4.1). In general, the leaflets open in the forward direction but only up to a certain distance from the tube wall to represent the fully open position (see top panel of Figure 4.2). The leaflets return to meet in the fully closed position (see bottom panel of Figure 4.2) along the centerline of the tube. The motion of this tube and leaflet system is analogous to the operation of a physical check valve where the leaflets operate under pressure forces.

For the purposes of the mathematical formulation following assumptions are made.

### 4.2.1 Assumptions

- A two-dimensional, lateral cross-section of the tube and the leaflets (see Figure 4.3).
- The assumption of axial symmetry, which simplifies modeling one-half of the cross-section.
- The system operates isothermally.

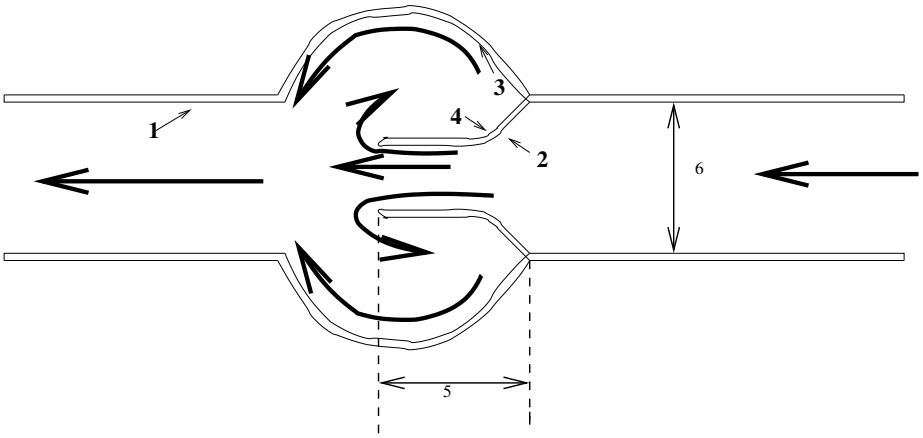


Figure 4.1. Two dimensional schematic of the tube and leaflet. 1. Lumenal surface of tube. 2. Medial surface of the leaflet. 3. Lumenal surface of the leaflet sinus. 4.Lateral surface of the leaflet. 5. Leaflet depth. 6. Tube diameter.

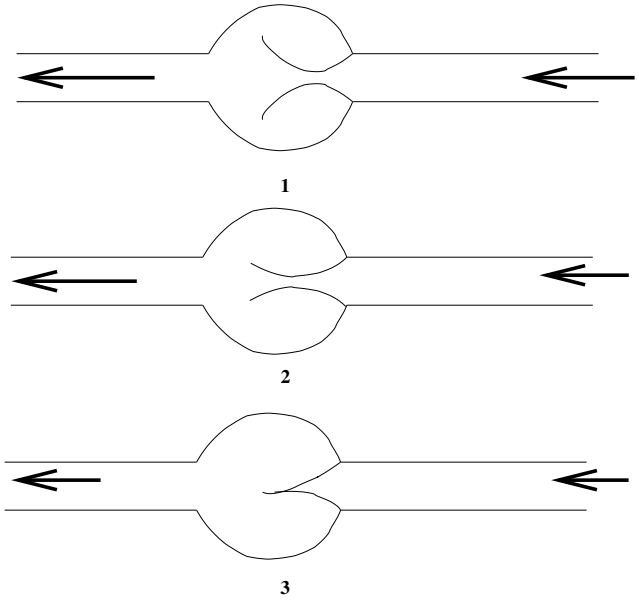


Figure 4.2. Two dimension schematic of 1. open, 2. closing, and 3. closed phases.

- Fluid is non-Newtonian (nonlinear stress-strain relationship) and incompressible.
- The fluid flow is laminar.
- The flexible structures follow a linear stress-strain relationship.
- The material of the flexible structures is ultra-thin so that longitudinal and circumferential bending can be neglected.

The fluid pressure forces and the viscous forces act on the inner tube wall surface and on the leaflet surfaces causing them to move in the direction of the fluid flow. And also when external compression is present, these compressions exert stresses on the outer boundary of the tube wall resulting in tube wall displacement. Depending upon the magnitude of the forces acting upon the tube wall the tube may distend or collapse affecting the cross-sectional flow area. During the opening and closing phases of the leaflets, fluid flow separation at the leaflet tip and fluid re-attachment at the sinus wall also will occur.

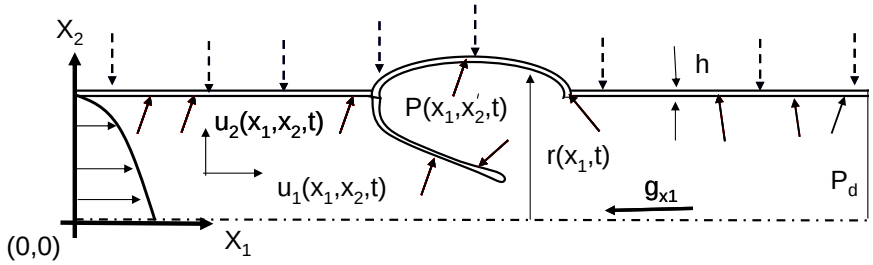


Figure 4.3. Schematic of 1/2 (lateral cross-section) of the tube and leaflet used in formulating the 2-D mathematical model. Solid lines: pressure and viscous forces. Dashed lines: external forces.

## 4.3 Modeling the Fluid Domain

Figure 1.3 provides a guide to the modeling approach used in this section and Figure 4.3 shows the schematic of half (lateral cross-section) of the tube and leaflet

used in formulating the 2-D mathematical model. Fluid dynamics in this system can be described by the conservation of momentum and mass principles. The model development considers the fluid dynamics within the tube, which is in a upright or standing position. Therefore, there is an accounting of the effects of static pressure (due to the fluid column) and dynamic pressure forces. The conservation of fluid momentum in two dimensions is given by,

$$\begin{aligned} &\frac{\partial u_i}{\partial t} + u_i \nabla u_j = -\frac{1}{\rho}\frac{\partial p}{\partial x_i} + g_{x_i} + \frac{1}{\rho}\nabla^2 \mu u_i \qquad i,j = 1,2 \\ &t > 0, \quad 0 < x_1 < L, \quad 0 < x_2 < r(x_1,t) \end{aligned} \tag{4.1}$$

The left hand side of the above equation accounts for the dynamic and convective acceleration of the velocity components. The pressure, gravity, and viscosity effects are represented by the first three terms on the right hand side of the equation. The reader is referred to the nomenclature for the definition of the variables.

The initial and boundary conditions for the Equation 4.1 are as follows.

1. Entrance (i.e. at $x_1 = 0,$ , $0 \le x_2 \le r(0,t)$, $t \ge 0$) to the tube:

   A fully developed parabolic axial velocity $u_1(0,x_2,t)$, and zero radial fluid velocity $u_2(0,x_2,t)$, at the tube entrance, are assumed. Additionally the axial velocity is assumed to be periodic.

$$u_1(0,x_2,t) = U_m(r(0,t) - x_2)(r(0,t) + x_2) \qquad t \ge 0 \tag{4.2}$$

   where $r(x_1,t)$ is the radius of the tube at axial distance $x_1$ and time $t$.

$$U_m = \begin{cases} U_{max} \sin\left(\dfrac{2\pi t}{T_c}\right) & (n-1)T_c \le t \le 0.5(2n-1)T_c, \quad n = 1,2,\ldots \\ 0 & 0.5(2n-1)T_c \le t \le nT_c \end{cases} \tag{4.3}$$

$U_{max}$ is the maximum axial centerline velocity and $T_c$ is the time between opening and closing of the leaflet.

$$u_2(0, x_2, t) = 0 \qquad t \geq 0 \tag{4.4}$$

2. Exit (i.e. $x_1 = L$,$0 \leq x_2 \leq r(L, t)$):

   An exit fluid pressure conditions is prescribed.

$$p(L, x_2, t) = P_d \qquad t \geq 0 \tag{4.5}$$

3. Internal boundary of tube wall (i.e. $0 < x_1 < L$, $x_2 = r(x_1, t)$):

   Fluid velocities at the internal tube wall are assumed to be the same as the rate of the displacement of internal tube wall in the respective directions.

$$u_1(x_1, r(x_1, t), t) = \frac{\partial U}{\partial t} \quad t > 0 \tag{4.6}$$

$$u_2(x_1, r(x_1, t), t) = \frac{\partial V}{\partial t} \quad t > 0 \tag{4.7}$$

   where $U(x_1, x_2, t)$ and $V(x_1, x_2, t)$ are the flexible boundary displacements at spatial coordinates $x_1$ and $x_2$ and time $t$ in the axial and radial directions, respectively.

4. Boundary of the internal flexible leaflet:

   Fluid velocities at the leaflet boundaries are assumed to be the same as the rate

of the displacement of the leaflet boundaries in their respective directions.

$$u_1(x_1, x_2, t) = \frac{\partial U}{\partial t} \quad t > 0 \tag{4.8}$$

$$u_2(x_1, x_2, t) = \frac{\partial V}{\partial t} \quad t > 0 \tag{4.9}$$

where $U(x_1, x_2, t)$ and $V(x_1, x_2, t)$ are the flexible boundary displacements at spatial coordinates $x_1$ and $x_2$ and time $t$ in the axial and radial directions, respectively.

5. Centerline (i.e. at $0 < x_1 < L$ , $x_2 = 0$) :

   Symmetric boundary conditions are assumed.

$$\frac{\partial u_i(x_1, 0, t)}{\partial x_j} = 0 \qquad i, j = 1, 2, \quad t > 0, \tag{4.10}$$

6. Initial conditions ( $0 < x_1 < L$, $0 < x_2 < r(x_1, 0)$):

   Everywhere within the tube both initial axial and radial velocities are assumed to be zero.

$$u_i(x_1, x_2, 0) = 0 \qquad i = 1, 2, \; t = 0, \tag{4.11}$$

The conservation of mass is given by,

$$\rho \nabla u_i = 0 \tag{4.12}$$

$$i = 1, 2 \qquad 0 \leq x_1 \leq L \qquad 0 \leq x_2 \leq r(x_1, t)$$

where $\rho$ is the fluid density.

## 4.4 Modeling the Solid Domain

Figure 1.3 provides a guide to the modeling approach used in this section. The solid domain consists of a flexible tube with two identical flaps (leaflets) embedded within the tube. The tube and the leaflets have different material properties. In a two-dimensional representation, this three-dimensional structure appears as a lateral cross-section of the tube wall with the leaflet's edge attached to the tube wall. As a result of the combined effects of fluid pressure, viscous forces, and external compression, the stresses are induced on the boundaries of these structures. The induced stresses (i.e. normal and shear stresses) are related to the strains in the respective directions by way of their elastic modulus. The strains are estimated by calculating the relative displacements of an infinitesimal continuum. The stress-strain relationships and the displacements are given by,

$$\sigma_{x_1} = E_t \varepsilon_{x_1} \tag{4.13}$$

$$\sigma_{x_2} = E_t \varepsilon_{x_2} \tag{4.14}$$

$$\tau_{x_1 x_2} = E_t \varepsilon_{x_1 x_2} \tag{4.15}$$

$$\varepsilon_{x_1} = \frac{\partial U}{\partial x_1} \tag{4.16}$$

$$\varepsilon_{x_2} = \frac{\partial V}{\partial x_2} \tag{4.17}$$

$$\varepsilon_{x_1 x_2} = \frac{1}{2}\left(\frac{\partial U}{\partial x_2} + \frac{\partial V}{\partial x_1}\right) \tag{4.18}$$

where $E_t$ is the Young's modulus of the tube material; $\sigma$ and $\tau$ are normal and shear stresses, respectively; and $\varepsilon$ is the shear strain.

### 4.4.1 Equations of motion for the tube wall

By considering the forces acting on an infinitesimal continuum of the tube, the relationship between induced stresses, body forces, and the displacements of the continuum are given by,

$$t > 0, \qquad 0 < x_1 < L, \qquad r(x_1, t) < x_2 < h + r(x_1, t)$$

$$\frac{\rho_t d^2 U}{dt^2} = \frac{\partial \sigma_{x_1}}{\partial x_1} + \frac{\partial \tau_{x_1 x_2}}{\partial x_2} + F_{x_1} \tag{4.19}$$

$$\frac{\rho_t d^2 V}{dt^2} = \frac{\partial \tau_{x_1 x_2}}{\partial x_1} + \frac{\partial \sigma_{x_2}}{\partial x_2} + F_{x_2} \tag{4.20}$$

where $F_{x_i}$, $i, j = 1, 2$ is the body force acting on the continuum and $h$ is the thickness of the tube. The terms on the left hand side of the equations represent the rate of change in the momentum of the infinitesimal continuum in the respective directions. The terms on the right hand side of the equations represent the induced normal and shear stresses and the body forces acting on the continuum in their respective directions.

By substituting Equations (4.13) to (4.18) into the above equations, a description of the nodal displacements in the direction of $x_1$ and $x_2$ can be obtained,

$$t > 0, \quad 0 < x_1 < L, \quad r(x_1, t) < x_2 < h + r(x_1, t)$$

$$\frac{\rho_t d^2 U}{dt^2} = E_t \left[ \nabla^2 U + \frac{\partial^2 V}{\partial x_1 \partial x_2} \right] + F_{x_1} \tag{4.21}$$

$$\frac{\rho_t d^2 V}{dt^2} = E_t \left[ \nabla^2 V + \frac{\partial^2 U}{\partial x_1 \partial x_2} \right] + F_{x_2} \tag{4.22}$$

The forces (fluid pressure and viscous forces) acting on the internal boundaries of the

tube and on the leaflet boundaries are given by,

$$\begin{aligned} F_{b_{x_i}} &= A_{x_i}(-p_{x_i} + \left(\nabla(\mu\bar{U})\right)_{x_i} + \left(\nabla(\mu\bar{U})\right)'_{x_i} \qquad i = 1, 2 \\ \bar{U} &\equiv [u_1 \quad u_2]' \end{aligned} \tag{4.23}$$

The boundary and initial and conditions for Equations (4.21) and (4.22) are as follows.

1. Boundaries at both ends of the tube ($x_1 = 0, L$, $r(x_1, t) < x_2 < h + r(x_1, t)$) are fixed in both directions (i.e. zero displacement).

$$U(0, x_2, t) = 0 \tag{4.24}$$

$$U(L, x_2, t) = 0 \tag{4.25}$$

$$V(0, x_2, t) = 0 \tag{4.26}$$

$$V(L, x_2, t) = 0 \quad t \geq 0 \tag{4.27}$$

2. Internal tube wall boundary ($0 < x_1 < L$, $x_2 = r(x_1, t)$):

   The forces acting on the internal tube wall are the sum of the fluid pressure and viscous forces defined by Equation 4.23.

$$F_{x_1}(x_1, r(x_1, t), t) = F_{b_{x_1}} \tag{4.28}$$

$$F_{x_2}(x_1, r(x_1, t), t) = F_{b_{x_2}} \quad t > 0 \tag{4.29}$$

3. External tube wall boundary ($0 < x_1 < L$, $x_2 = h + r(x_1, t)$):

   All flexible tubes that have either biological or industrial applications are subject to periodic distributed compression. This compression can be expressed in the form of a displacement or in terms of an external force. In this study

external compression in the $x_2$ direction is introduced as a periodic distributed displacement. There is no compression in the $x_1$ direction.

$$U(x_1, r(x_1, t), t) = 0 \qquad t > 0 \tag{4.30}$$

$$V(x_1, r(x_1, t), t) = \begin{cases} \delta_{max} \sin\left(\dfrac{2\pi t}{3}\right) G & (n-1)T_c \leq t \leq 0.5(2n-1)T_c, \quad n = 1, 2, \ldots \\ 0 & 0.5(2n-1)T_c \leq t \leq nT_c \end{cases} \tag{4.31}$$

$$G = [x_1(x_1 - L)(x_1 - L - 0.09)(x_1 - L - 0.135)]/[L^4]$$

4. Initial conditions (t=0, $0 < x_1 < L$, $r(x_1, t) < x_2 < h + r(x_1, t)$):
   Initially, there are no stresses or displacements acting on the any of the boundaries of the tube. The initial conditions are given by,

$$U(x_1, x_2, 0) = 0 \tag{4.32}$$

$$V(x_1, x_2, 0) = 0 \tag{4.33}$$

### 4.4.2 Equation for displacements of the leaflet

The axial and the radial displacements of the leaflet can be represented by a set of partial differential equations given by,

$$\frac{\rho_t d^2U}{dt^2} = E_t \left[ \nabla^2 U + \frac{\partial^2 V}{\partial x_1 \partial x_2} \right] + F_{x_1} \tag{4.34}$$

$$\frac{\rho_t d^2V}{dt^2} = E_t \left[ \nabla^2 V + \frac{\partial^2 U}{\partial x_1 \partial x_2} \right] + F_{x_2} \tag{4.35}$$

$$t > 0$$

All boundaries of the leaflet that come in contact with the fluid is subject to the sum of the pressure and viscous forces given by,

$$F_{x_1}(x_1, r(x_1, t), t) = F_{b_{x_1}} \tag{4.36}$$

$$F_{x_2}(x_1, r(x_1, t), t) = F_{b_{x_2}} \tag{4.37}$$

$$t \geq 0$$

Note that all the leaflet boundaries are initially free of displacements.

## 4.5 Numerical Solution

A mathematical description of the flexible tube with two leaflets results in a system of nonlinear partial differential equations with non-static boundary conditions. To solve this system (see Appendix C), finite element numerical techniques with an arbitrary Lagrangian-Eulerian (ALE) [2] formulation is implemented.

In general, a pure Lagrangian formulation, used mainly in structural mechanics, is where each individual node of the computational mesh follows an associated material particle during the deformation. The main disadvantage of this formulation is its

inability to follow large deformations without re-meshing.

In contrast, a pure Eulerian formulation, usually use in fluid mechanics, is where the computational mesh is fixed and the continuum moves with respect to the grid. Even though the Eulerian description can capture large deformations this technique requires very precise interface definition and has a large computational burden.

The ALE formulation capitalizes on the best features of both the Eulerian and Lagrangian formulations while de-emphasizing the disadvantages. Specifically, the ALE formulation not only allows the nodes of the computational mesh to move with the continuum, but also the computational mesh can move in an arbitrarily specified way to give a continuous re-zoning capability. As a result, the ALE formulation can follow large distortions with less computations. In this work, the mathematical model of the fluid domain is defined in the ALE framework; with the solid domain in the Lagrangian framework. Femlab® Multiphysics software, version 3.3a from Comsol Inc., (Stockholm, Sweden) is used to carry out the numerical solution.

### 4.5.1 ALE description of the fluid domain

Since the deformation in the fluid domain can be quite significant as compared to the solid domain, the computational mesh in the fluid domain cannot be held static to capture the dynamic properties of the fluid domain material points. Additionally, the computational procedure also must account for spatial changes to the computational mesh.

In general the conservation of mass and momentum in the fluid domain are defined by the Eulerian formulation (Equations (4.1) and (4.3)) where the fluid velocities are the corresponding material velocities. Thus, the convective velocity is same as the material velocity, $u_i$. Due to deformation of this system, both the material and the computational mesh points are moved relative to a spatial frame. When both material

and mesh points move relative to a fixed spatial co-ordinate system the convective velocity of a material point is the relative velocity of the material point with respect to the mesh velocity.

To accommodate the mesh movement, the convective velocities in Equations (4.1) that coincide with the material velocities are replaced by,

$$c = u_i - \hat{v} \quad i = 1, 2 \tag{4.38}$$

where $\hat{v}$ is the mesh velocity at a fixed mesh point. The difference, $c$, defines the relative motion of the material point with respect to the mesh in the spatial frame of reference. This adjustment requires redefining the conservation of momentum for the fluid,

$$\begin{aligned} &i, j = 1, 2 \qquad t > 0 \qquad 0 < x_1 < L \qquad 0 < x_2 < r(x_1, t) \\ &\frac{\partial u_i}{\partial t} + c\nabla u_j = -\frac{1}{\rho}\frac{\partial p}{\partial x_i} + g_{x_i} + \frac{1}{\rho}\nabla^2 \mu u_i \quad i, j = 1, 2 \end{aligned} \tag{4.39}$$

### 4.5.2 Procedure to solve the fluid and solid models

The numerical solution of the equations that describe the fluid and solid interactions are found using a suitable finite element method. The mathematical description of the solid domain is in the Lagrangian framework while that of the fluid domain is in the ALE framework. The procedure is as follows:

1. Solve Equations (4.39) and (4.3) to determine the spatial fluid properties.

2. Flexible boundary displacements are found by solving Equations (4.21), (4.22), (4.34) and (4.35) using the results of step 1. Note that in the Lagrangian formulation, the individual nodes follow the computational mesh. Thus, the solid domain computational mesh displacements are the same as the nodal displace-

ments.

3. Update the mesh points in the fluid domain using the Laplacian equation, $\nabla(\hat{v}) = 0$.

4. Return to step 1 and repeat for $0 < t < T_\infty$.

## 4.6 Case Study

In this section a case study is presented to demonstrate the use of the models developed previously. Note that a large part of this case study is adapted from [59].

### 4.6.1 Introduction

The flexible tube and the pair of leaflets are analogous to the vein and valve (leaflets) found in legs of humans (see Figure 4.4). Proper blood flow in the veins is important to ensure effective return of deoxygenated blood to the heart. A major element of the human venous system is the presence of one-way, flexible, bicuspid valves in the legs that allow antegrade blood flow while preventing retrograde flow [44]. The venous valve consists of a pair of flexible leaflets, each attached at a single point to the vein wall while their free edges protrude into the lumen of the vein. In normal subjects, these leaflets are crescent shaped.

The veins in legs of humans are said to be thin walled [61], as such these veins may collapse (through the force of external pressure) or distend (swell from internal pressure) or extend (stretch) when vessel wall is subjected to excessive stresses. Blood flow velocity in the veins in the legs is neither turbulent nor as pulsatile when compared to blood velocity in the arteries. Thus, blood flow (hemodynamics) within the human veins is analogous to low Reynolds fluid flow in a flexible channel. Further, it is pointed out that blood is a non-Newtonian fluid.

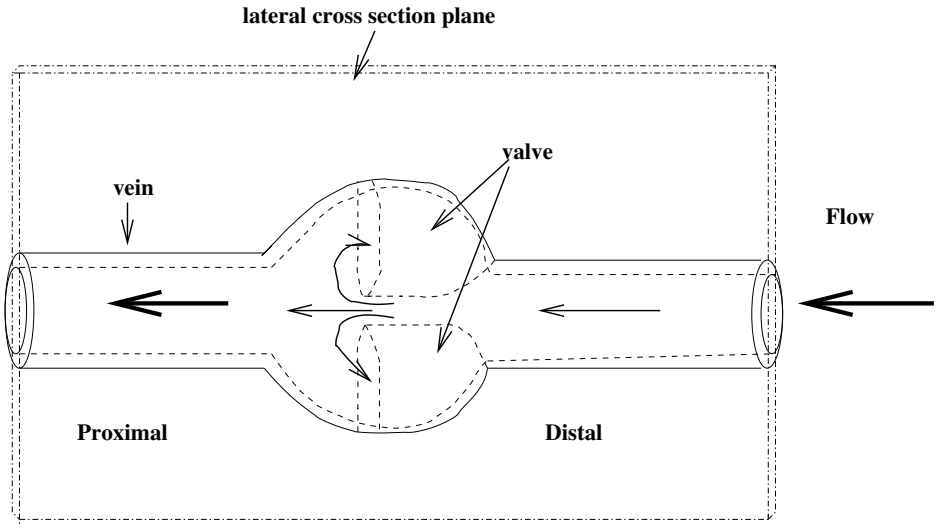


Figure 4.4. Three dimensional schematic of the vein and valve.

Evolution has evolved one-way flexible valves embedded within the vein to assist in venous return (antegrade flow) to the heart. The valve leaflets are attached at two points to the vein, hence they are said to be bicuspid venous valves. The motion of the valves affect the hemodynamics of the venous return. It is well documented that reduced venous blood flow is a strong function of the physiological integrity of the venous valve competence and the muscle-vein pump. The primary objective of this study is to understand the effect of fluid and external forces on the venous valve and vein physiology. To accomplish this objective a two-dimensional computational model of hemodynamic fluid flow within the human venous system will be developed. Accurate models may be able to connect venous system incompetence and changes in fluid flow behavior to the onset of pathophysiological venous limitations.

The competency of the venous system to maintain efficient antegrade flow has been linked to venous diseases. Obviously, a fundamental understanding of this flexible system can provide useful insights to the medical and pharmaceutical communities who treat venous and cardiovascular diseases. Additionally, this study can be used to investigate similar structures such as bronchial air ways, arteries [4, 5, 6] peristaltic

tubes, and micro-fluidic devices [8, 9].

Blood exhibits non-Newtonian fluid behavior, giving rise to spatial variation in the viscosity. Changes in the fluid properties such as viscosity or hematocrit (red blood cell count) have a significant effect on the flow behavior of the fluid. The viscosity of blood depends on many factors including composition, hematocrit volume, plasma viscosity, temperature, and shear rate. In the case of temperature, a healthy subject's body maintains a constant temperature every where thus, it reasonable to assume that blood flow in the venous system operates at isothermal conditions. Hence, local temperature variations can be neglected. Viscous forces together with the fluid pressure impose stresses on the boundaries of the flexible valve and vein wall resulting in continuous displacement of their boundaries.

Two types of viscosity models are used. The first is the model by Carreau where viscosity is defined as a function of shear rate [62]. The second is that of Zydney et al. [63] to emphasize the dependence of viscosity on the volume of red blood cells, shear rate, plasma viscosity, and body temperature [64] at low shear rates ($< 50\ \mathrm{s}^{-1}$). With these parameter dependent viscosity descriptions, the flow patterns behind and in front of the valve leaflets at different operating conditions can be studied.

### 4.6.2 Viscosity models

In general viscoelastic fluids, power fluids, and generalized Newtonian fluids are classified as non-Newtonian fluids [21]. The main feature of a generalized Newtonian fluid is that the shear stress is a function of the shear rate at that time and is independent of the history of the deformation. Two types of viscosity models are used in the model development. The first is Carreau's model [62] where viscosity is a function of the shear rate. The second, contains the dependency of viscosity on the constituents in the fluid. When the fluid is blood, the viscosity at low sheer rates is

a function of the percent of red blood cells and plasma viscosity, which is a function of the body's temperature [63].

#### 4.6.2.1 *Carreau viscosity model*

Blood viscosity ($\mu$) is given by,

$$\mu(\dot{\gamma}) = \mu_o \left(1 + (\lambda\dot{\gamma})^2\right)^{\frac{n-1}{2}} \tag{4.40}$$

where the parameters $\{\mu_o, n, \text{and } \lambda\}$, are material properties of the fluid and $\dot{\gamma}$ is the shear rate defined by,

$$\dot{\gamma} = \frac{\partial u_1}{\partial x_2} + \frac{\partial u_2}{\partial x_1} \tag{4.41}$$

#### 4.6.2.2 *Viscosity model at low shear rates*

At low shear rates, the percent solids (e.g. red blood cells) present in the fluid and the viscosity of the fluid (e.g. plasma) affect the overall fluid viscosity. Quemanda [65] provides a constitutive equation for blood viscosity using the principle of minimum energy dissipation,

$$\mu = \mu_f \left(1 - \frac{k}{2}C\right)^{-2} \tag{4.42}$$

$$k = \frac{k_o + k_\infty \left(\frac{\dot{\gamma}}{\dot{\gamma}_c}\right)^{0.5}}{1 + \left(\frac{\dot{\gamma}}{\dot{\gamma}_c}\right)^{0.5}} \tag{4.43}$$

where $\dot{\gamma}_c$ is the critical shear rate and the parameters, $\{k_o, k_\infty, \dot{\gamma}_c\}$ are functions of the percent hematocrit ($C$).

An extensive correlation between the percent hematocrit ($C$) and the parameters,

$\{k_o, k_\infty, \dot{\gamma}_c\}$ has been developed by [66],

$$k_o = \exp(3.874 - 10.41C + 13.8C^2 - 6.738C^3) \tag{4.44}$$

$$k_\infty = \exp(1.3435 - 2.803C + 2.711C^2 - 0.6479C^3) \tag{4.45}$$

$$\dot{\gamma}_c = \exp(-6.1508 + 27.923C - 25.6C^2 + 3.697C^3) \tag{4.46}$$

The plasma viscosity ($\mu_f$) is given by [67] ,

$$\mu_f = \mu_{37} \exp\left[\eta(37 - T)\right] \tag{4.47}$$

where $\mu_{37}$ is a reference plasma viscosity at 37°C, and $\eta$ is a temperature coefficient.

### 4.6.3 Adaptation of the general model to the vein and valve system

Referring to both solid and fluid domain boundary conditions in the general case, it is reasonable to use the same conditions but with relevant parameter values that pertain to the vein and valve system.

#### 4.6.3.1 *Fluid domain*

1. Internal vein wall surface and the boundaries ( i.e. surface) of the valve are subject to the sum of the pressure and viscous forces exerted by blood.

2. In general vein contains multiple valves leading to segmentation of the vein. The differences in the valves opening and closing frequencies causes periodic flow of blood to each segment of the vein.

4.6.3.2 *Solid domain*

1. In general, periodic muscle expansion and contraction in the human body imposes certain periodic displacements in the vein wall. Also due to the non-uniform structure of the muscle, the compression on the vein segment may not be uniform leading to non-uniform compression of the vein wall. Thus, it is reasonable to assume that the applied external compression is periodic function.

## 4.7 Summary and Contribution

A model for a two-dimensional mathematical representation of the flexible tube and flexible leaflet system is developed considering the fluid and solid domains that comprise this system. The fluid domain assumes non-Newtonian fluid properties and the solid domain assumes linear elastic properties. The motion of the leaflet and the tube wall introduces non-stationary boundary conditions. To address this issue, a numerical formulation of the fluid domain using an Arbitrary Lagrangian-Eulerian ALE framework is used to re-formulate the Eulerian model of the fluid domain while a Lagrangian frame work is used to model the solid domain. The human vein and valve system is used to demonstrate the validity of the model.

The primary contribution of this work as follows.

- A two-dimensional mechanistic PDE model is derived to represent fluid flow in the flexible tube and flexible leaflets using the conservation of mass and momentum principles.

- The motion of the flexible valve leaflet and vein wall introduce non-stationary system boundaries.

- The fluid domain is modeled using an ALE frame work to provide an accurate numerical solution while tracking the moving boundaries.

- Two viscosity models are used to represent the complex stress-strain relationship of the fluid.

## 4.8 NOMENCLATURE

| | |
|---|---|
| $C$ | Hematocrit percentage |
| $E$ | Young's Modules of the material $(Pa)$ |
| $F_{b_{x_i}}$ | Fluid forces acting on the flexible structures for directions $i = 1, 2$ $(Pa)$ |
| $F_{x_i}$ | Body forces acting on the flexible structure for directions $i = 1, 2$ $(Pa)$ |
| $L$ | Length of the tube $(m)$ |
| $P_d$ | Down stream exit fluid pressure $(Pa)$ |
| $T$ | Temperature $(C^\circ)$ |
| $T_c$ | Cycle duration $(s)$ |
| $U$ | Displacement in axial direction $(m)$ |
| $U_{max}$ | Maximum axial velocity at entrance $(m/s)$ |
| $V$ | Displacement in radial direction $(m)$ |
| $c$ | Relative convective velocity of the material in spatial domain $(m/s)$ |
| $g_{x_i}$ | Fluid gravitational force $(Pa)$ |
| $h$ | Thickness of the flexible tube $(m)$ |
| $p(x_1, x_2, t)$ | Fluid pressure $(Pa)$ |
| $r(x_1, t)$ | Radius of the tube $(m)$ |
| $t$ | Time $(s)$ |
| $u_1(x_1, x_2, t)$ | Axial fluid velocity $(m/s)$ |
| $u_2(x_1, x_2, t)$ | Radial fluid velocity $(m/s)$ |
| $x_1$ | Axial coordinate $(m)$ |
| $x_2$ | Radial coordinate $(m)$ |
| $\dot{\gamma}$ | Fluid shear rate $(s^{-1})$ |
| $\dot{\gamma}_c$ | Critical Shear rate $(s^{-1})$ |
| $\delta_{max}$ | Maximum displacement of the tube $(m)$ |
| $\varepsilon_{x_i}$ | Material shear strain |
| $\varepsilon_{x_i}$ | Material strain in $i$ direction , for i=1,2 |

| | |
|---|---|
| $\eta$ | Temperature coefficient $(1/C^{\circ})$ |
| $\mu$ | Dynamic blood viscosity $(Pa/s)$ |
| $\mu_f$ | Plasma viscosity $(Pa/s)$ |
| $\mu_o$ | Constant fluid dynamic viscosity $(Pa/s)$ |
| $\mu_{37}$ | Plasma viscosity at 37° C$(Pa/s)$ |
| $\rho$ | Fluid density $(Kg/m^3)$ |
| $\rho_s$ | Material density of the flexible structure$(Kg/m^3)$ |
| $\sigma_{x_i}$ | Material stress in $i$ direction , for i=1,2 $(Pa)$ |
| $\tau_{x_1x_2}$ | Material shear stress $(Pa)$ |

# CHAPTER 5
# NUMERICAL SOLUTION OF THE VEIN AND VALVE SYSTEM

Femlab® Multiphysics software, version 3.3a from Comsol Inc. (Stockholm, Sweden), is used for numerical simulations. The parameter valves are given in Table 5.2. A cast of a cadaver vein and valve is used to estimate the geometric parameters of the system. A Matlab program is written using the Mathworks (Natick, MA) Matlab © image analysis toolbox version 7.0.1 to estimate the geometric dimensions of the valve and the vein (see Appendix D). The dimensions are verified using calipers at corresponding locations on the cast.

## 5.1 Estimation of geometric parameter values for vein and the valve

The geometric parameters of the vein and valve system are estimated from the images of a cast of a harvested cadaver vein made by [68]. The harvested cadaver vein is just filled with room temperature vulcanizing ($RTV$) silicone to fill the vein without excess stretching and expansion. The filled vein is placed in a normal saline solution to prevent desiccation. After twenty-four hours, the cast has solidified; the cadaver vein is removed by cutting it away from the cast. From the cast it is possible to (see Figure 5.1) see the demarcation of the valve leaflet positions. Images of the cast are taken using a 7.2 Mega pixel digital camera. All images are taken with a metric scale next to the cast so that both scale and cast are in a same focal plane. The metric scale is used to calibrate the pixel distance to physical distance units. Using custom code written for Matlab's© image toolbox, the geometric dimensions of the valve and the vein are estimated.

First, the image captured by the digital camera is converted to a binary image. Next the edges of the image are detected using the *Sobel* edge detection technique


Figure 5.1. Cast of a harvested cadaver vein and valve. Note, the valve leaflets are numbered and marked with black ink to emphasize their location.

[69]. The principle of Sobel edge detection technique locates where discontinuities of the pixel values exist. These discontinuities in the pixel values are detected by estimating the first derivative of the pixel values in the horizontal (x) and vertical (y) directions. Once the edges of the vein and valve are detected (see Figure 5.2), the pixel distances between the edges are estimated. The metric scale in the image is used to determine the resolution. From the image resolution, physical dimensions of the object can be determined from the number of pixels between the feature being measured, e.g. the edges of the diameter. In the image shown in Figure 5.1, 120 pixels correspond to 1 cm, thus the resolution of the image is 0.0083 $cm/pixel$. Pixel distances are converted to standard distance units by multiplying the number of pixels by the resolution. Table 5.1 lists the estimated average values and the corresponding standard deviation for a total of n=3 valves shown in Figure 5.1. These estimated values are within the agreement of the calliper measurements.

## 5.2 Numerical simulation

The fluid and solid domain governing equations for the vein and valve system are solved by applying a finite element numerical method. Here, the fluid velocities and

Table 5.1. Geometric parameter values.

| Parameter | Value (mm) | Mean (mm) | Stand. Dev. (± mm) |
|---|---|---|---|
| Vein diameter: distil | 9.5 | 9.5 | 0.5 |
| Vein diameter: proximal | 8.65 | 9.8883 | 1.173 |
| Valve depth | 14 | 14 | 1 |
| Sinus height | 7.7 | 7.733 | 1.702 |

Table 5.2. Model parameter values [62, 63, 67, 70].

| Description | Variable | Value | Units |
|---|---|---|---|
| Tube length | $L$ | 0.18 | m |
| Tube inlet radius | $r(0,t)$ | $4.0\times10^{-3}$ | m |
| Leaflet depth | $d_s$ | 0.015 | m |
| Fluid density | $\rho$ | 1060 | $Kg/m^3$ |
| Inlet max axial velocity | $U_{max}$ | 0.4 | m/s |
| Exit fluid pressure | $P_d$ | 1000 | Pa |
| Fluid dynamic viscosity | $\mu_o$ | $2.2\times10^{-3}$ | Pa/s |
| Tube material density | $\rho_t$ | 960 | $Kg/m^3$ |
| Leaflet material density | $\rho_s$ | 500 | $Kg/m^3$ |
| Tube thickness | $h$ | $5\times10^{-4}$ | m |
| Leaflet thickness | $h_s$ | $2.5\times10^{-5}$ | m |
| Young's Modulus- tube | $E_t$ | $3.3\times10^{6}$ | Pa |
| Young's Modulus- leaflet | $E_s$ | $15\times10^{6}$ | Pa |
| Tube max displacement | $\delta_{max}$ | $2.5\times10^{-4}$ | m |
| Plasma viscosity at $37°C$ | $\mu_{37}$ | $1.4\times10^{-3}$ | Pa/s |
| Temperature coefficient | $\eta$ | 0.021 | $°C^{-1}$ |
| Temperature | $T$ | 28 | $°C$ |
| Cycle duration | $T_c$ | 3 | s |

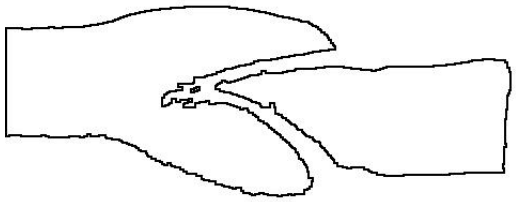

Figure 5.2. Vein and valve edges extracted from the image

the solid domain displacements are expressed using quadratic shaped functions while the fluid pressure is expressed using linear shaped functions. For numerically accurate and convergent results, it is important to guarantee that the computational mesh is less distorted at each successive solution step. When moving objects are present in the computational domain, the Comsol support [1] suggests using a sectioned domain and meshing the individual sections such that the number of nodal points are matched along the sectional boundaries. This technique allows control of the individual mesh deformation. In this model, the number of nodal points along the section and external boundaries are pre-prescribed to control the number of mesh elements in each section. This approach resulted in both triangular and quadrilateral mesh elements. Table 5.3 lists the mesh statistics of the base model.

Table 5.3. Mesh statistics.

| Parameter | Value |
|---|---|
| Number of mesh elements | 2797 |
| Number of triangular elements | 260 |
| Number of quadrilateral elements | 2537 |
| Solution time | 8 minutes |

Simulation results with refined number of mesh elements are carried out to in-

[1]Solution No :970, "Improving convergence for ALE and parameterized geometry." http://www.comsol.com/support/knowledgebase/970/.

vestigate the quality of the results. In this case the number of mesh elements has been increased to 3524 (26%) at the expense of total solution time of 15 minutes (almost doubled). The results obtained using the refined mesh model (not shown here) estimates a 6% increase in the maximum displacement of the leaflet free edge when compared to base case model. A comparison between the fluid domain solution with the refined mesh and the solution from the base case yield numerically less significant values (changes are in the range of 1%-4%). In general, the simulation results obtained with the base case model are better able to produce results that more closely match (discussed in the proceeding sections) the in vivo results reported by Lurie et al. [41]. Infinite mesh refinement is not possible when large deformations are present. If the deformations become too large, some of the mesh elements may become inverted. This affects the accuracy of the solution and eventually the solution will cease to converge.

## 5.3 Results and Analysis

### 5.3.1 Results: Baseline

The fluid flow dynamics and solid mechanics pertaining to the base case is presented first.

#### 5.3.1.1 *Fluid flow dynamics*

Figures 5.3 to 5.6 show the streamline patterns during a single cycle at different phases of the closing to opening cycle when the tube segment is in a vertical position. From these figures, one can observe the formation and break away of the vortices at the leaflet edge during the opening, equilibrium and closing phases of the cycle. This analysis is carried out by employing the second viscosity model with a hematocrit value of 30% solids.

The duration of one complete cycle is about 3.0 seconds. The closed phase lasts

about 0.2 seconds, the opening phase about 0.3 seconds, the equilibrium phase is about 1.5 seconds, and the closing phase is about 1 second. The durations of the opening and equilibrium phases are in satisfactory agreement with the in vivo studies of [41]. However, the duration of the closing and closed phase are different. The duration of the closed phase is reduced by 80% and and that of the closing phase has increased by about 75% when compared to the reported results of Lurie et al. [41]. These differences are attributed to the parameter values used in the model as well as the frequency of the external compression. In spite of these timing differences, the model is able to capture the fluid dynamics of the vein and venous valve system confirming the formation of vortices that modulate the leaflet motion.

Figure 5.7 shows the axial velocity profile in the open phase. It can be seen that a higher fluid velocity exists in between the leaflets due to the small flow area. Additionally inside the leaflet (or valve sinus) the fluid velocity is much less compared to anywhere else in the fluid domain. This lower fluid velocity results from vortex formation inside the sinus. The corresponding Reynolds number distribution is given in Figure 5.8. This result confirms a low Reynolds number flow.

Figures 5.9 and 5.10 show the fluid velocity patterns at different axial positions at the center line. These results indicate the periodic nature of the fluid velocity. The range of the approximate maximum centerline axial fluid velocities at the distal end, between the leaflets, and at the proximal end are listed in Table 5.4. These values are in the range reported by [41].

Panels on Figures 5.11 and 5.12 show the fluid pressure distribution around the leaflet and also at proximal and distal sides of the tube during different times of the leaflet cycle. It has been observed that during the open and opening phases the pressure around the leaflet is about 10% to 20% higher than the pressure distribution around the leaflet during close and closed phases. The arrow lines indicates the fluid

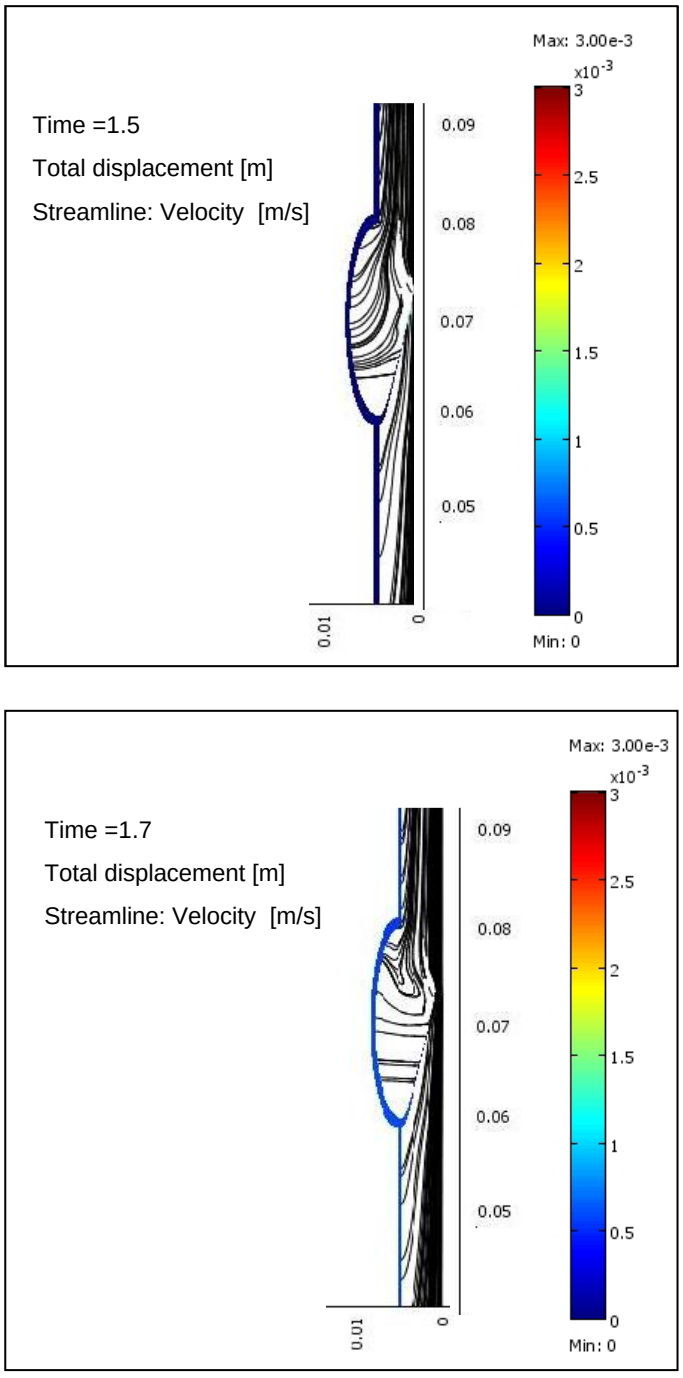


Figure 5.3. Fluid streamlines during the closed phase of the cycle. Top: time = 1.5. Bottom time = 1.7. Scale on the right represents displacement. Abscissa: Diameter of tube in meters. Ordinate: Length of tube in meters.

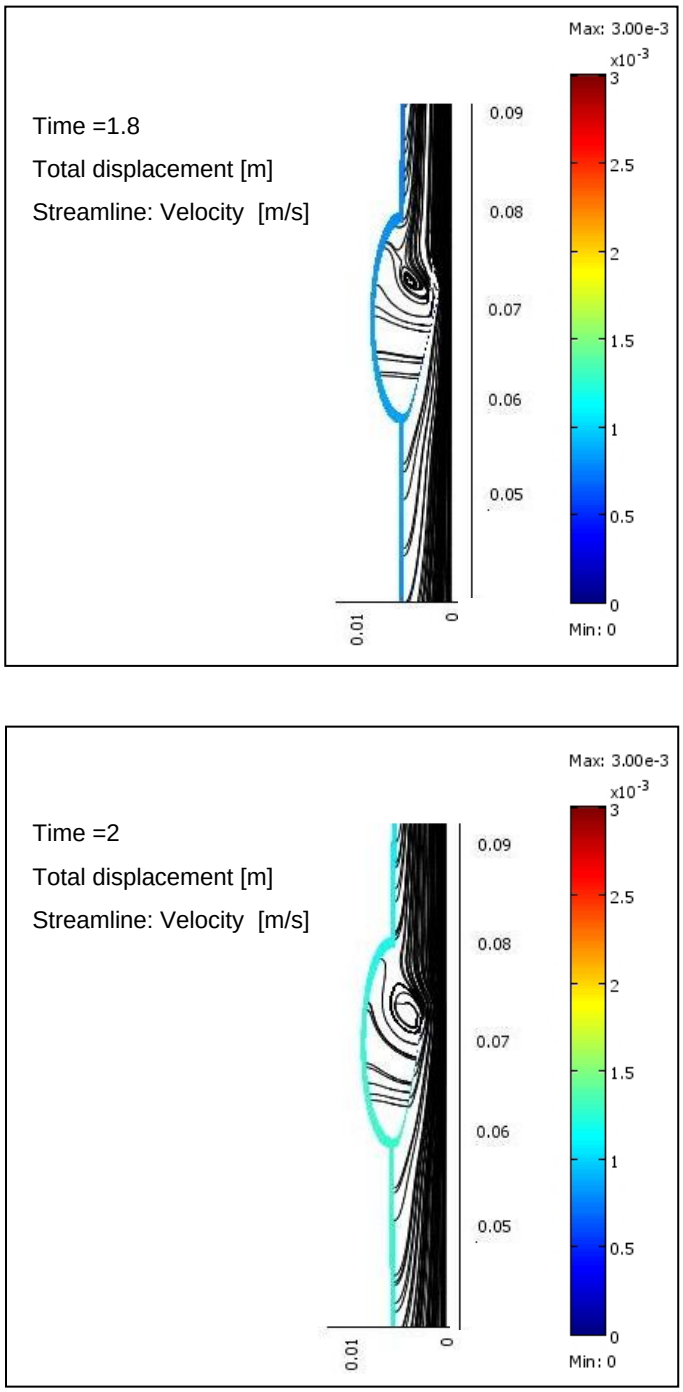


Figure 5.4. Fluid streamlines during the opening phase of the cycle. The scale on the right represents displacement. Abscissa: Diameter of tube in meters. Ordinate: Length of tube in meters.

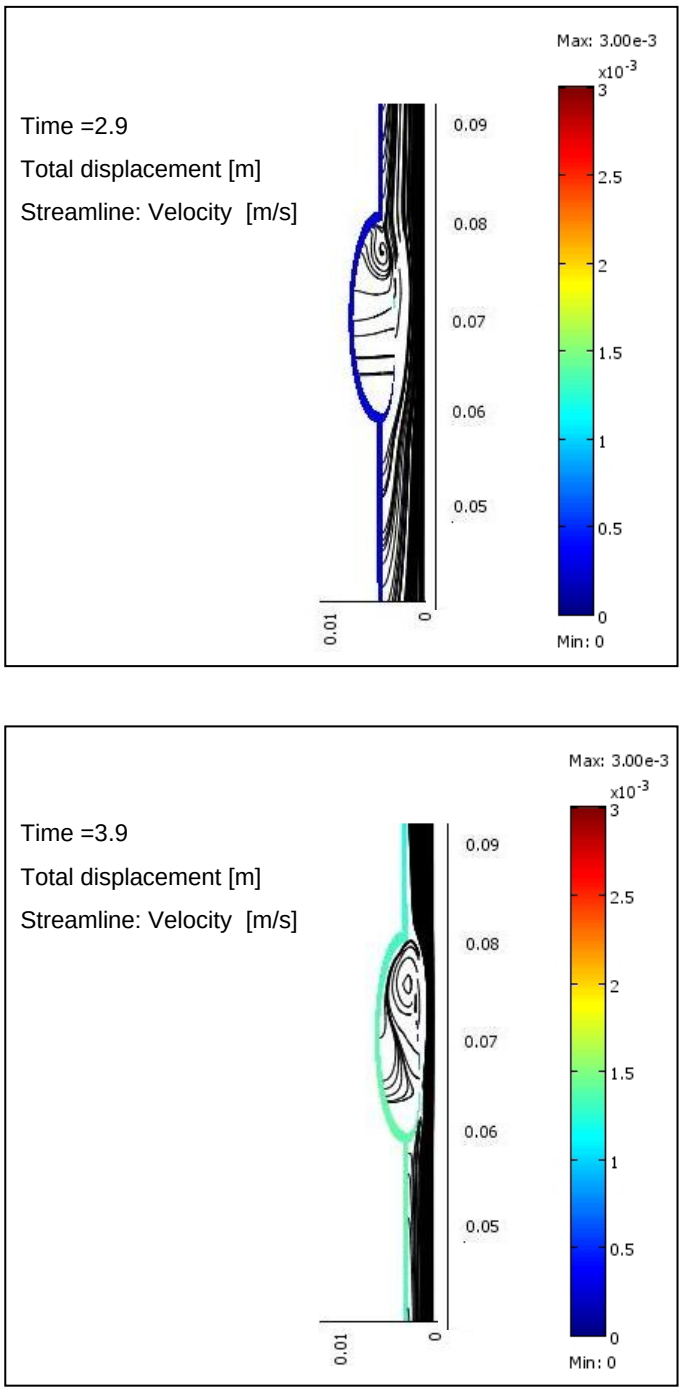


Figure 5.5. Fluid streamlines during the equilibrium phase of the cycle. The scale on the right represents displacement. Abscissa: Diameter of tube in meters. Ordinate: Length of tube in meters.

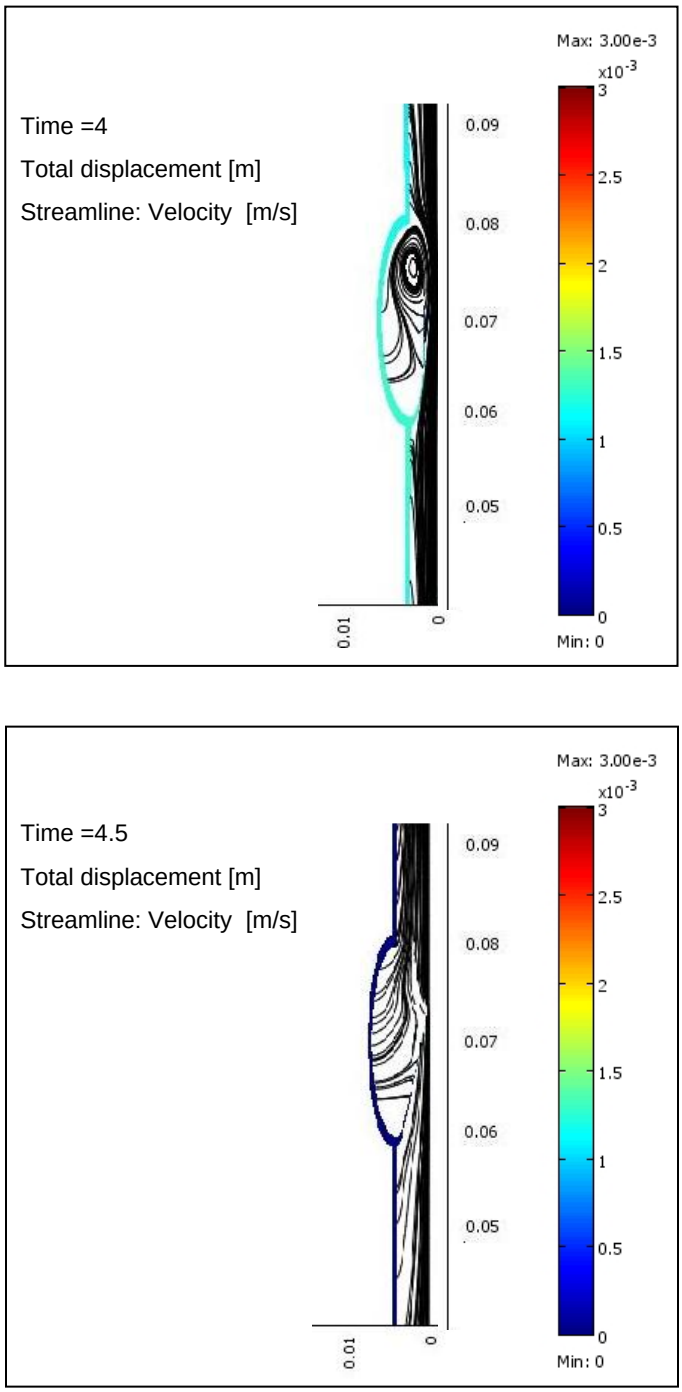


Figure 5.6. Fluid streamlines during the closing phase of the cycle. The scale on the right represents displacement. Abscissa: Diameter of tube in meters. Ordinate: Length of tube in meters.

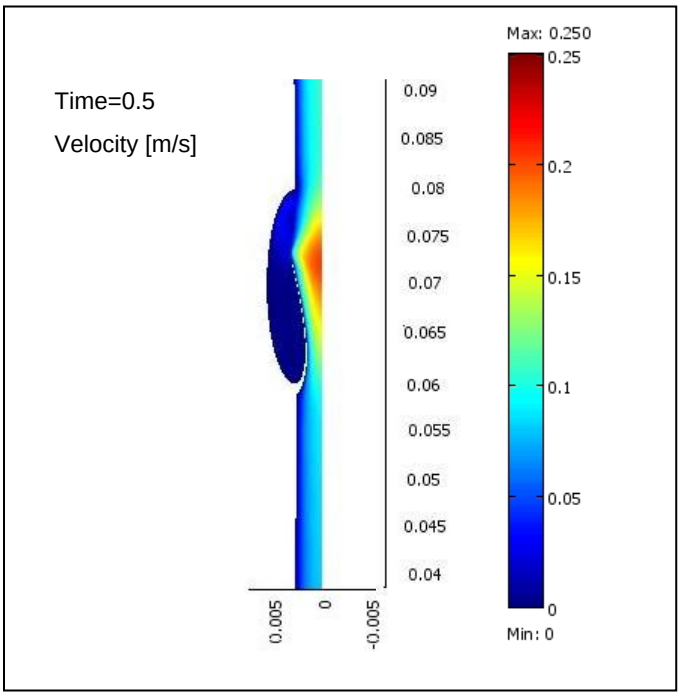


Figure 5.7. Axial fluid velocity at the open position. The scale on the right is the fluid velocity. Abscissa: Diameter of tube in meters. Ordinate: Length of tube in meters.

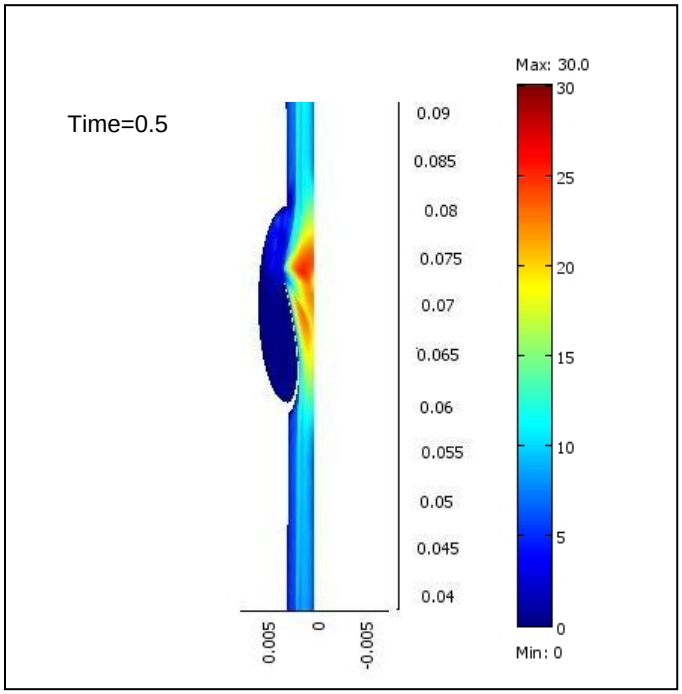


Figure 5.8. Reynolds number flow distribution. The scale on the right is the Reynolds number. Abscissa: Diameter of tube in meters. Ordinate: Length of tube in meters.

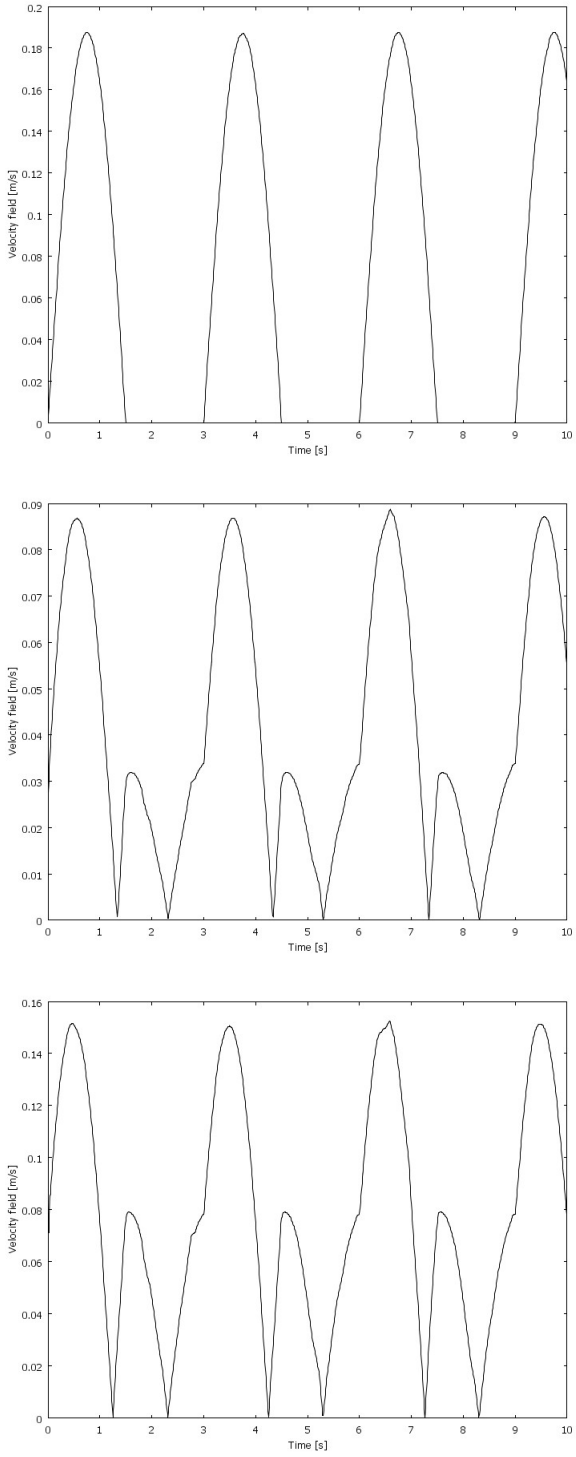


Figure 5.9. Centerline fluid velocity at different axial positions. Top: entrance (x=0 m, y=0 m). Middle: distal (x=0.05 m, y=0 m). Bottom: distal (x=0.065 m, y=0 m).

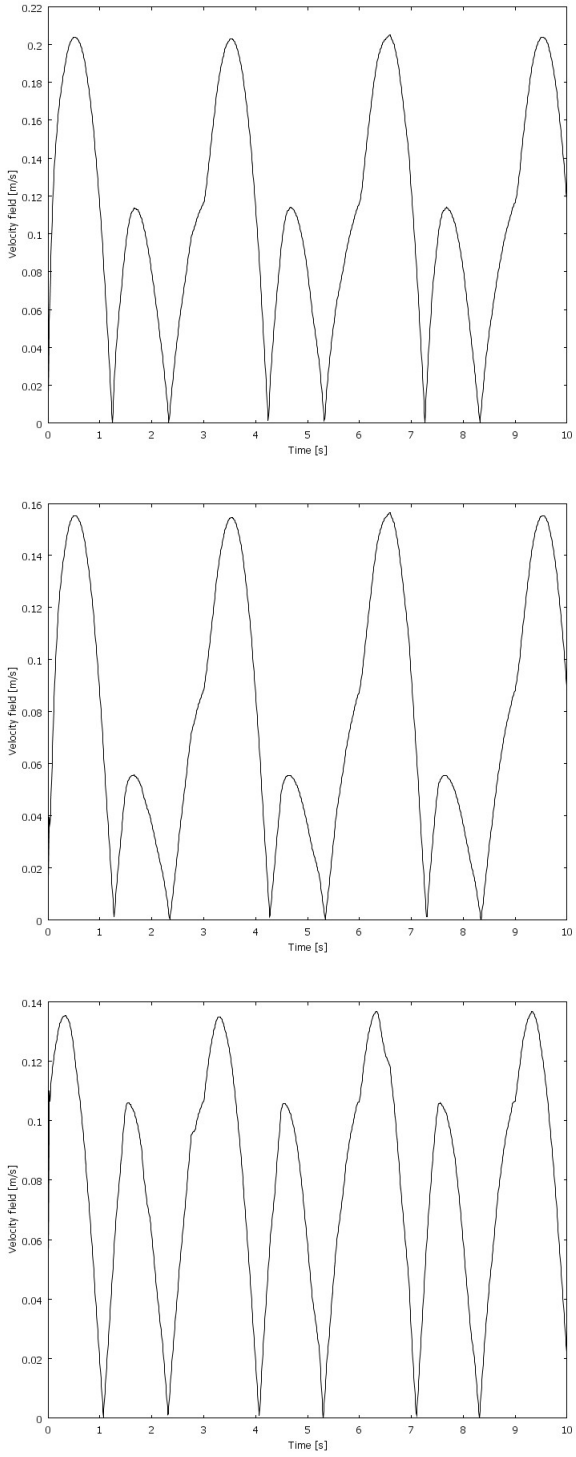


Figure 5.10. Centerline fluid velocity at different axial positions. Top: between the edge of the leaflet (x=0.073 m, y=0 m). Middle: proximal (x=0.077 m, y=0 m). Bottom: exit (x=0.18 m, y=0 m).

Table 5.4. Fluid velocity at different axial positions.

| Position | Range (cm/s) |
|---|---|
| Distal | 8 – 15 |
| In-between | 11 – 20 |
| Proximal | 13 – 15 |

flow directions.

5.3.1.2 *Motion of the leaflet free edge and vortex shedding at the leaflet free edge*

The motion of the leaflet occurs from 0 to 0.8 cm/s (see top panel of Figure 5.13). In the open phase, the free edge of the leaflet is about 0.35 cm from the centerline (see bottom panel of Figure 5.13). It has been observed that there is deformation in the tube during each cycle. However, this deformation is much less compared to the displacement of the leaflet, i.e the maximum tube wall displacement is about 25% of the maximum displacement of the leaflet edge (see Figures 5.3 to 5.6). Note that the scale of the figures prevents observing this deformation. The graphs in Figures (5.3 to 5.6) clearly show the formation of a vortex during the opening phase. During the equilibrium phase vortex shedding is observed, which can be attributed to the existence of self-excited oscillations.

The graphs in Figures 5.14 and 5.15 show the variation in the fluid shear rate at different positions of the leaflet. The highest variation of the fluid shear rate is observed at the medial side of the free edge of the leaflet (see bottom panel of Figure 5.15). This type of high variation in the fluid shear rate is expected at the medial side of the free edge of the leaflet due to vortex shedding. Referring to the motion of the leaflet's edge (the bottom panel of Figure of 5.13) it appears that the oscillations are low frequency oscillations. For the parameter values used, no high

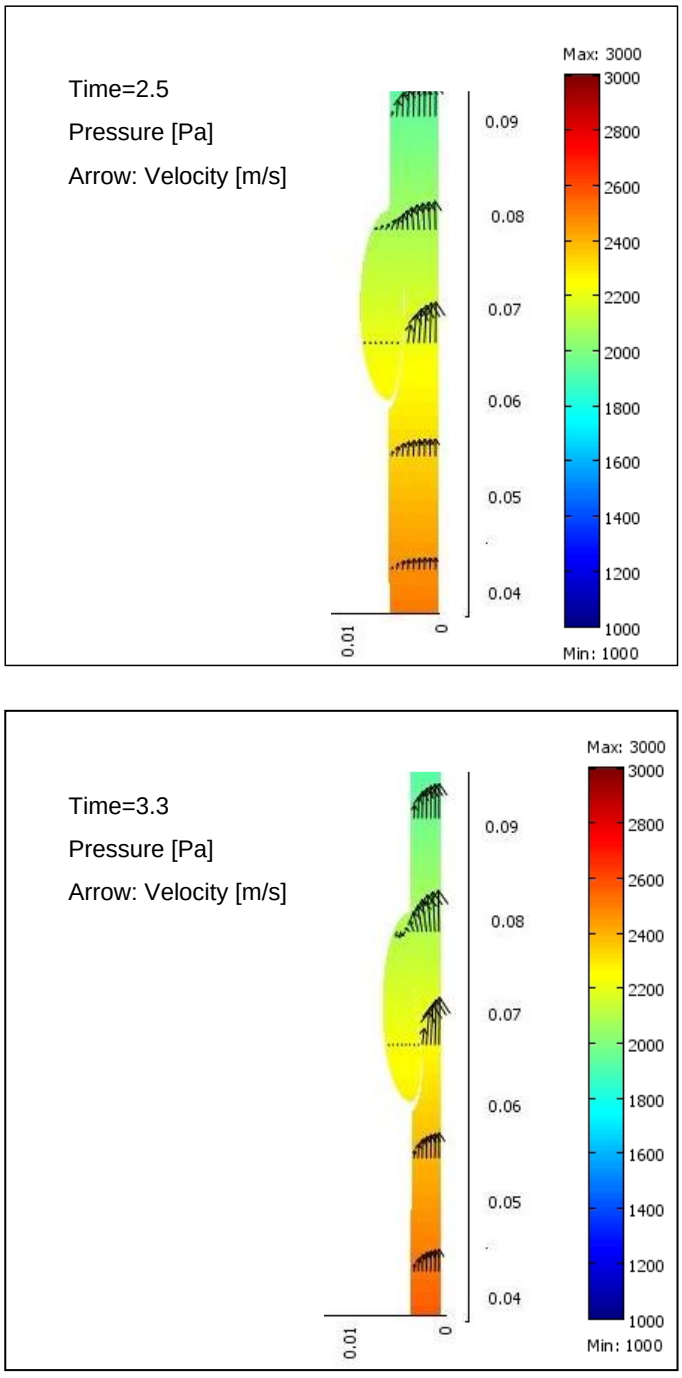


Figure 5.11. Pressure distribution. Top: opening phase. Bottom: open phase. Scale on the right represents pressure. Abscissa: Diameter of tube in meters. Ordinate: Length of tube in meters.

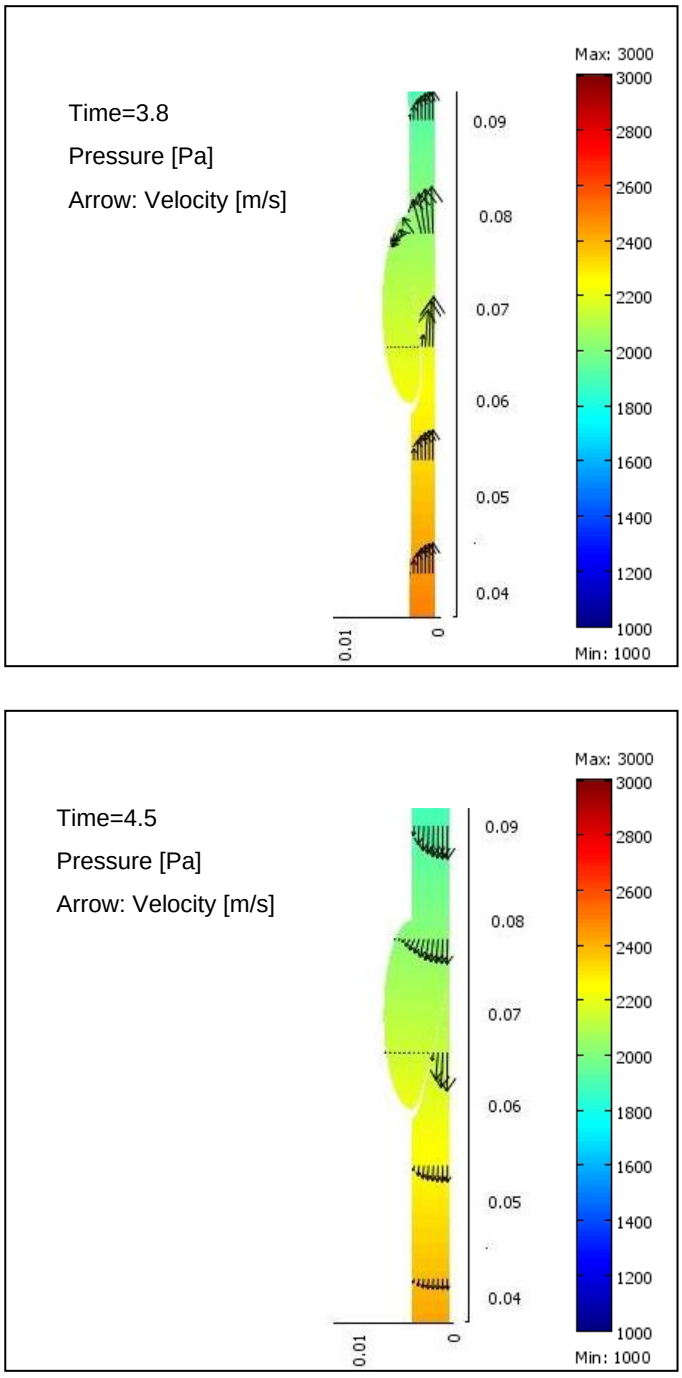


Figure 5.12. Pressure distribution. Top: closing phase. Bottom: closed phase. Scale on the right represents pressure. Abscissa: Diameter of tube in meters. Ordinate: Length of tube in meters.

frequency oscillations are observed. Furthermore, the magnitude of the shear rate variation at the inner points of the medial side of the leaflet (see bottom panel of Figure 5.14) is much less when compared to the corresponding point in the lateral side of the leaflet (see top panel of Figure5.14). Low fluid shear rate is indicative of the occurrence of small magnitude oscillations with less spatial variation and almost no vortex shedding.

#### 5.3.1.3 *Stress analysis on the leaflet free edge*

As the fluid flows from distal to proximal, the free edge of the leaflet move vertically up and down performing the valve opening and closure mechanisms. During the valve opening phase there are flow separation and vortex formation; and during the equilibrium phase, vortex shedding at the leaflet free edge. These events induce normal and shear stresses upon the free edge and ultimately cause motion of the leaflet's free edge (see bottom panel of Figure 5.13). The graphs in Figure 5.16 show the normal stresses acting in the radial and axial directions and surface shear stress acting on the free edge of the leaflet. All these stresses exhibit periodic behaviors. The normal stresses (see top panel of Figure 5.16) are synchronized together but, the shear stresses (see bottom panel of Figure 5.16) lag by about 1.5 seconds.

#### 5.3.1.4 *Normal and shear stress analysis on the leaflet and sinus wall*

Figures 5.17 and 5.18 show the total normal stress acting at the different positions of the leaflet on the medial and lateral sides of the leaflet, respectively. Both figures indicate that the highest stress occurs at the middle of the leaflet. Consider a time duration of 1.5 to 4.5 seconds. The time duration is equal to one full cycle.

Referring to Figures 5.17 and 5.18, it can be seen that as the valve starts opening, the total normal stress has accumulated at all positions of the valve during the opening phase (until about 1.8 s). Also during the next 1.5 s it can be seen that there is an

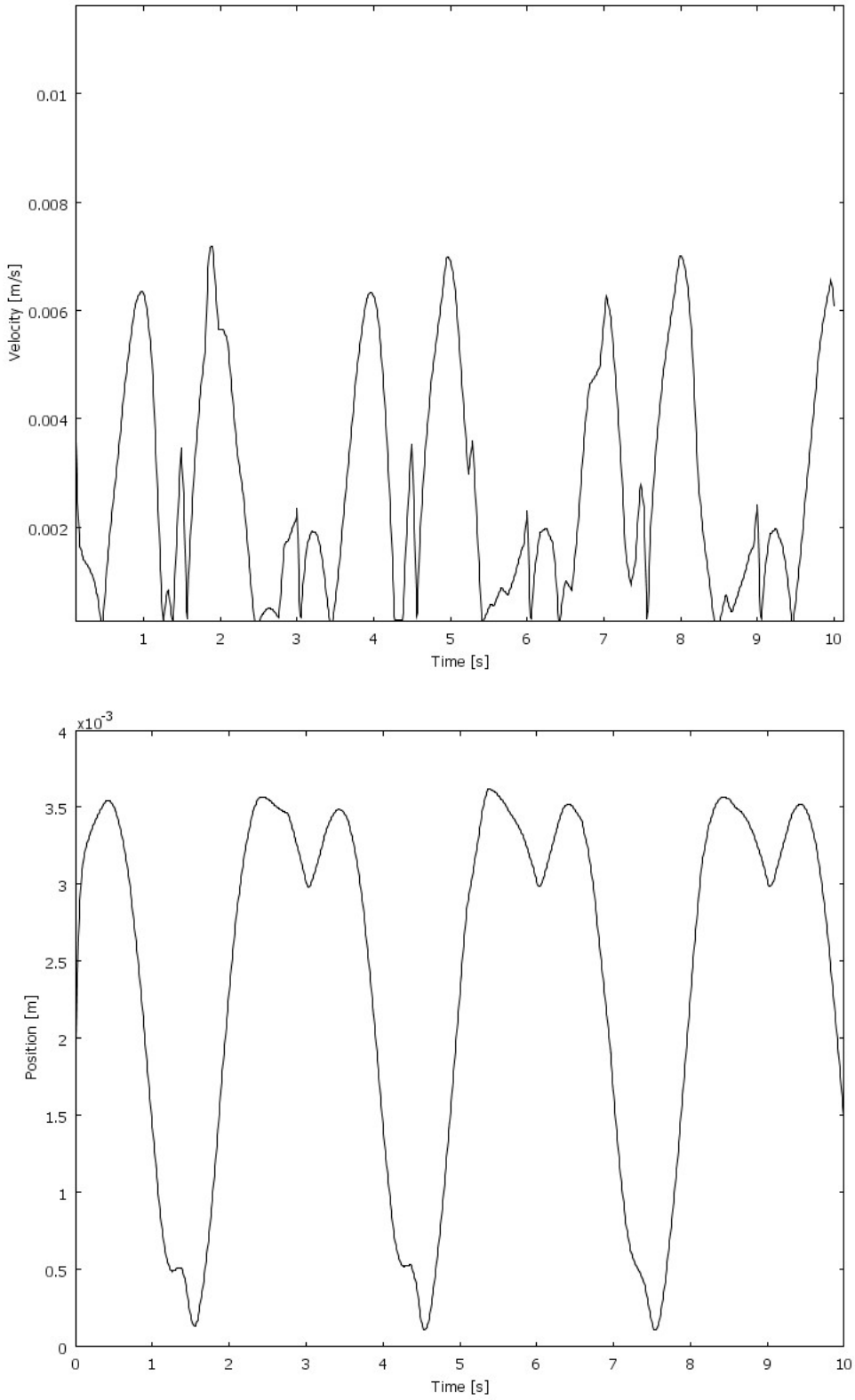


Figure 5.13. Top: motion of the leaflet's free edge. Bottom: position of the leaflet's free edge.

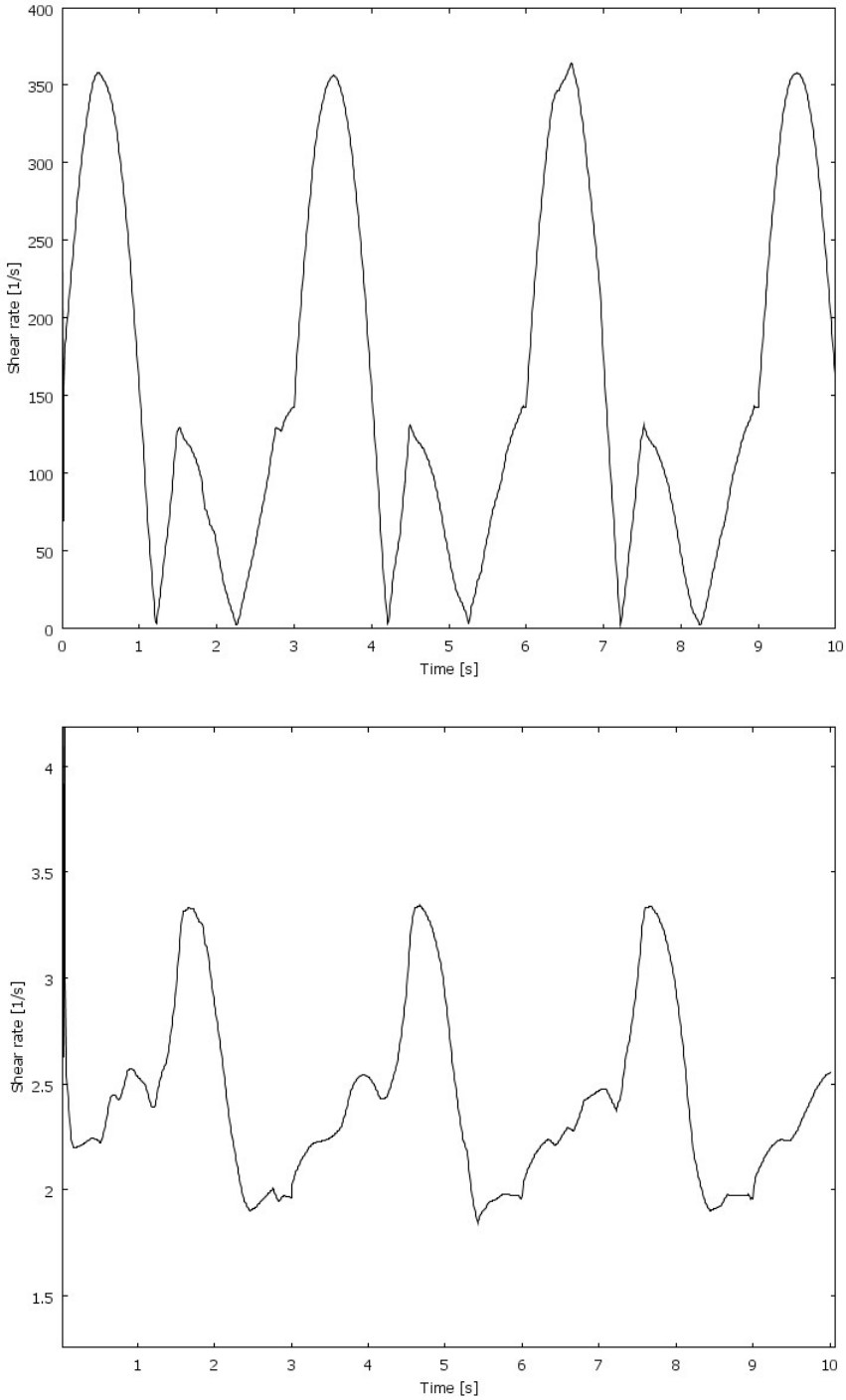


Figure 5.14. Fluid shear rate at lateral and medial sides at the middle point of the leaflet. Top: lateral side. Bottom: medial side.

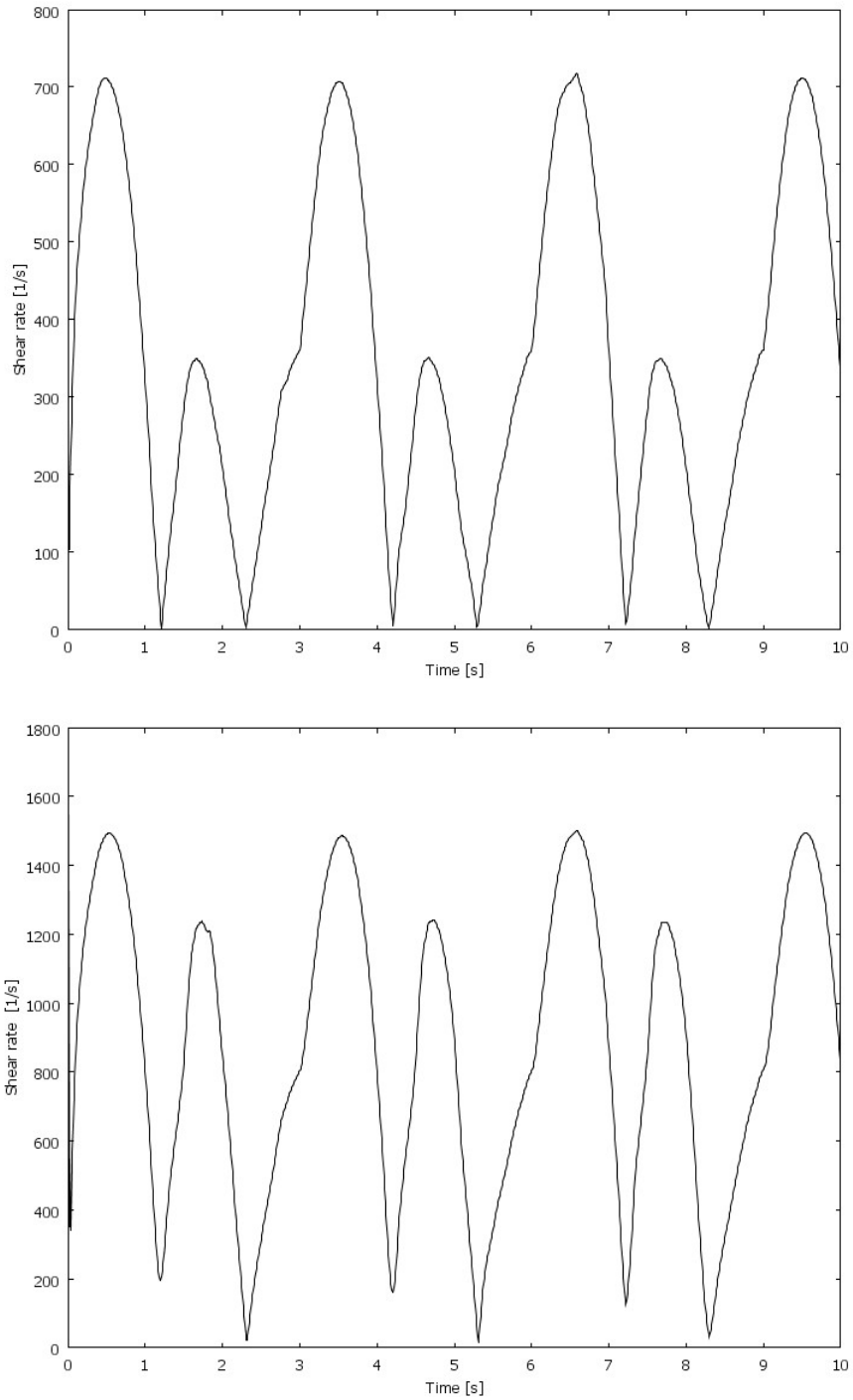


Figure 5.15. Fluid shear rate at lateral and medial sides of the free edge of the leaflet. Top: lateral side. Bottom: medial side.

overall increase in the normal stress at all points on the leaflet, which coincides with the duration of the equilibrium phase. A decrease in the induced stress in the leaflet is observed during the closing phase (i.e about 4.2 s of the cycle time). Then during the closed phase, stress starts to increase once again. Stresses at middle of the leaflet and at the free edge exhibit synchronized induced total stress profiles. These types of profiles for stress variation on the leaflet can be expected due to the two-dimensional model of the system. The absence of circumferential tension in the 2D model (which is present in the 3D model) may affect the total stress pattern at each point in the leaflet. Figure 5.19 shows the total normal stress variation acting on the edges and also at the middle of the sinus wall. It can be observed that the largest stresses (magnitude) occur at the middle of the sinus wall. However, these values are much less in magnitude when compared to the normal stress values induced in the leaflet.

### 5.3.2 Results:Impact of fluid viscosity

#### 5.3.2.1 *Comparison of the viscosity models*

Figures 5.20 and 5.21 compare the effect of different viscosity models on the closing and opening of the leaflet. The left panel shows the leaflet closing and opening based on viscosity model 1 in contrast to the right panel whose results are based on viscosity model 2. In both cases, it can be seen that inside the leaflet sinus the fluid viscosity is the highest. With the second viscosity model, a wider viscosity range is found inside the sinus cusps. Outside the sinus the viscosity distribution is similar in both cases. This effect can be attributed to fluid pooling inside the cusps due to reduced fluid velocities and also due to the formation of vortices. As a result the displacement of the leaflet estimated by the first viscosity model is about 0.38 cm from the centerline as compared to a displacement of 0.35 cm estimated by the second viscosity model.

Both models exhibit similar viscosity distributions at the medial side of the leaflet.

It is reasonable to conclude that the magnitude of the viscous forces acting on the medial side of the leaflet is similar in both cases. However, the lateral side of the leaflet experiences different size viscous force in each case. A higher viscous force is estimated by the second viscosity model thereby creating a greater resistance to the leaflet displacement on the lateral side.

#### 5.3.2.2 *Effect of solids on the fluid dynamics*

Figure 5.22 shows the effect of changes in the solid content of the fluid. In the case of blood, this change represents a change in the hematocrit value. The model results presented so far assumes 30% solids. The leaflet displacement (open position) is estimated at about 0.35 cm from the centerline. However, with an increase from 30% to 50%, the displacement from the centerline is 0.3 cm or a 14% reduction. As expected an increase in the solids content increases the viscosity of the fluid creating higher viscous forces inside the sinus which in turn restricts the motion of the leaflet.

### 5.3.3 Result: Sensitivity analysis of the system's elasticity

The elasticity of the leaflet and the tube wall play a major role in the geometric configuration of the entire system at any given time. The magnitude of the Young's moduli of the system is an indication of the system's ability to extend or collapse under the imposed fluid and external forces. The Young's moduli of the leaflet and tube wall are very different (different order of magnitude). According to in vivo measurements of Ackroyd et al. [70] the leaflet material exhibits higher elasticity modulus as compared to that of the tube wall material. In general, these elasticities exhibit anisotropic properties. For the present computational purpose, isotropic properties are assumed for both leaflet and the tube wall.

In order to estimate the impact of the flexibility of the leaflet and the tube wall on the overall dynamics of the system, the following procedure is adopted.

5.3.3.1 *Design of experiment procedure*

The methodology for the selection of the parameter values for the elastic modulus is adopted from the procedure suggested by Cho et al. [71]. This procedure uses a Monte Carlo method to select the parameter values that ensure feasible results.

**1.** Young's moduli for both leaflet and the tube wall are assumed to have a normal distribution. The mean and the standard deviation for each material is given in Table 5.5.

Table 5.5. Statistics of the leaflet and tube wall elastic moduli.

| Component | Mean (Pa) | Standard Deviation (Pa) |
|---|---|---|
| Leaflet | $15\times10^6$ | $10\times10^6$ |
| Tube wall | $3.3\times10^6$ | $2.5\times10^6$ |

**2.** It is necessary to determine for any selected combination of elastic moduli, whether it possible to obtain an accurate, convergent solution. Therefore the selection of the combination of the elastic moduli are forced to be in feasible regions within each distribution that ensure convergent and accurate results. Thus, an objective function is defined based on the output variable of the dynamic model. Here, the vertical displacement of the leaflet free edge is selected as the output variable to be used in the objective function. The objective function is given by,

$$F_{obj} = \sum_{i=1}^{T_{span}} \left(v_{2_{baseline}}(i) - v_{2_{current}}(i)\right)^2 . \tag{5.1}$$

where $F_{obj}$ is constrained by a pre-determined threshold value given for the system. The variables, $v_{2_{baseline}}(i)$, and $v_{2_{current}}(i)$, define the displacements of the leaflet's free edge at time $i$ for the baseline case and the current case, respectively.

**3.** The constraint (i.e. threshold value) for the objective function is determined using the information obtained from test data. The procedure to determine the threshold value is as follows. With a set of initial test data (i.e. combination of randomly selected elastic moduli from each distribution) the system of governing equations for the leaflet and the tube is solved and the leaflet's free edge motion is observed. These data together with the baseline data are used to estimate the objective function for each case. These data are used to establish a relationship between the two elastic moduli and the objective function value. By analyzing the objective function value and the corresponding leaflet free edge displacement for each case, the threshold value is set at $10^{-4}m^2$. Thus, any combination of the elastic moduli that produce an objective function value less than or equal to the threshold value is used in the sensitivity analysis.

Once the combination of elasticity moduli that satisfy the constraint value of the objective function 5.1 is selected, these parameter values are used in the sensitivity analysis. The elastic moduli used in the sensitivity analysis and their percentage change from the respective nominal values are listed in Table 5.6. A negative value indicates a decrease in the current value relative to the baseline value.

Figures 5.23 to 5.26 show the leaflet free edge displacement against the baseline for each case. It is observed that these changes affect the leaflet closure. Cases 2, 3, 6, and 7 are when both elastic moduli increase in magnitude. It can be seen from these figures, that the leaflet may not close properly leading to undesired retrograde flow. Referring to the corresponding percentage increase in the elastic moduli, it can be deduced that the impact on the overall displacement of the leaflet's free edge due to an increase in the leaflet elasticity is more significant than changes in the tube material elasticity.

Case 8 considers the impact on the displacement of the leaflet's free edge due to decreases in both elastic moduli. The results show that the leaflets close properly and also that the maximum opening of the leaflet increases relative to the base case. Table 5.7 lists the percent change (relative to the base case) in the maximum and minimum values that the leaflet's free edge experiences during the closing phase. This analysis confirms that a decrease in the flexibility of the leaflet and the tube material affects closing of the leaflet.

Table 5.6. Leaflet and tube wall elastic moduli.

| | Elastic moduli ($\times 10^7$Pa) | | Percent change (%) | |
|---|---|---|---|---|
| Case | Tube wall | Leaflet | Tube wall | Leaflet |
| 1 | 0.1146 | 1.7467 | -65.2727 | 16.4467 |
| 2 | 0.3480 | 3.2327 | 5.4545 | 115.5133 |
| 3 | 0.8073 | 1.9945 | 144.6364 | 32.9667 |
| 4 | 0.1734 | 1.7279 | -47.4545 | 15.1933 |
| 5 | 0.2742 | 3.3027 | -16.9091 | 120.1800 |
| 6 | 0.3909 | 1.7041 | 18.4545 | 13.6067 |
| 7 | 0.5118 | 2.0924 | 55.0909 | 39.4933 |
| 8 | 0.2128 | 1 .342 | -35.5152 | -10.5333 |

Table 5.7. Maximum and minimum displacement from the base case.

| Case | Max (%) | Min (%) |
|---|---|---|
| 1 | - 1.7511 | -209.0136 |
| 2 | - 6.4670 | - 538.2478 |
| 3 | - 2.2241 | - 296.0078 |
| 4 | - 2.5312 | - 166.7838 |
| 5 | - 3.4855 | - 543.6144 |
| 6 | - 2.3131 | - 148.4222 |
| 7 | - 4.6379 | -393.2503 |
| 8 | 7.0549 | 180.5705 |

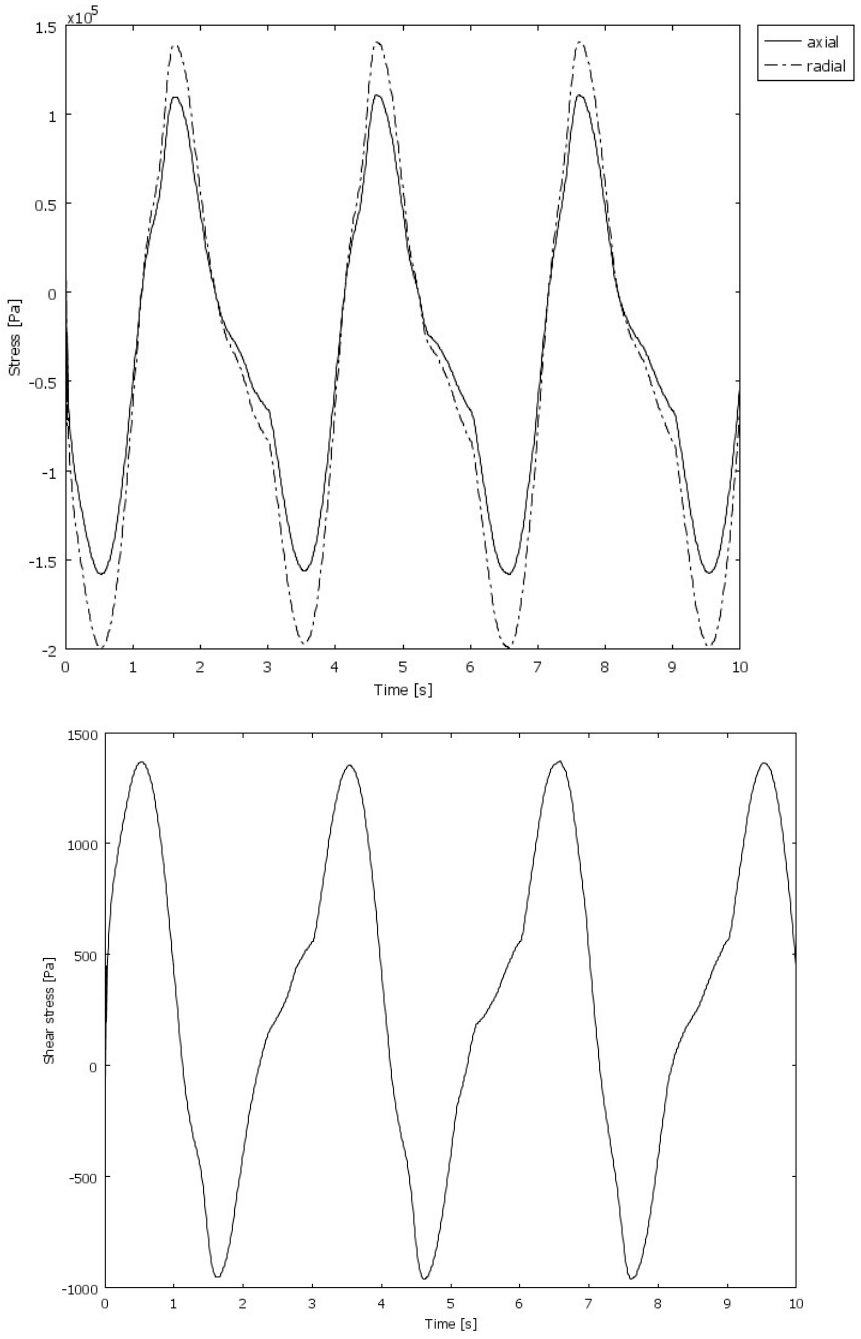


Figure 5.16. Normal and shear stresses at the free edge of the medial side of the leaflet. Top: normal stress in radial (dash-dot) and axial (solid) directions. Bottom: shear stress.

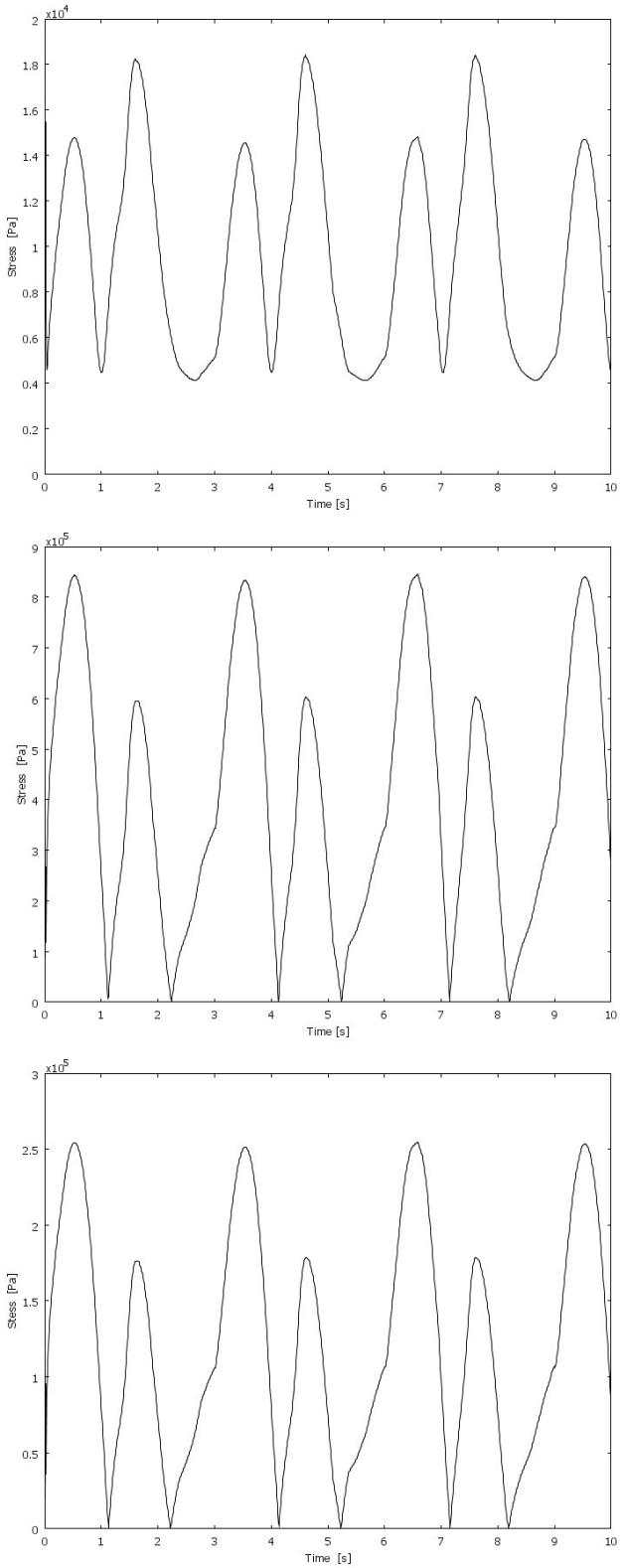


Figure 5.17. Total normal stress at different positions on the medial side of the leaflet. Top: at the vessel wall. Middle: middle of the leaflet. Bottom: free edge of the leaflet.

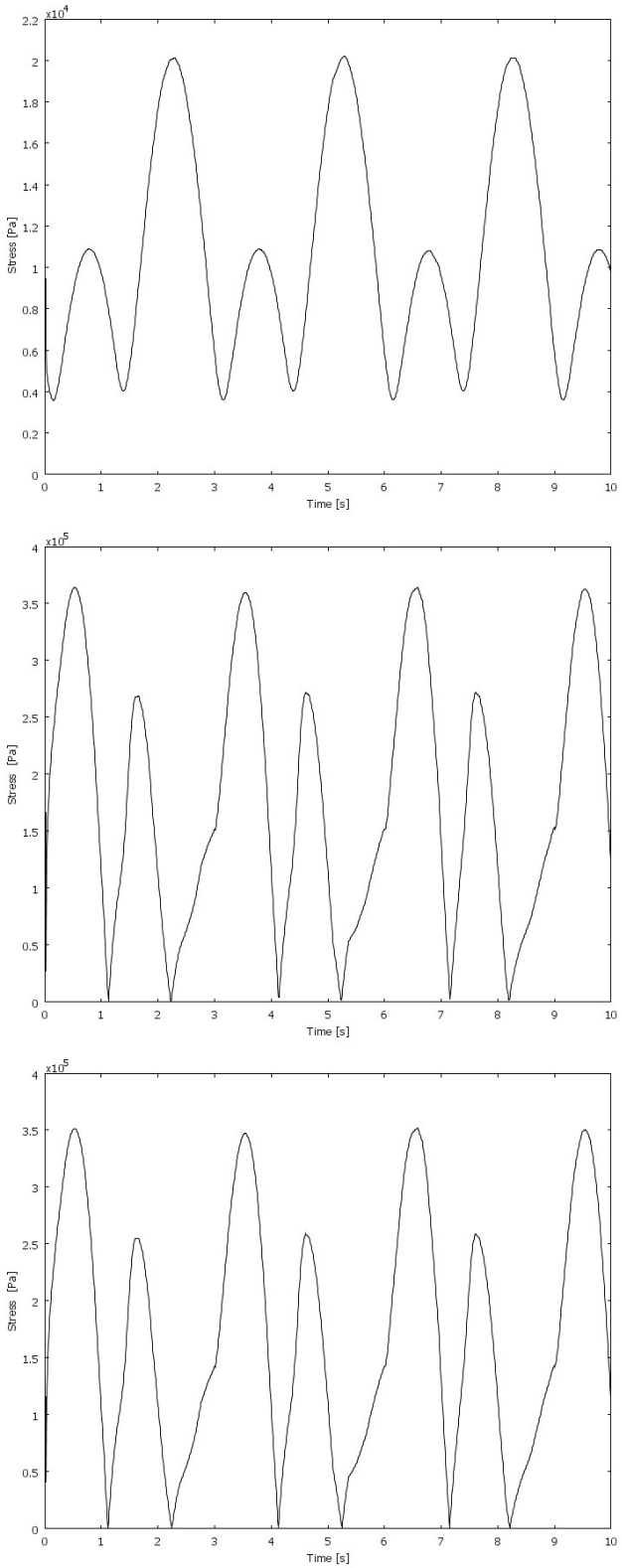


Figure 5.18. Total normal stress at different positions at the lateral side of the leaflet. Top: at the vessel wall. Middle: middle of the leaflet. Bottom: free edge of the leaflet.

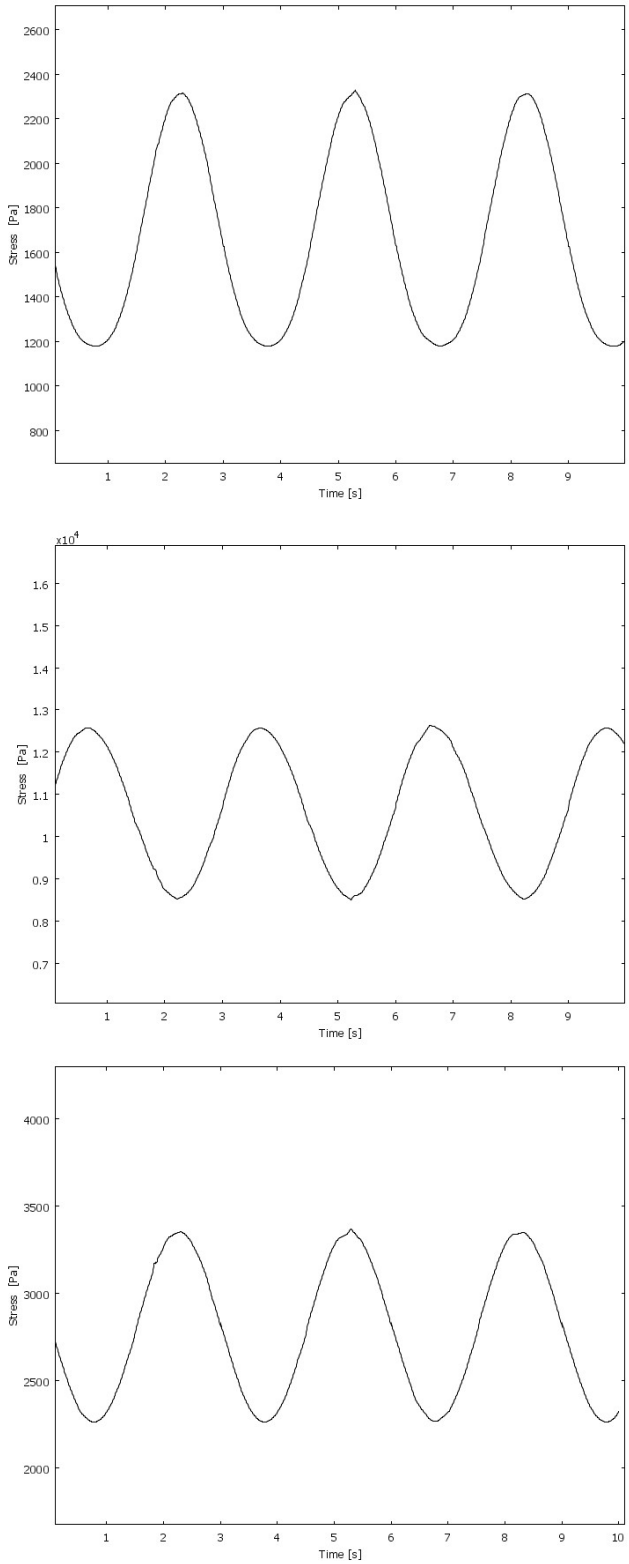


Figure 5.19. Total normal stress at different positions at the sinus wall. Top: edge nearest to the distal side. Middle: middle of the sinus wall. Bottom: edge nearest to the proximal side.

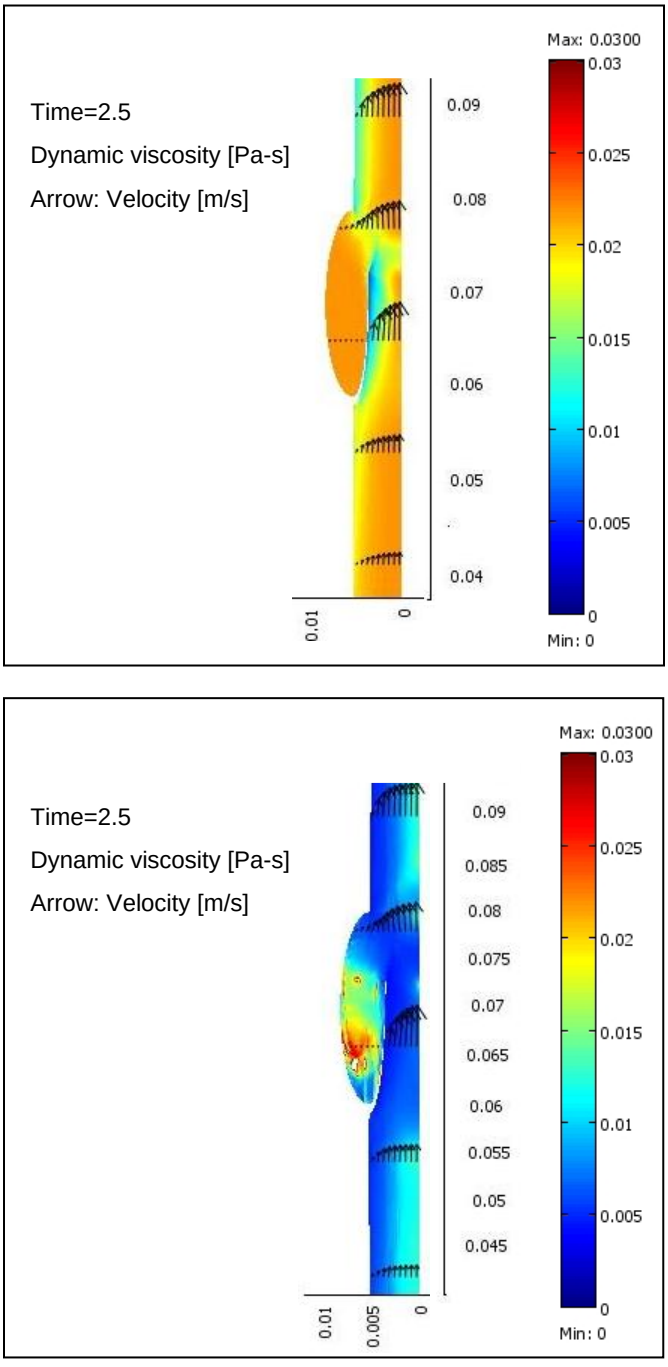


Figure 5.20. Viscosity distribution during the opening phase. Top: viscosity model 1. Bottom: viscosity model 2. Abscissa: Diameter of tube in meters. Ordinate: Length of tube in meters.

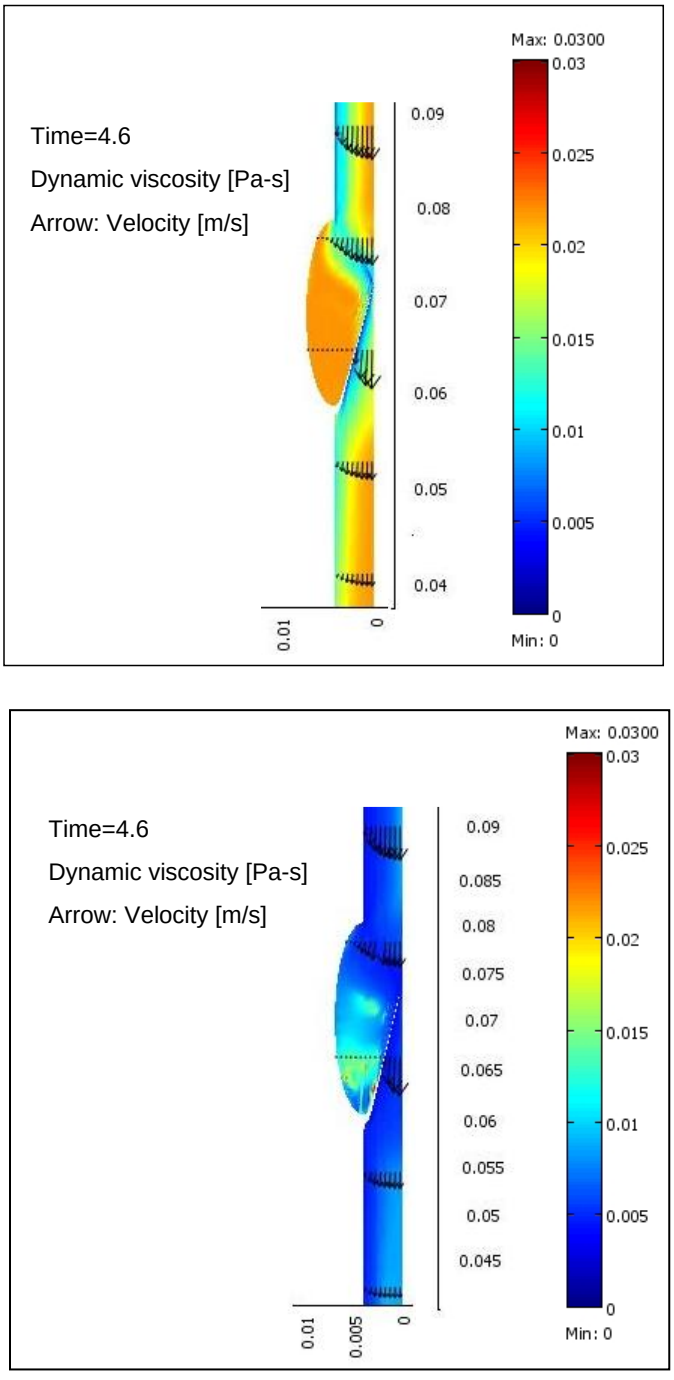


Figure 5.21. Viscosity distribution during the closed phase. Top: viscosity model 1. Bottom: viscosity model 2. Abscissa: Diameter of tube in meters. Ordinate: Length of tube in meters.

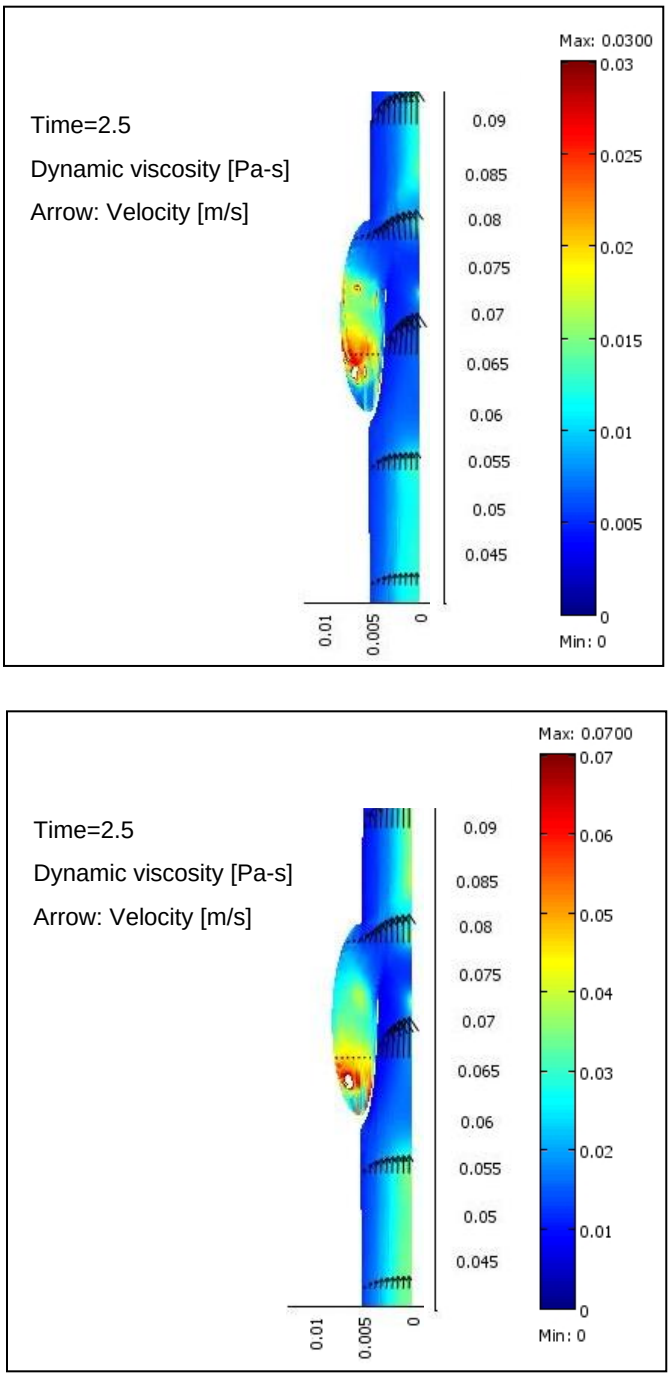


Figure 5.22. Effect due to different percent solids. Top: 30%. Bottom: 50%. Abscissa: Diameter of tube in meters. Ordinate: Length of tube in meters.

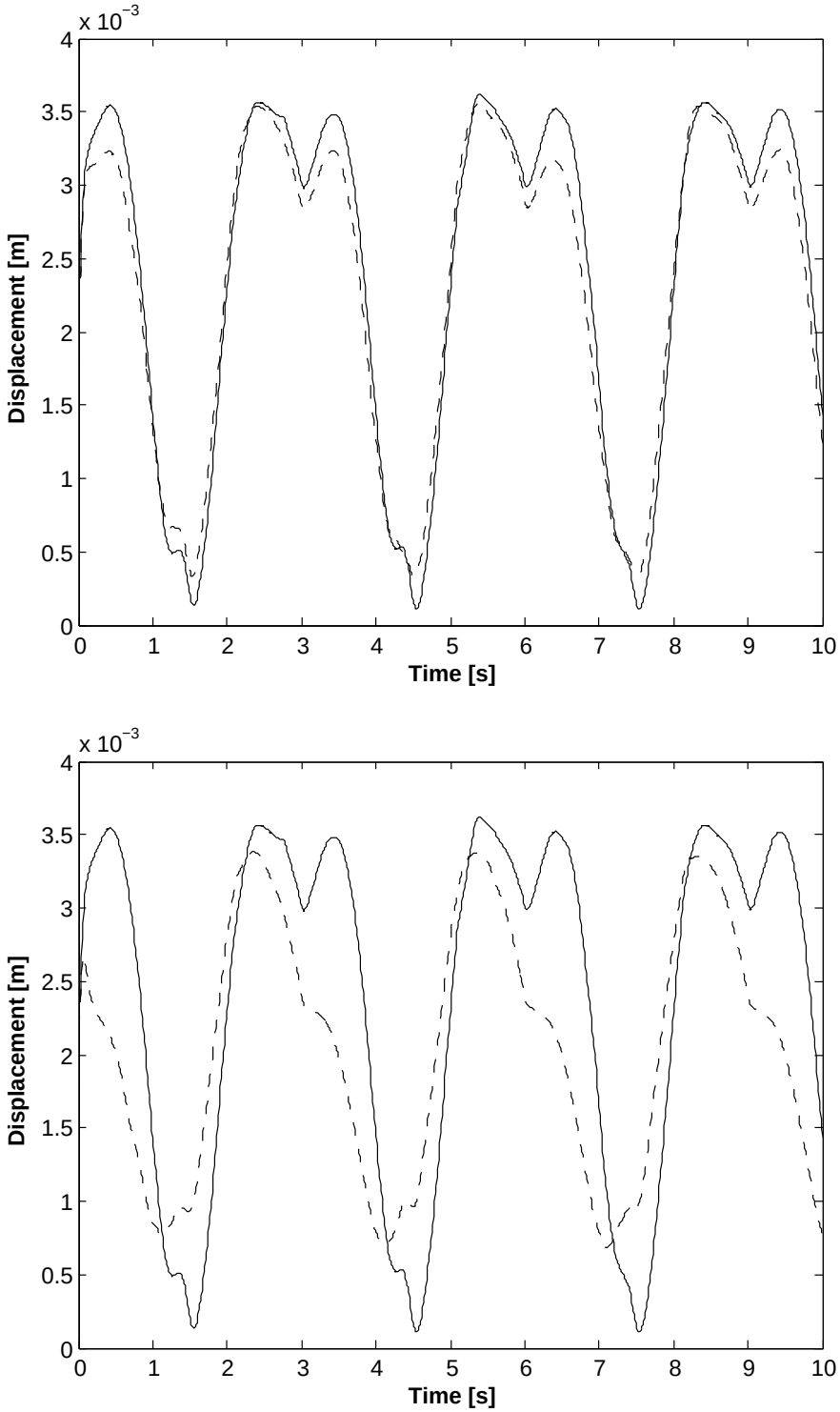


Figure 5.23. Sensitivity of the elasticities of the tube and leaflet. (Solid line: Base case. Dash line: Trial case.) Top: case 1. Bottom: case 2.

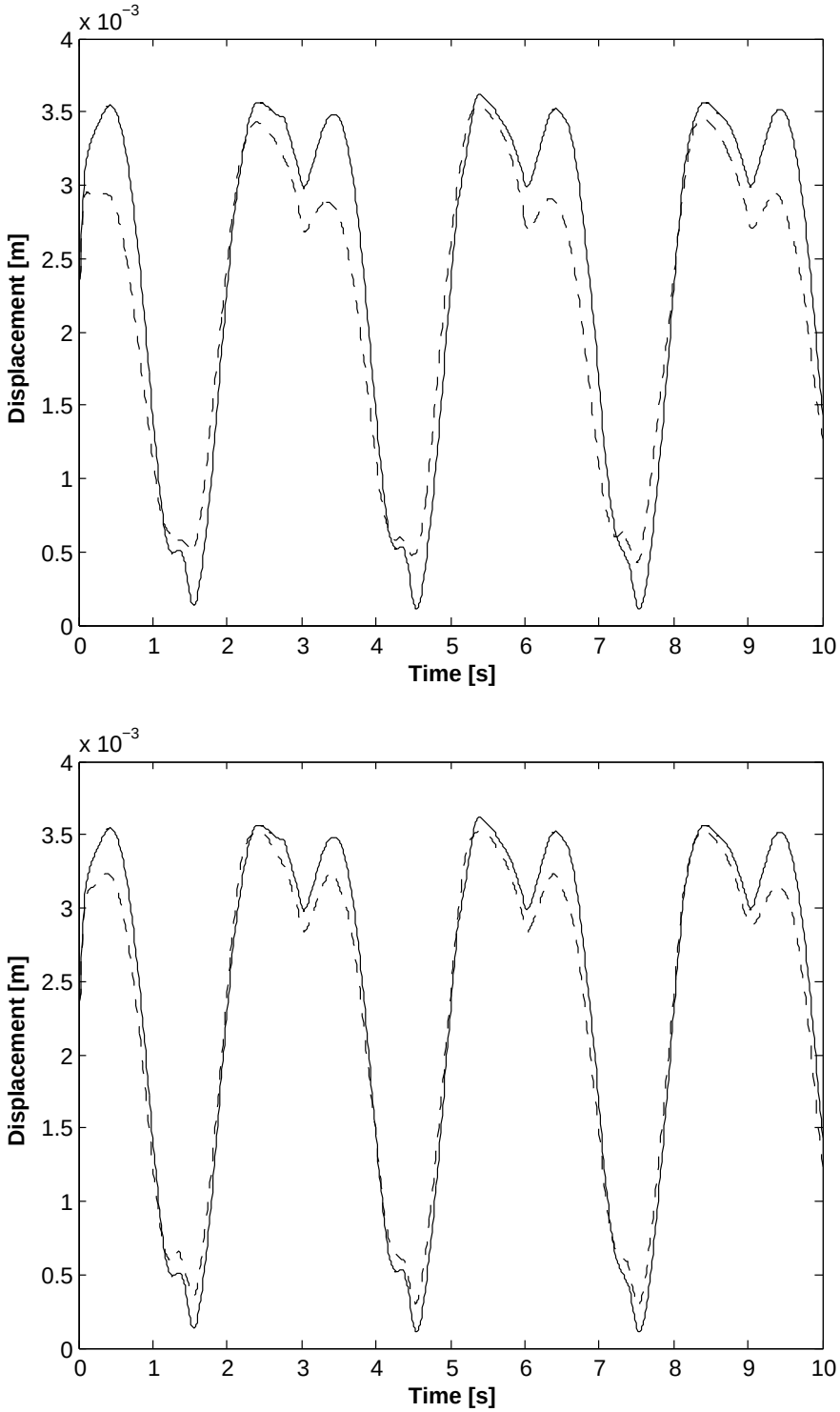


Figure 5.24. Sensitivity of the elasticities of the tube and leaflet. (Solid line: Base case. Dash line: Trial case.) Top: case 3. Bottom: case 4.

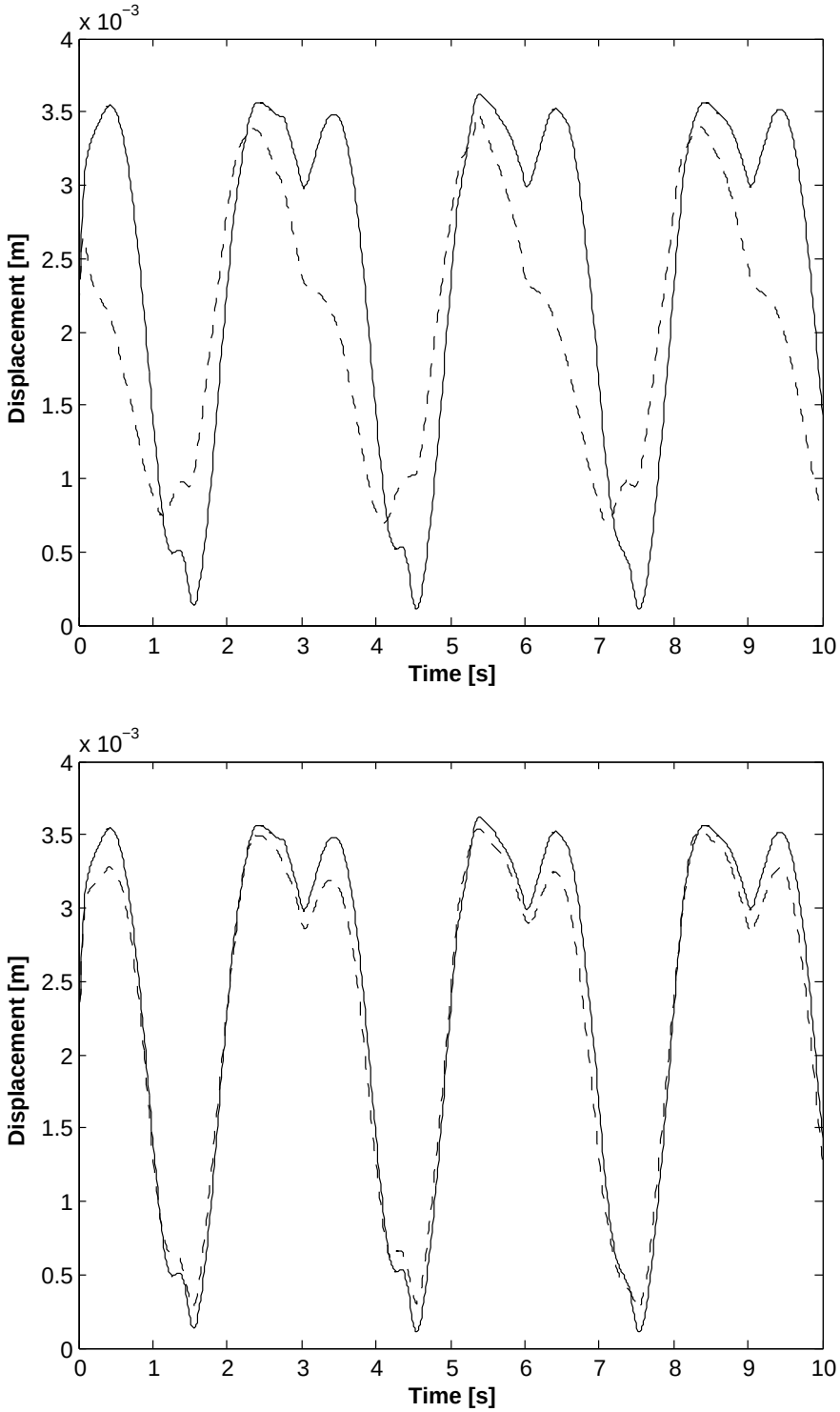


Figure 5.25. Sensitivity of the elasticities of the tube and leaflet. (Solid line: Base case. Dash line: Trial case.) Top: case 5. Bottom: case 6.

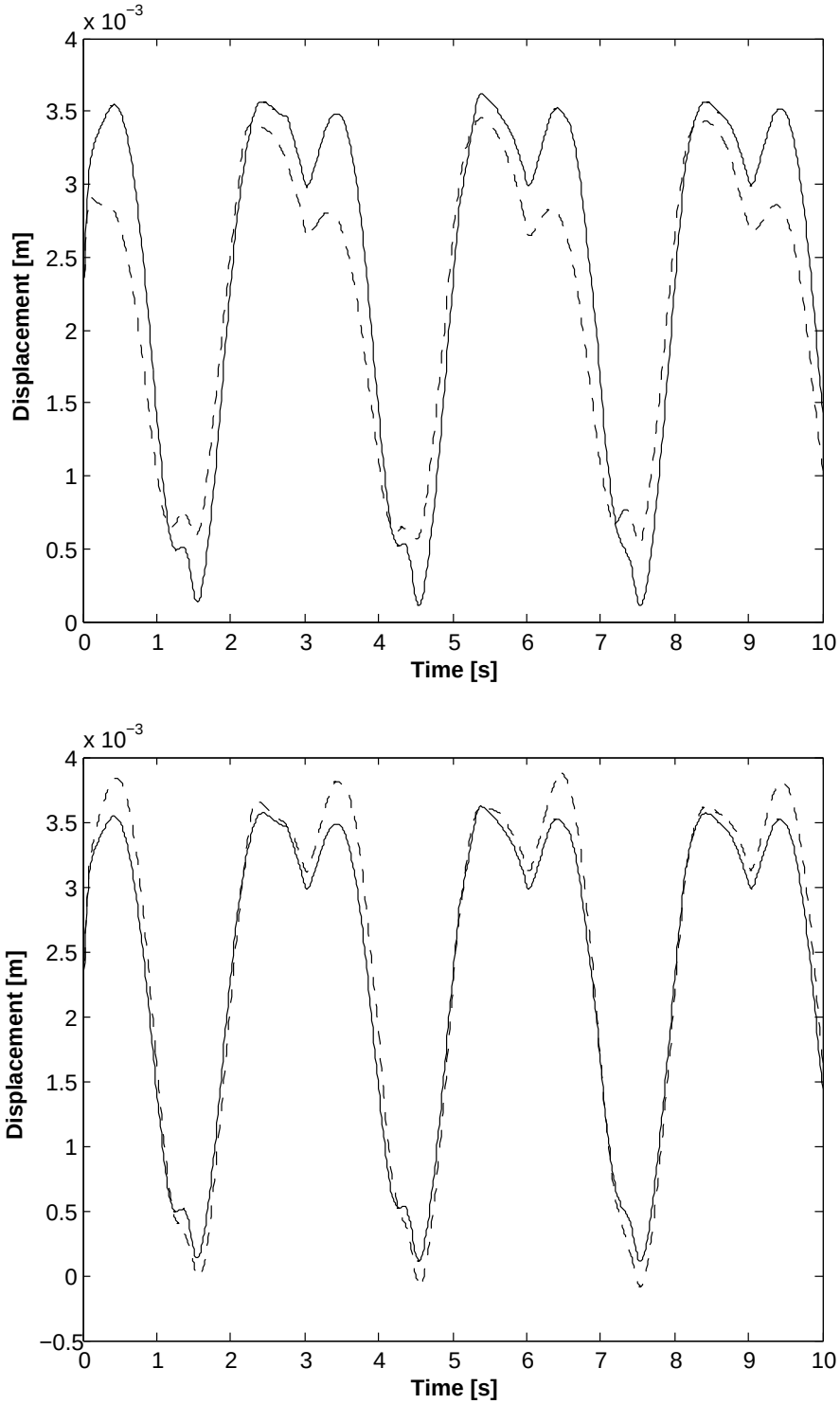


Figure 5.26. Sensitivity of the elasticities of the tube and leaflet.(Solid line: Base case. Dash line: Trial case.) Top: case 7. Bottom: case 8.

### 5.3.4 Result: Boundary conditions impact analysis

It has been observed that certain frequencies of the entering fluid velocity and the external compression applied to the tube wall influence the dynamics of the fluid within the tube and hence the leaflet motion. Panels in Figure 5.27 show the motion of the leaflet free edge at different combinations of boundary conditions for the entering fluid velocity and the external tube wall compression against that of the base case. Table 5.8 lists the boundary conditions used in each case. The periodic functions that are used to represent the boundary conditions and the compression function are given by,

$$F_1 = \begin{cases} \sin\left(\dfrac{2\pi t}{T_c}\right) & (n-1)T_c \le t \le 0.5(2n-1)T_c \quad n = 1, 2, \ldots \\ 0 & 0.5(2n-1)T_c \le t \le nT_c \end{cases}$$

$$F_2 = \begin{cases} \sin\left(\dfrac{2\pi t}{T_c}\right) & (n-1)T_c \le t \le 0.33(2n-1)T_c \quad n = 1, 2, \ldots \\ 0 & 0..33(2n-1)T_c \le t \le nT_c \end{cases}$$

$$F_3 = \left[x_1(x_1 - L)(x_1 - L - 0.09)(x_1 - L - 0.135)\right] / [L^4]$$

where $T_c$ represents the time to complete one leaflet cycle (i.e. the duration to open and close the leaflet.).

Table 5.8. System conditions.

| Case | Inlet fluid velocity | Tube wall compression |
|---|---|---|
| 1 | $U_{max}F_1$ | $\delta_{max}(-F_2)F_3$ |
| 2 | $U_{max}F_2$ | $\delta_{max}(-F_1)F_3$ |
| 3 | $U_{max}F_2$ | $\delta_{max}(-F_2)F_3$ |

where $U_{max}$ is the maximum centerline entrance velocity of the fluid, and $\delta_{max}$ is the

maximum displacement imposed on the tube wall due to external compression. All simulations are carried out with $\delta_{max}$ equal to 0.002 m.

Referring to top panel in Figure 5.27, it can be deduced that a decrease in the duration of the tube wall compression increases the oscillatory motion of the leaflet. Additionally, the maximum opening (length) of the leaflet increases by 20% and the closing (length) of the leaflet decreases by 150% relative to the base case.

The middle panel of Figure 5.27 shows the leaflet's free edge motion against that of the base case due to a decrease in the frequency of the entering fluid flow velocity. An increase in the oscillatory motion of the leaflet free edge can been observed. However, the maximum displacement of the leaflet's free edge has increased significantly (about 94%) compared to the base case. The closure of the leaflet is not affected.

A decrease in the frequency of the entering fluid velocity and the tube compression increases the leaflet opening and the oscillatory motion of the leaflet (see bottom panel of Figure 5.27). In this case, the maximum opening distance of the leaflet is increased by 81% and complete closure of the leaflet can be observed.

This sensitivity analysis reveals that the influence of variations in the fluid velocity frequency has a greater impact on the leaflet motion than variations in the frequency of the external compression of the tube wall.

## 5.4 Double Valve and Vein System

In general, veins in the lower extremities of the human body contain multiple valves arranged in a sequential manner [1]. In this section, the dynamics of the fluid flow in a double valve and tube system is investigated. The mathematical formulation of the fluid and solid domain are the same as in the case of a single leaflet and tube system described in chapter 4. Additionally the model parameter values remain the same. The dimensions of this model are listed in Table 5.9.

Table 5.9. Dimensions of the double leaflet and tube system

| Parameter | Value(cm) |
|---|---|
| Tube diameter | 0.4 |
| Tube thickness | 0.05 |
| Tube length | 25 |
| Valve depth | 0.9 |
| Sinus height | 0.22 |

To introduce a non-uniformity in the tube wall compression, segments of the tube wall that contain a leaflet are subjected to different compression frequency. The external tube wall boundary conditions are given by,

$$\begin{aligned} &\delta_{max} D_1 D_3 \qquad 0 \le x_1 \le L_{v_1} \\ &\delta_{max} D_2 D_3 \qquad L_{v_1} < x_1 \le L_d \end{aligned} \tag{5.2}$$

where $L_{v_1}$ is the length of the tube up to the end of sinus wall (i.e. $0 < L_{v1} = 0.0825m < L_d = 0.25m$) of the first valve and and $L_d$ is the length of the tube.

$$D_1 = \begin{cases} \sin\left(\dfrac{2\pi t}{T_c}\right) & (n-1)T_c \le t \le 0.5(2n-1)T_c \qquad n = 1, 2, \ldots \\ 0 & 0.5(2n-1)T_c \le t \le nT_c \end{cases}$$

$$D_2 = \begin{cases} \sin\left(\dfrac{2\pi t}{T_c} + \dfrac{\pi}{2}\right) & (n-1)T_c \le t \le 0.33(2n-1)T_c \qquad n = 1, 2, \ldots \\ 0 & 0.33(2n-1)T_c \le t \le nT_c \end{cases}$$

$$D_3 = \left[x_1(x_1 - L_d)(x_1 - L_d - 0.0635)(x_1 - L_d - 0.125)(x_1 - L_d - 0.1875)\right] / [L_d^5] \tag{5.3}$$

This analysis is carried out using the second viscosity model and a 30% solid percent. Figures 5.28 to 5.29 show the fluid flow velocity and streamline pattern in

the double leaflet system during the opening and closing phases of each valve. The formation of vortices in the leaflet sinus during the opening phase in both leaflets can be observed. The leaflet cycle (i.e. duration from opening to closed position) for both leaflets is 3 seconds.

Figure 5.30 shows the displacement of the each leaflet's free edge. It has been observed that the displacement of the second leaflet lags behind that of the first. The maximum displacement of the free edge of the second leaflet is about 17% less than that of the first leaflet. This type of displacement is attributed to the varying compression frequencies exerted on different segments of the tube's external wall and also to the influence of preceding leaflet.

## 5.5 Summary

This study presented the simulation results of a two-dimensional first-principles model that describe the fluid dynamics of a non-Newtonian fluid within a flexible tube that contained a flexible pair of symmetrical leaflets. The tube and leaflets are surrogates for the human vein and venous bicuspid valve found in the lower legs. The general model was presented in chapter 4.

The model enabled an estimation of the extent of valve opening and closing as a function of fluid dynamics and fluid-structure interactions. The Femlab® environment was used to solve the model and its capabilities permitted visualization of the formation of vortices and their role in flow regulation and leaflet motion. Stress analysis on the leaflet enabled the identification of those locations that were under higher stresses. A sensitivity analysis using different hematocrit (% solids) values showed the impact of blood thinning or thickening (viscosity) on the motion of the leaflet.

A parameter sensitivity analysis on the elasticity of the system confirms that an increase in the elastic modulus of the leaflet affect the closing of the leaflet. A

sensitivity analysis on the boundary conditions involving entering fluid velocity and external compression of the tube wall reveal that the fluid entrance velocity has a greater impact over the dynamics of the leaflet motion than the compression frequency of the tube wall.

This kind of information can be valuable to the medical and pharmaceutical communities. Thus, this type of fundamental model can provide a means to investigate different fluid flow dynamics and direct experimental work for validation and further investigations. The contributions of this chapter are as follows.

- A two-dimensional model developed in chapter 4 is used to study the dynamics of the human vein and valve system in the legs. The model and solution environment permitted the spatial and temporal variation in the fluid and structural variable properties in all locutions of the system,including the locations where these properties cannot be estimated by experimental means with out affecting the integrity of the system.

- It is important to understand the nature of vortex shedding at the leaflet edge , as excessive shedding may damage the leaflet edge. Damaged leaflet edges may trigger the process of thrombi (blood clots) formation in a later stage. The simulated results showed the formation and breakaway of vortices (vortex shedding) at the leaflet's free edge at normal flow and tube conditions.

- Due to the model's flexibility the model was used to predict the impact of several variables and conditions on the overall dynamics of the system.

## 5.6 NOMENCLATURE

| | |
|---|---|
| $F_{b_{x_i}}$ | Fluid forces acting on the flexible structures for directions $i = 1, 2$ $(Pa)$ |
| $F_{x_i}$ | Body forces acting on the flexible structure for directions $i = 1, 2$ $(Pa)$ |
| $P_d$ | Down stream exit fluid pressure $(Pa)$ |
| $T$ | Temperature $(C^\circ)$ |
| $T_c$ | Cycle duration $(s)$ |
| $U$ | Displacement in axial direction $(m)$ |
| $U_{max}$ | Maximum axial velocity at entrance $(m/s)$ |
| $V$ | Displacement in radial direction $(m)$ |
| $c$ | Relative convective velocity of the material in spatial domain $(m/s)$ |
| $g_{x_i}$ | Fluid gravitational force $(Pa)$ |
| $p(x_1, x_2, t)$ | Fluid pressure $(Pa)$ |
| $t$ | Time $(s)$ |
| $u_1(x_1, x_2, t)$ | Axial fluid velocity $(m/s)$ |
| $u_2(x_1, x_2, t)$ | Radial fluid velocity $(m/s)$ |
| $x_1$ | Axial coordinate $(m)$ |
| $x_2$ | Radial coordinate $(m)$ |
| $\dot{\gamma}$ | Fluid shear rate $(s^{-1})$ |
| $\dot{\gamma}_c$ | Critical Shear rate $(s^{-1})$ |
| $\delta_{max}$ | Maximum displacement of the tube $(m)$ |
| $\varepsilon_{x_i}$ | Material shear strain |
| $\varepsilon_{x_i}$ | Material strain in $i$ direction , for i=1,2 |
| $\mu$ | Dynamic blood viscosity $(Pa/s)$ |
| $\mu_f$ | Plasma viscosity $(Pa/s)$ |
| $\mu_o$ | Constant fluid dynamic viscosity $(Pa/s)$ |
| $\mu_{37}$ | Plasma viscosity at 37° C$(Pa/s)$ |
| $\sigma_{x_i}$ | Material stress in $i$ direction , for i=1,2 $(Pa)$ |
| $\tau_{x_1x_2}$ | Material shear stress $(Pa)$ |

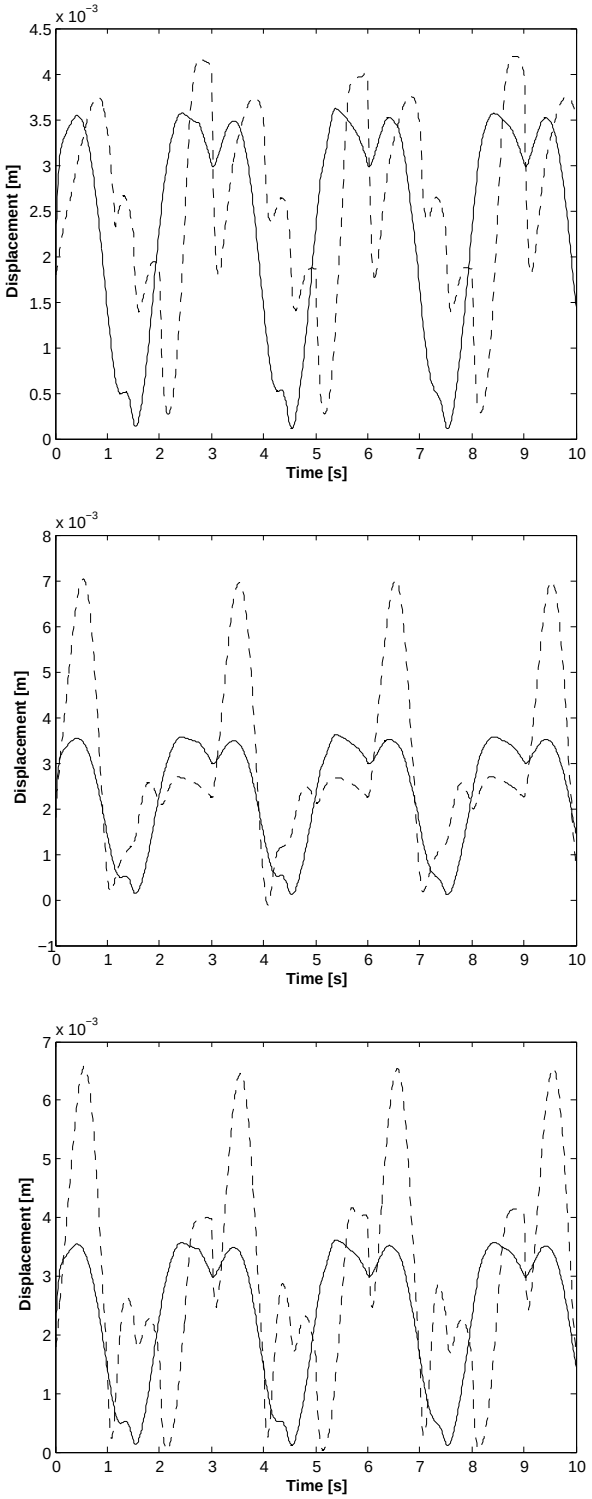


Figure 5.27. Sensitivity analysis to varying boundary conditions. (Solid line: Base Case. Dashed line: Trial case.) Top: Compression frequency of the tube wall. Middle: fluid velocity frequency. Bottom: compression frequency and fluid velocity frequency.

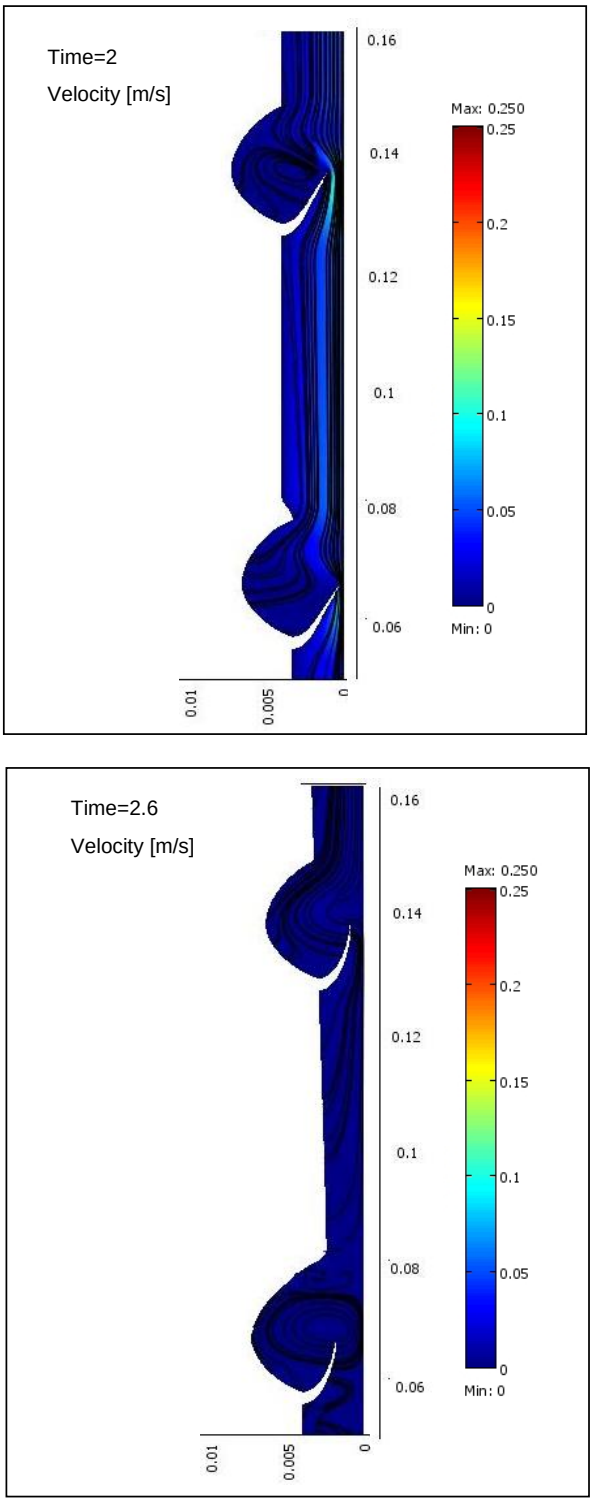


Figure 5.28. Streamlines in a double leaflet system: closing and opening of the first leaflet. The scale on the left is velocity. Abscissa: Diameter of tube in meters. Ordinate: Length of tube in meters.

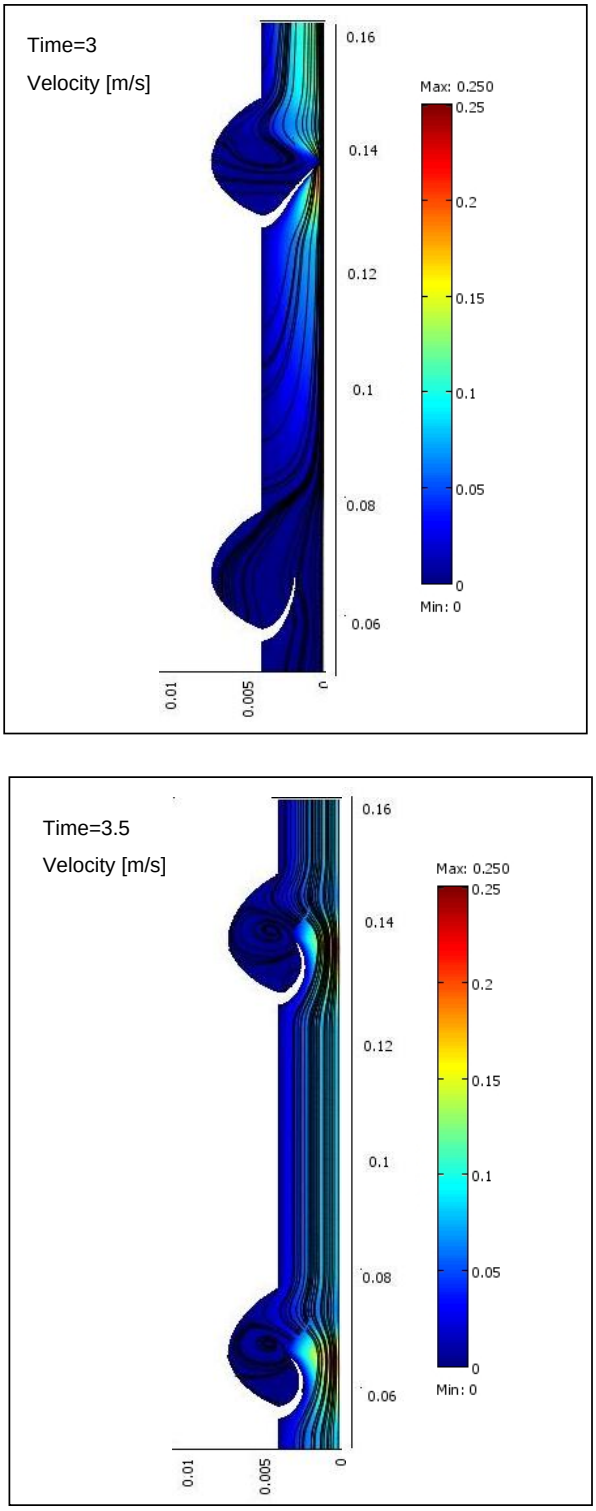


Figure 5.29. Streamlines in a double leaflet system: closing and opening of the second leaflet. The scale on the left is velocity. Abscissa: Diameter of tube in meters. Ordinate: Length of tube in meters.

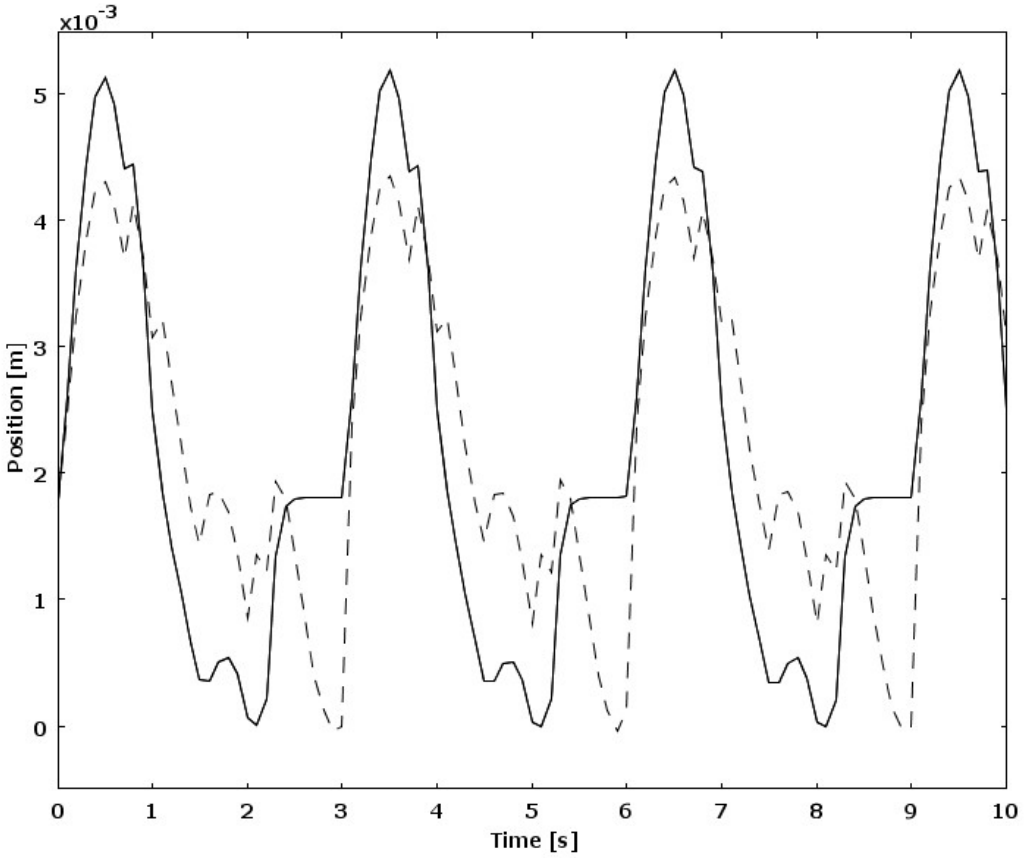


Figure 5.30. Displacement of the leaflet free edge: leaflet 1 (Solid line); leaflet 2 (Dashed line).

# CHAPTER 6
# SUMMARY AND CONTRIBUTIONS

In chapter 2, fluid flow separation and reattachment is common occurrence in the flexible tubes. It is important to understand the factors that promote these conditions and to mitigate any adverse effects associated with them. A one-dimensional model of fluid flow in a flexible channel [35] was used to develop new fluid separation and reattachment criteria. These criteria are based on the presence of an adverse pressure gradient and change in the total energy gradient, respectively. The new criteria are based on measurable quantities such as fluid pressure and fluid velocity. Fluid flow experiments at low Reynolds number flow were carried out and the experimental data compared to the model's predictions. The predictions were found to be qualitatively satisfactory; the differences were attributed to either experimental errors or parameter uncertainties.

Further numerical analysis of the merit of a closed-form solution to the one-dimensional model is carried out using the method of characteristics. The purpose was primarily to reduce the computational burden but also to investigate the limiting behavior of the model. In particular, the original solution was obtained assuming a quartic function for the fluid velocity. Here, a quadratic velocity profile was assumed. The analysis of the solution obtained with this assumption showed that there can be multiple locations for flow separation and flow re-attachment to occur. Additionally, the locations of flow separation and re-attachment points were found based on the criteria provided in [34] and these multiple locations were observed in the experiment discussed in chapter 2.

A model for a two-dimensional mathematical representation of a flexible tube and double leaflet valve system was developed in chapter 4. The fluid domain assumes

non-Newtonian fluid properties and the solid domain assumes linear isotropic elastic properties. Here, the dynamics of the fluid domain were modeled using conservation of mass and momentum principles and the flexible domain dynamics were modeled considering Newton's second law. The motion of the leaflet and the tube wall introduces non-stationary boundary conditions. Thus, the mathematical description of this system involves multi-dimensional fluid dynamics and non-linear solid mechanics resulting in a system of nonlinear partial differential equations with moving boundary conditions. To solve this system of equations, the numerical formulation of the fluid domain was transformed from the usual Eulerian framework to the Arbitrary Lagrangian-Eulerian ALE framework. The solid domain remained in a Lagrangian framework.

A case study (see chapter 5) using the vein and venous valve found in the legs of humans is presented to compare known behavior to the numerical solution predictions. Two viscosity models are used to represent the complex stress-strain relationship of blood that contributed to the non-Newtonian properties of the system. The model enabled an estimation of the extent of valve opening and closing as a function of the fluid dynamics and fluid-structure interactions. The Femlab® environment was used to solve the model and its capabilities permitted visualization of the formation of vortices and their role in flow regulation and leaflet motion. The simulated results showed the formation and breakaway of vortices (vortex shedding) at the leaflet's free edge. It is important to understand the nature of vortex shedding at the leaflet edge, as excessive shedding may damage the leaflet edge. Damaged leaflet edges may trigger the process of thrombi (blood clots) formation in a later stage. Stress analysis on the leaflet enabled the identification of those locations that were under higher stresses.

A parameter sensitivity analysis on the elasticity of the system confirms that an increase in the elastic modulus of the leaflet affects the closing of the leaflet.

A sensitivity analysis on the boundary conditions involving entering fluid velocity and external compression of the tube wall reveal that the fluid entrance velocity has a greater impact on the dynamics of the leaflet motion than the compression frequency of the tube wall. This kind of information can be valuable to the medical and pharmaceutical communities. Thus, this type of fundamental model can provide a means to investigate different fluid flow dynamics and direct experimental work for validation and further investigations.

The contribution of this study as follows.

- The criteria proposed by [34] for flow separation and re-attachment are validated numerically.
- Model predictions at low Reynolds number flow are qualitatively compared to experimental data.
- An approximate analytical solution to the model developed in chapter 2 is arrived at using the method of characteristics. This approach served to reduce the computational burden associated with solving an infinite dimensional problem and to provide valuable insights into the behavior of the collapsible channel.
- The locations of flow separation and re-attachment points are found based on the criteria provided in [34].
- The analytical solution confirmed the existence of multiple points of collapse, which was observed in the experimental data discussed in section 2.3.
- A two-dimensional mechanistic PDE model is derived to represent blood flow in the vein and venous valve using the conservation of mass and momentum principles.

- The motion of the flexible valve leaflet and vein wall introduce non-stationary system boundaries.

- The fluid domain is modeled using an ALE frame work to provide an accurate numerical solution while tracking the moving boundaries.

- Two viscosity models are used to represent the complex stress-strain relationship of the fluid.

- A two-dimensional model developed in chapter 4 is used to study the dynamics of the human vein and valve system in the legs. The model and solution environment permitted the spatial and temporal variation in the fluid and structural variable properties in all locutions of the system,including the locations where these properties cannot be estimated by experimental means with out affecting the integrity of the system.

- It is important to understand the nature of vortex shedding at the leaflet edge, as excessive shedding may damage the leaflet edge. Damaged leaflet edges may trigger the process of thrombi (blood clots) formation in a later stage. The simulated results showed the formation and breakaway of vortices (vortex shedding) at the leaflet's free edge at normal flow and tube conditions.

- Due to the model's flexibility the model was used to predict the impact of several variables and conditions on the overall dynamics of the system.

# CHAPTER 7
# FUTURE WORK

In this work the fluid dynamics that involves flexible tubes with and without internal flexible structures has been investigated. Furthermore, fluid properties such as Newtonian, non-Newtonian and isotropic linear material properties for flexible structure are incorporated.

1. The one-dimensional model proposed by Pedley[35] was used to predict the low Reynolds number flow. The model predictions were compared to experimental data. However, the experimental data were confined to pressure and flow rate measurement. As future work, the extent of the tube collapse or expansion is expected to be estimated using images (CCD camera and arthroscopic device) captured during the experiments. This will enable the establishment of a relationship between fluid pressure, fluid velocity, and the tube flow area. The tubing used in the experiments was translucent. To assist in future flow visualization experiments a transparent flexible tube is recommended.

2. The approximate analytical solution obtained to the one-dimensional model considered a quadratic velocity profile with constant coefficients in each region. For more accurate results, time dependent coefficient are suggested as future work.

3. The mathematical formulation of the fluid structure interactions in a flexible tube with embedded leaflets considered linear isotropic elastic properties for the flexible structures. However, these structures exhibit anisotropic, nonlinear elastic properties. Also some non-Newtonian fluids exhibit viscoelastic properties. The impact of these properties may produce asymmetric dynamics. Investigat-

ing the impact of these properties is recommended.

4. The analysis was confined to a two-dimensional mathematical formulation. This enabled the exclusion of circumferential bending and torsion that can occur in real systems. In order to capture the substantial dynamics a three-dimensional mathematical should be investigated.

5. The mathematical concept presented in the general modeling chapter is expected to be transferrable to other application areas to provide a mathematical foundation to model fluid structure interactions in flexible structures with embedded internal flexible structures. The advantages of using this type of fluid structure interaction model include: (1) The incorporation of the natural geometry which allows the forces to act continuously on the structures. (2) The assumption of a continuum, which reduces the numerical errors introduced by the bio-mechanical model. (3) The use of the ALE framework to capture the fluid dynamics and the moving boundaries.

6. There are several numerical techniques available to model to fluid structure interactions with moving boundaries other than ALE method. These methods includes fictitious boundary method, immersed boundary method, and level set method. All these methods have certain advantages and disadvantages over each other. This study did not consider comparing different numerical techniques. A comparison study is recommended for future work.

# APPENDIX A

# MODEL DERIVATION OF A FLEXIBLE TUBE

## A.1 Conservation of Mass

The conservation of mass involves relating mass within the unit length of the conduit to the physical quantities that vary with time and space. Hence, conservation of mass within the conduit is a function of the fluid properties. In free surface fluid flow, the height of the free surface as measured from a fixed point relates to the fluid mass in the conduit (See appendix B for the derivation). Here, the transverse height, which is in the $\tilde{y}$-direction directly affects fluid flow velocity and the internal pressure distribution. Hence, the physical quantity that affects the mass within the conduit is the transverse height of the conduit. The conservation of mass equation for an infinitesimal control volume of the collapsible tube in a horizontal geometry is given by [35],

$$\rho\tilde{h}_{\tilde{t}} + \rho\tilde{\bar{u}}\tilde{h}_{\tilde{x}} = -\rho\tilde{\bar{u}}_{\tilde{x}}\tilde{h} \tag{A.1}$$

where $\rho$ is the fluid density, $\tilde{h}(\tilde{x},\tilde{t})$ is the vertical position of the tube wall, $\tilde{u}(\tilde{x},\tilde{y},\tilde{t})$ is the instantaneous velocity, and $\tilde{\bar{u}}$ is the mean velocity given by

$$\tilde{\bar{u}} = \frac{1}{\tilde{h}}\int_0^{\tilde{h}} \tilde{u}\, dy \tag{A.2}$$

Define the fluctuation in the velocity by,

$$\tilde{\acute{u}}(\tilde{x},\tilde{y},\tilde{t}) = \tilde{u}(\tilde{x},\tilde{y},\tilde{t}) - \tilde{\bar{u}}(\tilde{x},\tilde{t}). \tag{A.3}$$

where $\acute{u}(x, y, t)$ is the fluctuation. These quantities all are functions of the spatial variable, $\tilde{x}$, and time, $\tilde{t}$.

Using the definitions listed in Table 2.1, the dimensionless form of Equation (A.1) given by,

$$\rho h_t + \rho \bar{u} h_x = -\rho \bar{u}_x h. \tag{A.4}$$

## A.2 Conservation of Momentum

An application of the conservation of momentum is based on balancing the rate of change in the momentum of the control volume of the fluid to the net forces acting on the fluid. The acceleration component consists of transient and convective changes in the acceleration of the fluid. Since the forces are on a moving fluid in a horizontal direction, gravitational forces can be neglected. In general the longitudinal fluid velocity $\tilde{u}$ is a function of time and the longitudinal ($x$) and transverse ($y$) coordinates [4]. The momentum balance is a one-dimensional Navier-Stokes equation given by,

$$\frac{\partial \tilde{u}}{\partial \tilde{t}} + \tilde{u}\frac{\partial \tilde{u}}{\partial \tilde{x}} = \frac{1}{\rho}\left(-\frac{\partial \tilde{p}}{\partial \tilde{x}} + \mu\left[\frac{\partial^2 \tilde{u}}{\partial \tilde{x}^2} + \frac{\partial^2 \tilde{u}}{\partial \tilde{y}^2}\right]\right) \tag{A.5}$$

where $\rho$ and $\mu$ represent the density and the viscosity of the fluid, respectively; and the forces on the right hand side are the pressure and viscous forces.

Viscous effects are more significant along the transverse direction as compared to the longitudinal direction when the tube is sufficiently long. Therefore, the second derivative of the fluid velocity in the longitudinal direction is negligible compared to the derivative in the transverse direction. Thus, the term $\partial^2 \tilde{u}/\partial^2 x$ can be eliminated from the above equation.

Using the definitions provided in Table 2.1 and Equation (A.3), the dimensionless

form of the above equation is given by,

$$\frac{\partial u}{\partial t} + u\frac{\partial u}{\partial x} = -\frac{\partial p}{\partial x} + Re^{-1}\frac{\partial^2 \acute{u}}{\partial y^2}. \tag{A.6}$$

Accounting for energy losses due to flow re-attachment as a result of divergence and separation of the fluid at the downstream end is important as these losses have a direct impact on the instantaneous velocity. Since it is difficult to account for all sources of energy losses on the instantaneous velocities, their effects on the average velocities are considered instead. Cancelli and Pedley [31] defined the velocity fluctuation component as the difference between the instantaneous velocity and the average velocity. In addition the sum of the velocity fluctuation components in the transverse direction for all longitudinal positions are assumed to be zero. This definition for the instantaneous velocity in terms of the velocity fluctuation component motivates the use of an integral form of the momentum balance given by, (see section A.4 for the derivation) [31],

$$\bar{u_t} + \bar{u}\bar{u}_x + \frac{1}{2h}\frac{\partial}{\partial x}\left[\int_o^h \acute{u}^2 dy\right] = -p_x + \left(\frac{Re^{-1}}{h}\right)[\acute{u}_y]\Big|_0^h. \tag{A.7}$$

## A.3 Equation of State

The external and internal pressures induce moments and forces on the conduit's flexible wall. Being elastic, the tube wall's compliance will cause the fluid pressure, flow area, and hence the fluid velocity to change. A balance of the forces and the moments acting on an element of the tube wall leads to an equation of state, which in this case is the *tube law* [7]. The forces and the moments that may be induced on the tube wall are longitudinal tension and bending and circumferential bending.

In one-dimensional fluid flow, the cross-sectional area $\tilde{A}$ of the tube, the internal pressure $\tilde{p}$, and the average velocity $\tilde{\bar{u}}$ are functions of $\tilde{x}$ and $\tilde{t}$. When the tube law

applies and considering circumferential bending only, the elastic properties can be modeled by [7],

$$\tilde{p} - \tilde{p_e} = K_p P(\alpha) \tag{A.8}$$

where $\alpha = \tilde{A}/\tilde{A}_o$, $\tilde{A}_o$ is the un-deformed cross-sectional area, and $K_p$ is the circumferential bending stiffness coefficient. The stiffness coefficient $K_p$ is a material property of the tube and depends on the thickness of the tube, the modulus of elasticity and the Poisson ratio[1]. When both longitudinal tension and longitudinal bending are present, Equation (A.8) becomes [24],

$$\tilde{p} - \tilde{p_e} = K_p P(\alpha) - \frac{\tilde{T}}{\tilde{R}} - \mathcal{E} I \frac{\partial^4 \tilde{y}}{\partial \tilde{x}^4} \tag{A.9}$$

where $\tilde{R}$ is the longitudinal radius of curvature, $\mathcal{E}$ is modulus of elasticity, and $\mathcal{I}$ is the moment of inertia. If the tube has very thin walls then the contribution of circumferential and longitudinal bending are negligible thus, Equation (A.9) becomes

$$\tilde{p} - \tilde{p_e} = -\frac{\tilde{T}}{\tilde{R}} \tag{A.10}$$

For a two-dimensional Cartesian coordinate system, the radius of curvature is given by [24]

$$\frac{1}{\tilde{R}} = \frac{\tilde{h}_{\tilde{x}\tilde{x}}}{\left[1 + \left(\tilde{h}_{\tilde{x}}\right)^2\right]^{-3/2}}. \tag{A.11}$$

Substitution of the above into Equation (A.10) and applying the definitions in Table 2.1 give the following dimensionless form of the tube law,

$$p_e - p = \frac{T h_{xx}}{(1 + {h_x}^2)^{3/2}}. \tag{A.12}$$

[1]The ratio of transverse contraction strain to the longitudinal extension strain in the direction of the stretching force.

## A.4 Derivation of Equation (2.5)

Using the relationships defined in Table 2.1, Equation (A.5)is converted to the following dimensionless form,

$$u_t + uu_x = p_x + Re^{-1}u_{yy}. \tag{A.13}$$

Integrating this equation across the channel width yields equation (2.5). The derivation of each component of this equation is as follows.

$$u(x,y,t) = u(\bar{x},t) + \acute{u}(x,y,t) \tag{A.14}$$

$$\bar{u} = \frac{1}{h(x,t)}\int_0^h u dy \tag{A.15}$$

$$\int_0^h \acute{u} dy = 0 \tag{A.16}$$

The above equations enables the derivation of the following derivatives,

$$u_t = \bar{u_t} + \acute{u}_t$$

$$u_x = \bar{u_x} + \acute{u}_x$$

$$u_{yy} = \acute{u_{yy}}.$$

The integration of first term in Equation (A.13) is given by,

$$\int_0^h u_t dy = \int_0^h \bar{u_t} dy + \int_0^h \acute{u}_t dy \tag{A.17}$$

From Equation (A.16) it can be seen last term on the right of Equation (A.17) is zero. Thus,

$$\int_0^h u_t dy = \bar{u}_t h. \tag{A.18}$$

The integration of second term in Equation (A.13) is given by,

$$\int_0^h uu_x dy = \int_0^h \bar{u}\bar{u_x} dy + \int_0^h \bar{u}\acute{u}_x dy + \int_0^h \acute{u}\bar{u_x} dy + \int_0^h \acute{u}\acute{u}_x dy \tag{A.19}$$

It can be shown that the second and third terms on the right hand side of the above equation are equal to zero and the first and last terms can be re-written as,

$$\int_0^h uu_x dy \int_0^y \acute{u}\acute{u}_x dy = \frac{\partial}{\partial x} \int_0^y \acute{u}^2 dy. \tag{A.20}$$

The integration of first and second terms on the right side of Equation (A.13) is given by,

$$\int_0^y p_x dy = p_x h(x,t) \tag{A.21}$$

$$\int_0^y u_{yy} dy = \int_0^y \acute{u}_{yy} dy = \acute{u}_y \Big|_0^h. \tag{A.22}$$

This completes the derivation.

# APPENDIX B

## DERIVATION OF CONSERVATION OF MASS EQUATION FOR FREE SURFACE FLOW

Consider infinitesimal control volume as shown in Figure(B.1).

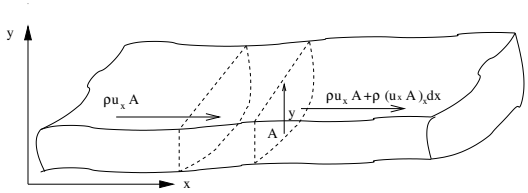


Figure B.1. Free surface flow channel.

This infinitesimal slice of the fluid is normal to $x$ direction and corresponds to the geometry at time $t$. Suppose the free surface is approximately horizontal. Then an application of the conservation of mass to this small volume in the longitudinal direction yields,

$$-\rho\bar{u}A + [\rho\bar{u}A + \rho\frac{\partial}{\partial x}(\bar{u}Adx)] + \rho\frac{\partial A}{\partial t}dx = 0 \tag{B.1}$$

where $A, \bar{u}, \rho$ are cross-sectional area, average velocity and the fluid density. Simplifying this equation yields,

$$\bar{u}\frac{\partial A}{\partial x} + A\frac{\partial \bar{u}}{\partial x} + \frac{\partial A}{\partial t}x = 0 \tag{B.2}$$

Assuming that the area $A$ is proportional to height $h$, Equation (B.2) can be re-written to arrive at the following expression,

$$\bar{u}\frac{\partial h}{\partial x} + h\frac{\partial \bar{u}}{\partial x} + \frac{\partial h}{\partial t}x = 0. \tag{B.3}$$

# APPENDIX C

# ARBITRARY LAGRANGIAN-EULERIAN METHOD

## C.1 Lagrangian Formulation

The following material is summarized from the work of [2]. This formulation is used primarily in solid mechanics where each individual mesh follows the associated material particle during its motion (see top panel of Figure C.1). The Lagrangian description allows easy tracking of the free surfaces and interfaces of different materials. However, in order to produce accurate results this formulation requires frequent re-meshing of the system when large deformations occur.

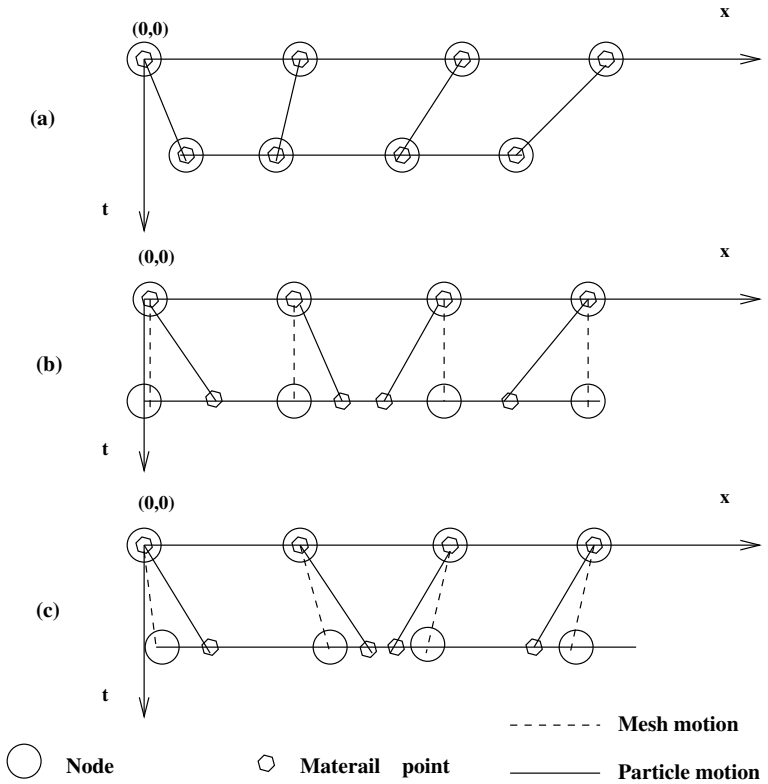


Figure C.1. One-dimensional representation of (a) Lagrangian, (b) Eulerian, and (c) *ALE* mesh and particle motion [2].

There are two domains used in continuum mechanics, the spatial and material

domains.

1. Material domain - $R_X \subset \mathbb{R}^{n_{sd}}$, each $n_{sd}$ spatial dimension consists of material points $X$.

2. Spatial domain - $R_x$ consist of spatial points $x$.

The computational mesh follows the motion of the continuum. Thus, the material points of the continuum are permanently fixed to the grid nodes of the computational mesh. This enables a definition of a reference configuration in the Lagrangian formulation using the initial configuration defined by the material points (i.e. material coordinates $X$) in the material domain (see Figure C.2) [2]. The motion of the mate-

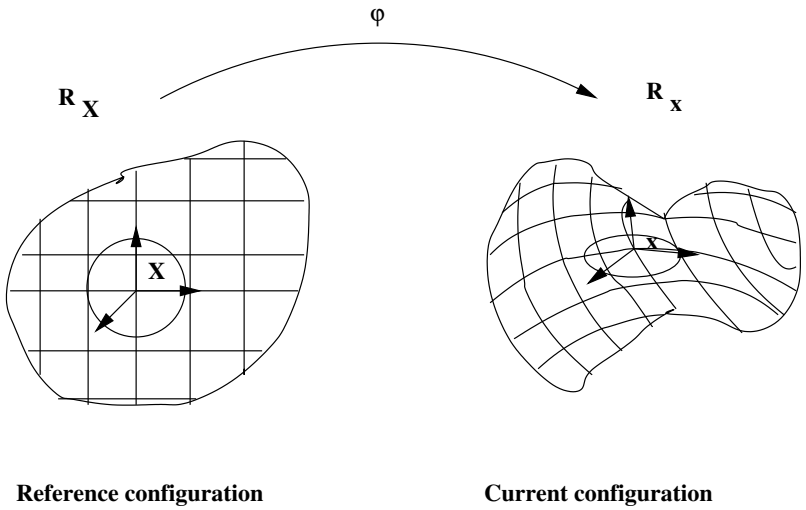


Figure C.2. Lagrangian description of motion [2].

rial points relates the material coordinates $X$ to the spatial coordinates $x$. Consider a one-to-one mapping of the function $\varphi$ from the material reference frame to the spatial reference frame. The mapping between the two reference frames is given by,

$$\begin{aligned} \varphi : R_X \times [t_0, t_{final}] &\rightarrow R_x \times [t_0, t_{final}] \\ (X, t) &\rightarrow \varphi(X, t) = (x, t) \end{aligned} \tag{C.1}$$

where $t_0$ and $t_{final}$ define the initial and final computing times, respectively. The material coordinate $X$ relates to the spatial coordinate $x$ in time $t$ by the law of motion,

$$x = x(X, t) \quad \forall\, t \tag{C.2}$$

Therefore, for every time $t$, the map $\varphi$ defines a configuration in the spatial domain. This enables us to define a material velocity $v$ for a fixed material point $X$, that is,

$$v(X, t) = \left.\frac{\partial x}{\partial t}\right|_X . \tag{C.3}$$

In order to ensure a one-to-one mapping of the function $\varphi$, the term $\partial x/\partial X$ must have a positive value. This non-zero condition provides the required condition for the existence of the inverse function, $\varphi^{-1}$. The positivity of the above term guarantees no orientation changes in the references axes at each point $X$ at time $t > t_0$. Using the inverse function it is possible to track the history of the motion of a particular material point $X$,

$$(X, t) = \varphi^{-1}(x, t). \tag{C.4}$$

In the Lagrangian formulation there are non-convective effects as the material point coincides with the same grid points during the motion.

## C.2 Eulerian Formulation

The following material is summarized from the work of [2]. This method is applied mainly to fluid mechanics where the computational mesh is fixed and the continuum moves with respect to a grid (see middle panel of Figure C.1) [2]. This formulation consists of examining the variations in the physical quantities associated with the fluid particles passing a fixed computational grid over the time. Thus, in this method the computational grid is fixed and the continuum is moved (including the material

points) with respect to the computational grid. This disassociation of material particles from the mesh grid introduces a convective effect due to the relative motion of the deforming material points with respect to the fixed computational grid. Here, the conservation equations are formulated in terms of the spatial coordinates $x$ and time $t$ leaving the Eulerian description of motion to consider the variables and functions that have instantaneous significance in a fixed region in space.

The material velocity $v$ at a given computational node is the velocity of the material point. This enables a definition of the material velocity $v = v(x, t)$ with respect to a fixed computational mesh thereby eliminating the necessity of a reference initial configuration of the continuum and material coordinate. With the Eulerian description it is easy to follow a large deformation but a precise kinematic description of the interfaces and flow resolutions are required.

## C.3 Arbitrary Lagrangian-Eulerian Formulation

The ALE formulation makes use of the best features of both the Lagrangian and Eulerian approaches. In the ALE method the computational mesh may be allowed to move with the continuum similar to the Lagrangian method or the mesh can be fixed as in the Eulerian method or the mesh can move in a specified manner to provide continuous re-zoning (see bottom panel of Figure C.1) [2].

## C.4 Relative Motion Among The Spatial, Material, And The Reference Configuration

When ALE formulation is introduced with an arbitrarily moving computational grid, an additional reference configuration $R_{\mathcal{X}}$ is need to be defined. Here the computational grid is defined in the reference domain hence reference points $\mathcal{X}$ are introduced to identify the grid points. Note that in the *ALE* formulation both reference

and material domain move and their relative motion in the spatial domain need to be estimated. Figure (C.3) illustrates the relationship among three configurations (i.e.

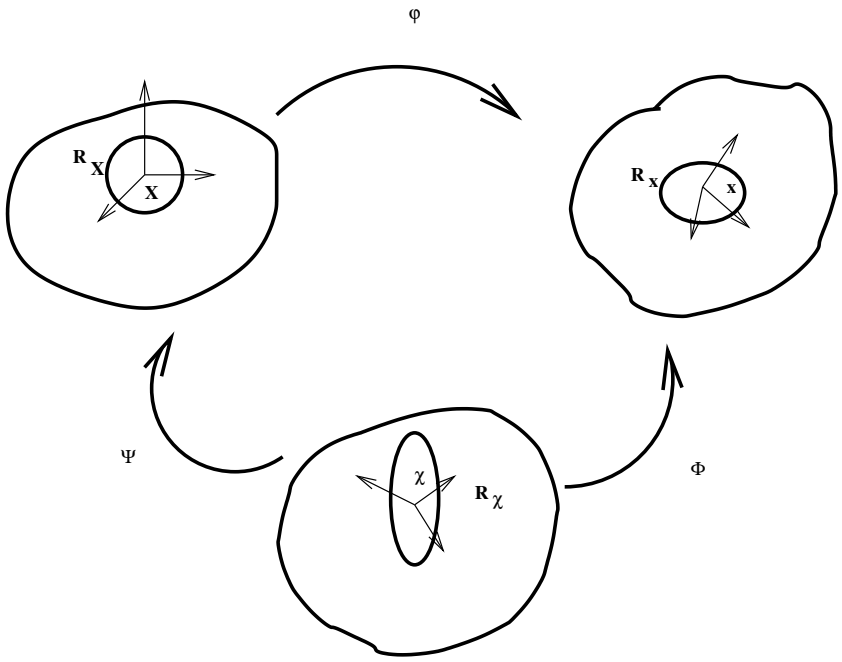


Figure C.3. Relationship among spatial, referential and material frames [2].

material, spatial, and the reference),where $\Phi$,and $\Psi$, referred to mapping of referential domain $R_{\mathcal{X}}$ to spatial domain and the material domain respectively. The function $\varphi$ is the mapping from $R_X$ to $R_x$. Thus, the motion of a material point in the spatial domain can be expressed as follows,

$$\varphi = \Phi \circ \Psi^{-1} \tag{C.5}$$

The motion of the material points in the spatial domain is given by,

$$\begin{aligned} \varphi : R_X \times [t_0, t_{final}] &\rightarrow R_x \times [t_0, t_{final}] \\ (X, t) &\rightarrow \varphi(X, t) = (x, t) \end{aligned} \tag{C.6}$$

Therefore, spatial coordinate $x$ can be represented as a function of the material coordinate $X$ and time $t$,

$$x = x(X,t) \quad t = t \tag{C.7}$$

This implies that the spatial coordinate $x$ is dependent on both $X$ and $t$. Thus, the velocity of a given material point in the spatial domain is given by,

$$v(X,t) = \left.\frac{\partial x}{\partial t}\right|_X . \tag{C.8}$$

The mapping $\Phi$ from $R_{\mathcal{X}}$ to $R_x$ can be understood as the motion of the grid points in the spatial domain,

$$\Phi : R_{\mathcal{X}} \times [t_0, t_{final}] \rightarrow R_x \times [t_0, t_{final}] \tag{C.9}$$

$$(\mathcal{X}, t) \rightarrow \Phi(\mathcal{X}, t) = (x, t) \tag{C.10}$$

$$\hat{v}(\mathcal{X}, t) = \left.\frac{\partial x}{\partial t}\right|_{\mathcal{X}} \tag{C.11}$$

where $\hat{v}$ is the mesh velocity.

The mapping from $R_X$ to $R_{\mathcal{X}}$ is interpreted as the material motion in the reference domain,

$$\Psi^{-1} : R_X \times [t_0, t_{final}] \rightarrow R_x \times [t_0, t_{final}] \tag{C.12}$$

$$(X, t) \rightarrow \Psi^{-1}(\mathcal{X}, t) = (\mathcal{X}, t) \tag{C.13}$$

$$w(X,t) = \left.\frac{\partial \mathcal{X}}{\partial t}\right|_X \tag{C.14}$$

where $w$ is the particle velocity in the $R_{\mathcal{X}}$ referential domain.

The relationship among velocities $v, \hat{v}$, and $w$ can be derived by differentiating

$\varphi = \Phi \circ \Psi^{-1}$,

$$\frac{\partial \varphi}{\partial (X,t)}(X,t) = \frac{\partial \Phi}{\partial (\mathcal{X},t)}(\Psi^{-1}(X,t))\frac{\partial \Psi^{-1}(X,t)}{\partial (X,t)}(X,t) \tag{C.15}$$

$$= \frac{\partial \Phi}{\partial (\mathcal{X},t)}(\mathcal{X},t)\frac{\partial \Psi^{-1}(X,t)}{\partial (X,t)}(X,t) \tag{C.16}$$

$$\tag{C.17}$$

Considering the time derivative components of the above differential form, the velocity relationship is,

$$\left.\frac{\partial x}{\partial t}\right|_X = \left.\frac{\partial x}{\partial t}\right|_{\mathcal{X}} + \frac{\partial x}{\partial \mathcal{X}}.w \tag{C.18}$$

$$v = \hat{v} + \frac{\partial x}{\partial \mathcal{X}}.w \tag{C.19}$$

Thus, the convective velocity $c$, i.e. the relative velocity between material and computational grid nodes, is given by,

$$c = v - \hat{v} = \frac{\partial x}{\partial \mathcal{X}}.w \tag{C.20}$$

## C.5 The Fundamental *ALE* Equation

It is necessary to define a relation between material (total) time derivative and the referential time derivative within *ALE* framework to express the conservation laws for mass, momentum, and energy.

### C.5.1 Material, spatial and referential time derivative

Consider physical scaler quantity, $f(x,t)$, $f^*(\mathcal{X},t)$, and $f^{**}(X,t)$ defined in spatial, referenial and material configurations respectively. Since particle motion $\varphi$ is a mapping,the spatial description of the physical quantity $f(x,y)$ is related to the

material description of the physical quantity $f^{**}(X,t)$ by

$$f^{**}(X,t) = f(x,t) = f((\varphi X,t),t) \tag{C.21}$$

$$f^{**} = f \circ \varphi \tag{C.22}$$

Thus, differentiating the material time derivative and the spatial time derivative are related by,

$$\left.\frac{\partial f^{**}}{\partial t}\right|_X = \frac{\partial f}{\partial t} + \frac{\partial f}{\partial x}.\left.\frac{\partial x}{\partial t}\right|_X = \frac{\partial f}{\partial t} + \frac{\partial f}{\partial x}.v \tag{C.23}$$

Therefore the relationship between material and the spatial time derivative can be expressed as (by dropping $*$ notation),

$$\left.\frac{\partial f}{\partial t}\right|_X = \left.\frac{\partial f}{\partial t}\right|_x + v.\nabla f \tag{C.24}$$

This represents the variation of the physical quantity for a given particle $X$,by the sum of the local variation and the convective term which takes the account of the relative motion of the material and the spatial system.

In order to extend the relation between material and spatial time derivatives in to referential time derivative the following mapping is considered.

$$f^{**} = f^{*} \circ \Psi^{-1} \tag{C.25}$$

by differentiating Equation (C.25) with respect to time ($t$)for a fixed material coordinates $X$,

$$\left.\frac{\partial f^{**}}{\partial t}\right|_X = \left.\frac{\partial f^{*}}{\partial t}\right|_{\mathcal{X}} + \left.\frac{\partial f^{*}}{\partial \mathcal{X}}\frac{\partial \mathcal{X}}{\partial t}\right|_X = \frac{\partial f^{*}}{\partial t} + \frac{\partial f^{*}}{\partial \mathcal{X}}.w \tag{C.26}$$

This equation relates material and the referential time derivatives. By using the

Equations (C.20) and (C.26) the fundamental $ALE$ relation between material time derivatives, referential time derivatives and the spatial gradient can be given by,

$$\left.\frac{\partial f}{\partial t}\right|_X = \left.\frac{\partial f}{\partial t}\right|_\chi + \frac{\partial f}{\partial x}.c = \left.\frac{\partial f}{\partial t}\right|_\chi + c.\nabla f \tag{C.27}$$

This can be interpreted as the time derivative of the physical quantity $f$ for a give particle $X$ in spatial domain, as the sum of the local time derivative with respect to reference coordinate system and the convective term that takes into account of the relative velocity $c$ between the material and the referential system.

# APPENDIX D

## COMSOL MODEL - SINGLE VALVE

## 1. Table of Contents



## 2. Model Properties

| Property | Value |
|---|---|
| Model name | Singlevalve |
| Author | Nilmini Wijeratne |
| Company | Texas Tech University |
| Department | Chemical Engineering |
| Reference | |
| URL | |
| Saved date | Dec 16, 2007 11:44:15 PM |
| Creation date | Aug 9, 2007 11:48:22 AM |
| COMSOL version | COMSOL 3.3.0.511 |

File name: C:\Users\nilmini\Research\Femlabfiles\test9-13.mph

Application modes and modules used in this model:

- Geom1 (2D)
  - Non-Newtonian Flow (Chemical Engineering Module)
  - Plane Strain
  - Moving Mesh (ALE)

## 3. Constants

| Name | Expression | Value | Description |
|---|---|---|---|
| rho | 1060 | | |
| g | 9.81 | | |
| h1 | 0.18 | | |
| u_amp | 0.75 | | |
| delta_max | 0.004 | | |

| | | | |
|---|---|---|---|
| C | 0.3 | | |
| T1 | 28 | | |
| nu1 | 0.021 | | |
| mu37 | 1.4*10^(-3) | | |

### 4. Global Expressions

| Name | Expression | Description | |
|---|---|---|---|
| u_max | u_amp*A | | |
| A | (abs(sin(2*pi*t/3))+sin(2*pi*t/3))/2 | | |
| k0 | exp(3.874-10.41*C+13.8*C^2-6.738*C^3) | | |
| k1 | exp(1.3435-2.803*C+2.711*C^2-0.6479*C^3) | | |
| gC | exp(-6.1508+27.923*C-25.6*C^2+3.697*C^3) | | |
| B | (-abs(sin(2*pi*t/3))+sin(2*pi*t/3))/2 | | |
| N1 | (abs(sin(2*pi*t/3)+sin(2*pi*t/1.5)) + (sin(2*pi*t/3)+sin(2*pi*t/1.5))) /2 | | |
| N2 | (-abs(sin(2*pi*t/3)+sin(2*pi*t/1.5)) + (sin(2*pi*t/3)+sin(2*pi*t/1.5))) /2 | | |

### 5. Geometry

Number of geometries: 1

#### 5.1. Geom1

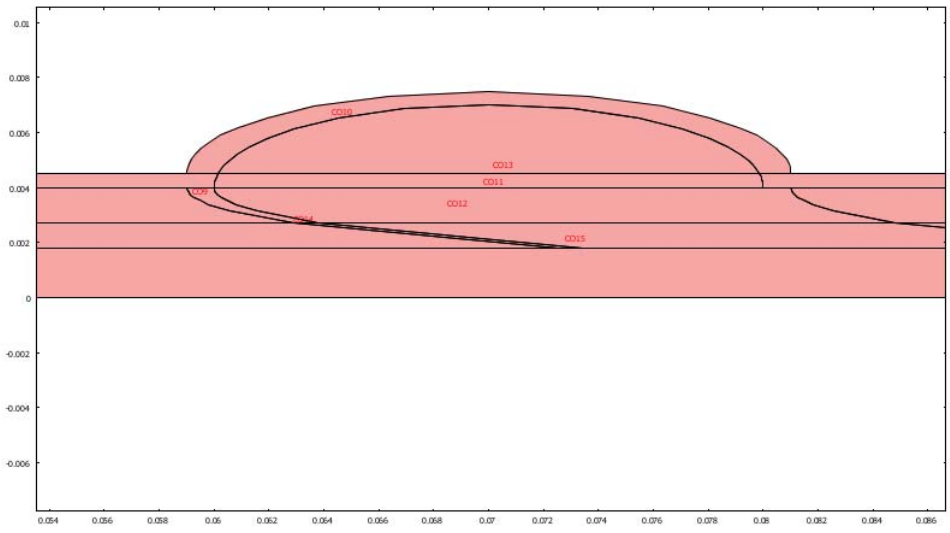

### 5.1.1. Point mode

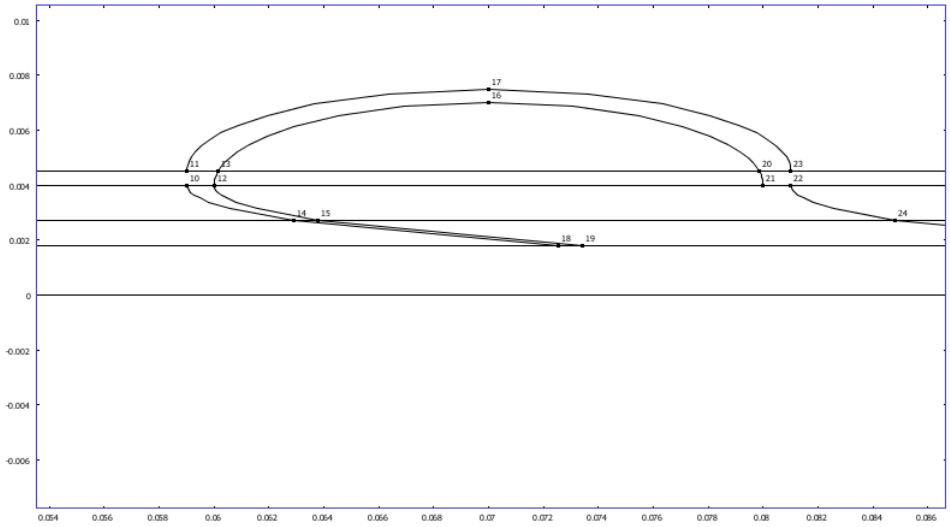

### 5.1.2. Boundary mode

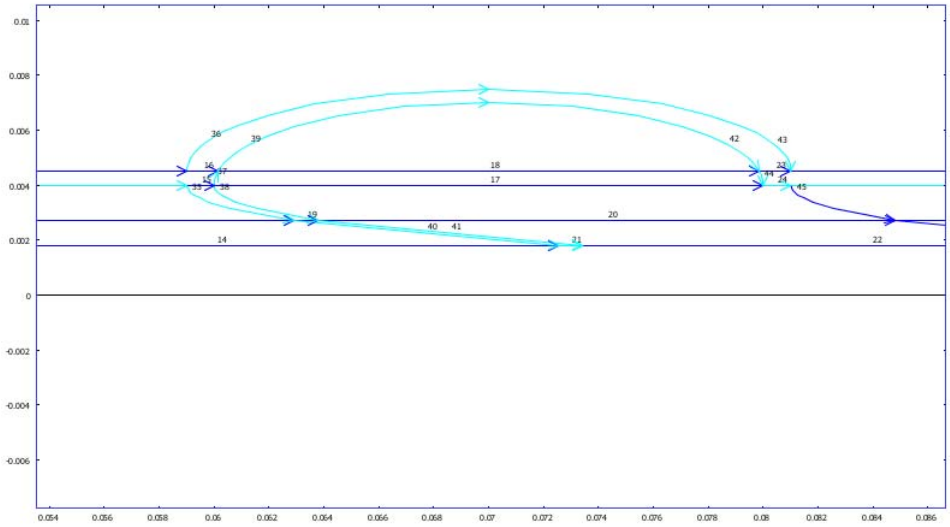

### 5.1.3. Subdomain mode

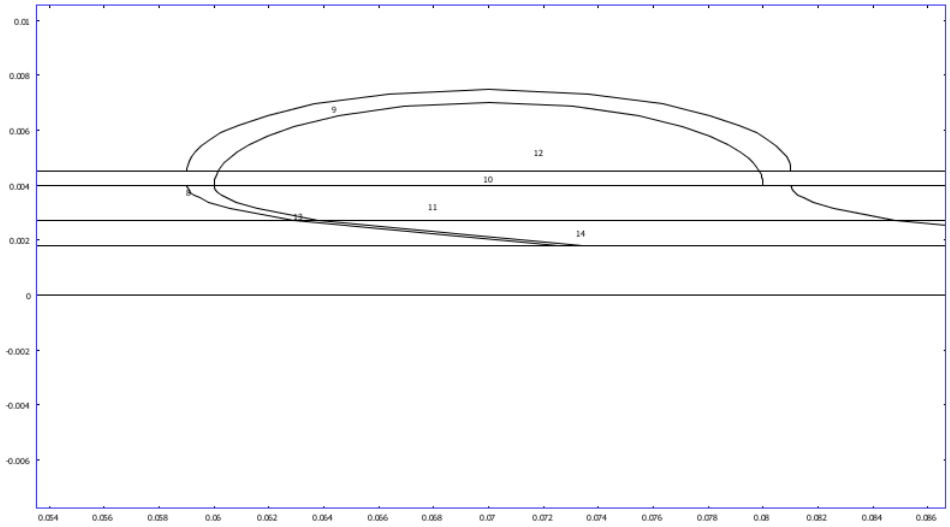


## 6. Geom1

Space dimensions: 2D

Independent variables: X, Y, Z

### 6.1. Expressions

### 6.1.1. Subdomain Expressions

| | |
|---|---|
| Subdomain | 1-3, 5-7, 10-12, 14, 16-17 |
| k | (k0+k1*sqrt(sr_chns/gC))/(1+sqrt(sr_chns/gC)) |
| muP | mu37*exp(nu1*(37-T1)) |

### 6.2. Mesh

### 6.2.1. Mesh Statistics

| | |
|---|---|
| Number of degrees of freedom | 45190 |
| Number of mesh points | 2788 |
| Number of elements | 2797 |
| Triangular | 260 |

| | |
|---|---|
| Quadrilateral | 2537 |
| Number of boundary elements | 619 |
| Number of vertex elements | 30 |
| Minimum element quality | 0.017 |
| Element area ratio | 0.026 |

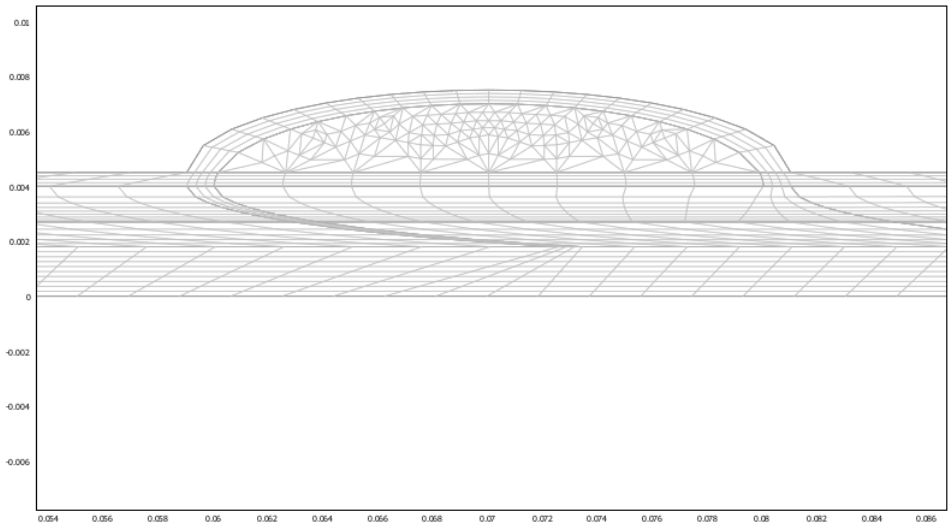


### 6.3. Application Mode: Non-Newtonian Flow (chns)

Application mode type: Non-Newtonian Flow (Chemical Engineering Module)

Application mode name: chns

#### 6.3.1. Application Mode Properties

| **Property** | **Value** |
|---|---|
| Default element type | Lagrange - $P_2$ $P_1$ |
| Analysis type | Transient |
| Stress tensor | Total |
| Corner smoothing | Off |
| Non-isothermal flow | Off |
| Turbulence model | None |
| Realizability | Off |
| Non-Newtonian flow | On |

| | |
|---|---|
| Brinkman on by default | Off |
| Two-phase flow | Single-phase flow |
| Frame | Frame (xy) |
| Weak constraints | Ideal |

### 6.3.2. Variables

Dependent variables: u, v, p, logk, logd, logw, phi, nxw, nyw

Shape functions: shlag(2,'lm1'), shlag(2,'lm2'), shlag(2,'u'), shlag(2,'v'), shlag(1,'p')

Interior boundaries not active

### 6.3.3. Boundary Settings

| Boundary | | 1, 3, 5 | 2, 13 |
|---|---|---|---|
| Type | | Velocity | Slip/Symmetry |
| X-velocity (u0) | m/s | **u_max*(s-0.5)*(s+0.5)** | 0 |
| Y-velocity (v0) | m/s | 0 | 0 |
| Pressure (p0) | Pa | 0 | 0 |

| Boundary | 8, 10, 21, 24-25, 35, 37-42, 44 | 29-31 |
|---|---|---|
| Type | Velocity | Normal flow, pressure |
| X-velocity (u0) | **u2t** | 0 |
| Y-velocity (v0) | **v2t** | 0 |
| Pressure (p0) | 0 | **1000** |

### 6.3.4. Subdomain Settings

| Subdomain | | 1-3, 5-7, 10-12, 14, 16-17 |
|---|---|---|
| Shape functions (shape) | | **shlag(2,'lm1') shlag(2,'lm2') shlag(2,'u') shlag(2,'v') shlag(1,'p')** |
| Integration order (gporder) | | **4 4 2** |
| Constraint order (cporder) | | **2 2 1** |
| Density (rho) | $kg/m^3$ | **1060** |
| Volume force, X-dir. (F_x) | $N/m^3$ | **-rho*g** |
| Zero shear rate viscosity (eta0) | $Pa \cdot s$ | **muP/(1-0.5*k*C)^2** |
| Model parameter (n) | 1 | **0.392** |
| Model parameter (lambda) | s | **0.11** |
| Infinite shear rate viscosity (eta_inf) | $Pa \cdot s$ | **0.0022** |
| Viscosity model type | | **user** |

| | | |
|---|---|---|
| (type_visc) | | |
| Isotropic diffusion switch (idon) | $m^2$ | **1** |

### 6.4. Application Mode: Plane Strain (pn)

Application mode type: Plane Strain

Application mode name: pn

#### 6.4.1. Application Mode Properties

| **Property** | **Value** |
|---|---|
| Default element type | Lagrange - Quadratic |
| Analysis type | Static |
| Specify eigenvalues using | Eigenfrequency |
| Frame | Frame (xy) |
| Weak constraints | Ideal |

#### 6.4.2. Variables

Dependent variables: u2, v2

Shape functions: shlag(2,'lm7'), shlag(2,'lm8'), shlag(2,'u2'), shlag(2,'v2')

Interior boundaries not active

#### 6.4.3. Point Settings

| | | |
|---|---|---|
| Point | | 1-30 |
| Shape functions (wcshape) | 1 | **[1;2]** |

#### 6.4.4. Boundary Settings

| | | | |
|---|---|---|---|
| Boundary | | 7, 32 | 8, 10, 21, 24-25, 35, 37-42, 44 |
| Edge load X-dir. (Fx) | 1 | 0 | **-lm1** |
| Edge load Y-dir. (Fy) | 1 | 0 | **-lm2** |
| Hx | 1 | **1** | 0 |
| Constraint Y-dir. (Ry) | m | 0 | 0 |
| Hy | 1 | **1** | 0 |

| | |
|---|---|
| Boundary | 9, 26, 36, 43 |
| Edge load X-dir. (Fx) | 0 |

| | |
|---|---|
| Edge load Y-dir. (Fy) | 0 |
| Hx | 0 |
| Constraint Y-dir. (Ry) | **(delta_max/h1^4)*sin(2*pi*t/3)*x*(x-h1)*(x-h1-0.09)*(x-h1-0.135)** |
| Hy | **1** |

### 6.4.5. Subdomain Settings

| Subdomain | | 4, 9, 15 | 8, 13 |
|---|---|---|---|
| Shape functions (shape) | | **shlag(2,'lm7') shlag(2,'lm8') shlag(2,'u2') shlag(2,'v2')** | **shlag(2,'lm7') shlag(2,'lm8') shlag(2,'u2') shlag(2,'v2')** |
| Integration order (gporder) | | **4 4** | **4 4** |
| Young's modulus (E) | Pa | **3.3e6** | **15e6** |
| Density (rho) | $kg/m^3$ | **960** | **500** |
| Poisson's ratio (nu) | 1 | **0.44** | **0.44** |
| Thickness (thickness) | m | **0.0005** | **0.0000025** |

## 6.5. Application Mode: Moving Mesh (ALE) (ale)

Application mode type: Moving Mesh (ALE)

Application mode name: ale

### 6.5.1. Application Mode Properties

| **Property** | **Value** |
|---|---|
| Default element type | Lagrange - Quadratic |
| Smoothing method | Laplace |
| Analysis type | Transient |
| Allow remeshing | Off |
| Defines frame | Frame (ale) |
| Original reference frame | Frame (ale) |
| Motion relative to | Frame (xy) |
| Weak constraints | Non-ideal |

### 6.5.2. Variables

Dependent variables:

Shape functions: shlag(2,'lm9'), shlag(2,'lm10'), shlag(2,'x'), shlag(2,'y')

Interior boundaries not active

### 6.5.3. Boundary Settings

| | | | |
|---|---|---|---|
| Boundary | | 1-3, 5, 13, 29-31 | 8, 10, 21, 24-25, 35, 37-42, 44 |
| Type | | Mesh displacement | Mesh displacement |
| Mesh displacement (deform) | m | {0;0} | **{u2;v2}** |
| defflag | m/s | **{1;1}** | **{1;1}** |

### 6.5.4. Subdomain Settings

| | | | |
|---|---|---|---|
| Subdomain | | 1-3, 5-7, 10-12, 14, 16-17 | 4, 8-9, 13, 15 |
| Shape functions (shape) | | **shlag(2,'lm9') shlag(2,'lm10') shlag(2,'x') shlag(2,'y')** | **shlag(2,'lm9') shlag(2,'lm10') shlag(2,'x') shlag(2,'y')** |
| Integration order (gporder) | | **4 4** | **4 4** |
| type | | free | **Phys** |
| Displacement variables (physexpr) | m | {0;0} | **{u2;v2}** |

| | | | |
|---|---|---|---|
| Subdomain initial value | | 1-3, 5-7, 10-12, 14, 16-17 | 4, 8-9, 13, 15 |
| Spatial coordinate (x) | m | xinit_ale | xinit_ale |
| Spatial coordinate (y) | m | yinit_ale | yinit_ale |

## 7. Extrusion Coupling Variables

### 7.1. Geom1

#### 7.1.1. Source Point: 19

| **Name** | **Value** |
|---|---|
| Expression | v2+Y |
| Transformation type | General |
| Source transformation | |
| Destination Subdomain | 1-17 (Geom1) |
| Name | Yp |

#### 7.1.2. Source Point: 19

| **Name** | **Value** |
|---|---|
| Expression | sqrt(v^2+u^2) |
| Transformation type | General |

| | |
|---|---|
| Source transformation | |
| Destination Subdomain | 1-17 (Geom1) |
| Name | Vp |

### 8. Solver Settings

Solve using a script: off

| | |
|---|---|
| Analysis type | Transient |
| Auto select solver | On |
| Solver | Time dependent |
| Solution form | Automatic |
| Symmetric | auto |
| Adaption | Off |

### 8.1. Direct (UMFPACK)

Solver type: Linear system solver

| **Parameter** | **Value** |
|---|---|
| Pivot threshold | 0.1 |
| Memory allocation factor | 0.7 |

### 8.2. Time Stepping

| **Parameter** | **Value** |
|---|---|
| Times | 0:0.01:10 |
| Relative tolerance | 0.01 |
| Absolute tolerance | 0.0010 |
| Times to store in output | Specified times |
| Time steps taken by solver | Free |
| Manual tuning of step size | Off |
| Initial time step | 0.0010 |
| Maximum time step | 1.0 |
| Maximum BDF order | 5 |
| Singular mass matrix | Maybe |
| Consistent initialization of DAE systems | Backward Euler |
| Error estimation strategy | Exclude algebraic |
| Allow complex numbers | Off |

### 8.3. Advanced

| Parameter | Value |
|---|---|
| Constraint handling method | Elimination |
| Null-space function | Automatic |
| Assembly block size | 5000 |
| Use Hermitian transpose of constraint matrix and in symmetry detection | Off |
| Use complex functions with real input | Off |
| Stop if error due to undefined operation | On |
| Type of scaling | Automatic |
| Manual scaling | |
| Row equilibration | On |
| Manual control of reassembly | Off |
| Load constant | On |
| Constraint constant | On |
| Mass constant | On |
| Damping (mass) constant | On |
| Jacobian constant | On |
| Constraint Jacobian constant | On |

## 9. Postprocessing

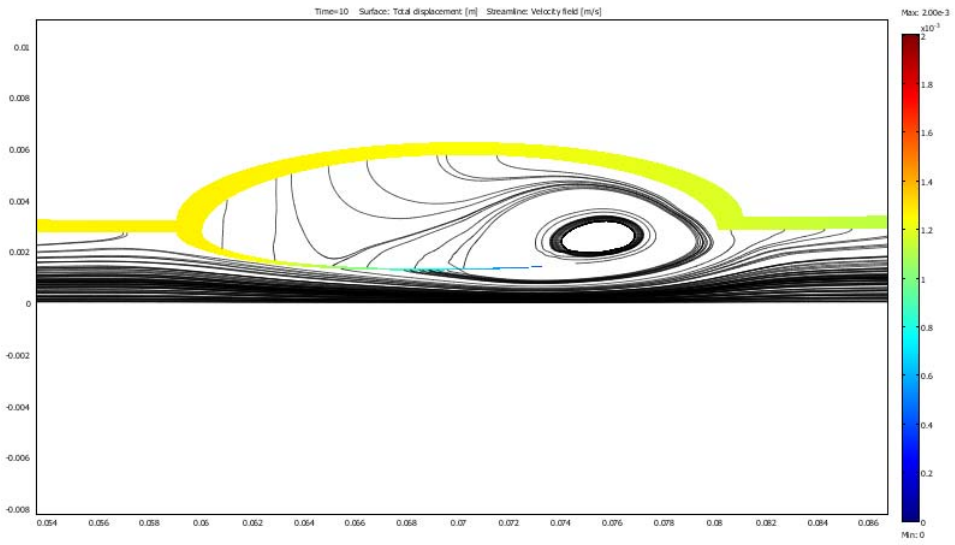

## 10. Variables

### 10.1. Point

#### 10.1.1. Point 1-3, 7-9, 24-28

| Name | Description | Expression |
|---|---|---|
| FXg_pn | Point load in global X-dir. | |
| FYg_pn | Point load in global Y-dir. | |
| disp_pn | Total displacement | |

#### 10.1.2. Point 4-6, 10-23, 29-30

| Name | Description | Expression |
|---|---|---|
| FXg_pn | Point load in global X-dir. | 0 |
| FYg_pn | Point load in global Y-dir. | 0 |
| disp_pn | Total displacement | sqrt(real(u2)^2+real(v2)^2) |

### 10.2. Boundary

#### 10.2.1. Boundary 1-6, 11-14, 17-18, 20, 22, 27-31, 33-34, 45-46

| Name | Description | Expression |
|---|---|---|
| K_X_chns | Viscous force per area, X component | 2 * nX_chns * eta_chns * uX+nY_chns * eta_chns * (uY+vX) |
| T_X_chns | Total force per area, X component | -nX_chns * p+2 * nX_chns * eta_chns * uX+nY_chns * eta_chns * (uY+vX) |
| K_Y_chns | Viscous force per area, Y component | nX_chns * eta_chns * (vX+uY)+2 * nY_chns * eta_chns * vY |
| T_Y_chns | Total force per area, Y component | -nY_chns * p+nX_chns * eta_chns * (vX+uY)+2 * nY_chns * eta_chns * vY |
| FXg_pn | Edge load in global X-dir. | |
| FYg_pn | Edge load in global Y-dir. | |
| disp_pn | Total displacement | |
| TaX_pn | Surface traction (force/area) in X-dir. | |
| TaY_pn | Surface traction (force/area) in Y-dir. | |

#### 10.2.2. Boundary 7, 9, 15-16, 19, 23, 26, 32, 36, 43

| Name | Description | Expression |
|---|---|---|
| K_X_chns | Viscous force per area, X component | |

| | | |
|---|---|---|
| T_X_chns | Total force per area, X component | |
| K_Y_chns | Viscous force per area, Y component | |
| T_Y_chns | Total force per area, Y component | |
| FXg_pn | Edge load in global X-dir. | 0 |
| FYg_pn | Edge load in global Y-dir. | 0 |
| disp_pn | Total displacement | sqrt(real(u2)^2+real(v2)^2) |
| TaX_pn | Surface traction (force/area) in X-dir. | sX_pn * nX_pn+sXY_pn * nY_pn |
| TaY_pn | Surface traction (force/area) in Y-dir. | sXY_pn * nX_pn+sY_pn * nY_pn |

#### 10.2.3. Boundary 8, 10, 21, 24-25, 35, 37-42, 44

| Name | Description | Expression |
|---|---|---|
| K_X_chns | Viscous force per area, X component | 2 * nX_chns * eta_chns * uX+nY_chns * eta_chns * (uY+vX) |
| T_X_chns | Total force per area, X component | -nX_chns * p+2 * nX_chns * eta_chns * uX+nY_chns * eta_chns * (uY+vX) |
| K_Y_chns | Viscous force per area, Y component | nX_chns * eta_chns * (vX+uY)+2 * nY_chns * eta_chns * vY |
| T_Y_chns | Total force per area, Y component | -nY_chns * p+nX_chns * eta_chns * (vX+uY)+2 * nY_chns * eta_chns * vY |
| FXg_pn | Edge load in global X-dir. | FX_pn * thickness_pn |
| FYg_pn | Edge load in global Y-dir. | FY_pn * thickness_pn |
| disp_pn | Total displacement | sqrt(real(u2)^2+real(v2)^2) |
| TaX_pn | Surface traction (force/area) in X-dir. | sX_pn * nX_pn+sXY_pn * nY_pn |
| TaY_pn | Surface traction (force/area) in Y-dir. | sXY_pn * nX_pn+sY_pn * nY_pn |

### 10.3. Subdomain

#### 10.3.1. Subdomain 1-3, 5-7, 10-12, 14, 16-17

| Name | Description | Expression |
|---|---|---|
| U_chns | Velocity field | sqrt(u^2+v^2) |
| V_chns | Vorticity | vX-uY |
| divU_chns | Divergence of velocity field | uX+vY |
| sr_chns | Shear rate | sqrt(0.5 * (4 * uX^2+2 * (uY+vX)^2+4 * vY^2)+eps) |
| cellRe_chns | Cell Reynolds | rho_chns * U_chns * h/eta_chns |

| | | |
|---|---|---|
| | number | |
| res_u_chns | Equation residual for u | rho_chns * (u * uX+v * uY)+pX-F_x_chns-eta_chns * (2 * uXX+uYY+vXY) |
| res_tst_u_chns | Variational equation residual for u | nojac(rho_chns) * (nojac(u) * uX+nojac(v) * uY)+pX-nojac(eta_chns) * (2 * uXX+uYY+vXY) |
| res_sc_u_chns | Shock capturing residual for u | rho_chns * (u * uX+v * uY)+pX-F_x_chns |
| res_v_chns | Equation residual for v | rho_chns * (u * vX+v * vY)+pY-F_y_chns-eta_chns * (vXX+uYX+2 * vYY) |
| res_tst_v_chns | Variational equation residual for v | nojac(rho_chns) * (nojac(u) * vX+nojac(v) * vY)+pY-nojac(eta_chns) * (vXX+uYX+2 * vYY) |
| res_sc_v_chns | Shock capturing residual for v | rho_chns * (u * vX+v * vY)+pY-F_y_chns |
| beta_X_chns | Convective field, X component | rho_chns * u |
| beta_Y_chns | Convective field, Y component | rho_chns * v |
| Dm_chns | Mean diffusion coefficient | eta_chns |
| da_chns | Total time scale factor | rho_chns |
| FXg_pn | Body load in global X-dir. | |
| FYg_pn | Body load in global Y-dir. | |
| disp_pn | Total displacement | |
| sX_pn | sX normal stress global sys. | |
| sY_pn | sY normal stress global sys. | |
| sZ_pn | sZ normal stress global sys. | |
| sXY_pn | sXY shear stress global sys. | |
| eX_pn | eX normal strain global sys. | |
| eY_pn | eY normal strain global sys. | |
| eXY_pn | eXY shear strain global sys. | |
| K_pn | Bulk modulus | |
| G_pn | Shear modulus | |

| | | |
|---|---|---|
| mises_pn | von Mises stress | |
| Ws_pn | Strain energy density | |
| evol_pn | Volumetric strain | |
| tresca_pn | Tresca stress | |
| xinit_ale | x coordinate initial value | X |
| yinit_ale | y coordinate initial value | Y |
| dx_ale | x-displacement | x-X |
| dy_ale | y-displacement | y-Y |

### 10.3.2. Subdomain 4, 8-9, 13, 15

| Name | Description | Expression |
|---|---|---|
| U_chns | Velocity field | |
| V_chns | Vorticity | |
| divU_chns | Divergence of velocity field | |
| sr_chns | Shear rate | |
| cellRe_chns | Cell Reynolds number | |
| res_u_chns | Equation residual for u | |
| res_tst_u_chns | Variational equation residual for u | |
| res_sc_u_chns | Shock capturing residual for u | |
| res_v_chns | Equation residual for v | |
| res_tst_v_chns | Variational equation residual for v | |
| res_sc_v_chns | Shock capturing residual for v | |
| beta_X_chns | Convective field, X component | |
| beta_Y_chns | Convective field, Y component | |
| Dm_chns | Mean diffusion coefficient | |
| da_chns | Total time scale | |

| | | |
|---|---|---|
| | factor | |
| FXg_pn | Body load in global X-dir. | 0 |
| FYg_pn | Body load in global Y-dir. | 0 |
| disp_pn | Total displacement | sqrt(real(u2)^2+real(v2)^2) |
| sX_pn | sX normal stress global sys. | E_pn * (1-nu_pn) * eX_pn/((1+nu_pn) * (1-2 * nu_pn))+E_pn * nu_pn * eY_pn/((1+nu_pn) * (1-2 * nu_pn)) |
| sY_pn | sY normal stress global sys. | E_pn * nu_pn * eX_pn/((1+nu_pn) * (1-2 * nu_pn))+E_pn * (1-nu_pn) * eY_pn/((1+nu_pn) * (1-2 * nu_pn)) |
| sZ_pn | sZ normal stress global sys. | E_pn * nu_pn * eX_pn/((1+nu_pn) * (1-2 * nu_pn))+E_pn * nu_pn * eY_pn/((1+nu_pn) * (1-2 * nu_pn)) |
| sXY_pn | sXY shear stress global sys. | E_pn * eXY_pn/(1+nu_pn) |
| eX_pn | eX normal strain global sys. | u2X |
| eY_pn | eY normal strain global sys. | v2Y |
| eXY_pn | eXY shear strain global sys. | 0.5 * (u2Y+v2X) |
| K_pn | Bulk modulus | E_pn/(3 * (1-2 * nu_pn)) |
| G_pn | Shear modulus | 0.5 * E_pn/(1+nu_pn) |
| mises_pn | von Mises stress | sqrt(sX_pn^2+sY_pn^2+sZ_pn^2-sX_pn * sY_pn-sY_pn * sZ_pn-sX_pn * sZ_pn+3 * sXY_pn^2) |
| Ws_pn | Strain energy density | 0.5 * thickness_pn * (eX_pn * sX_pn+eY_pn * sY_pn+2 * eXY_pn * sXY_pn) |
| evol_pn | Volumetric strain | eX_pn+eY_pn |
| tresca_pn | Tresca stress | max(max(abs(s1_pn-s2_pn),abs(s2_pn-s3_pn)),abs(s1_pn-s3_pn)) |
| xinit_ale | x coordinate initial value | X |
| yinit_ale | y coordinate initial value | Y |
| dx_ale | x-displacement | x-X |
| dy_ale | y-displacement | y-Y |

# APPENDIX E

# COMSOL MODEL - DOUBLE VALVE

## 1. Table of Contents



## 2. Model Properties

| Property | Value |
|---|---|
| Model name | Doublevalve |
| Author | Nilmini Wijeratne |
| Company | Texas Tech University |
| Department | Chemical Engineering |
| Reference | |
| URL | |
| Saved date | Jan 8, 2008 4:20:28 PM |
| Creation date | Dec 12, 2007 7:22:05 PM |
| COMSOL version | COMSOL 3.3.0.511 |

File name: C:\Users\nilmini\Research\Femlabfiles\double12-13s2.mph

Application modes and modules used in this model:

- Geom1 (2D)
  - Plane Strain (Structural Mechanics Module)
  - Non-Newtonian Flow (Chemical Engineering Module)
  - Moving Mesh (ALE)

## 3. Constants

| Name | Expression | Value | Description |
|---|---|---|---|
| rho | 1060 | | |
| h1 | 0.25 | | |
| g | 9.81 | | |
| u_amp | 0.75 | | |
| delta_max | 0.0045 | | |

| | | | |
|---|---|---|---|
| C | 0.3 | | |
| T1 | 28 | | |
| nu1 | 0.021 | | |
| mu37 | 1.4*10^(-3) | | |
| delta_max1 | 0.0027 | | |
| k02 | 6.117 | | |
| k12 | 2.0732 | | |
| gC2 | 1.0222 | | |

**4. Global Expressions**

| Name | Expression | Description | |
|---|---|---|---|
| u_max | u_amp*N1 | | |
| A | (abs(sin(2*pi*t/3))+sin(2*pi*t/3))/2 | | |
| k0 | exp(3.874-10.41*C+13.8*C^2-6.738*C^3) | | |
| k1 | exp(1.3435-2.803*C+2.711*C^2-0.6479*C^3) | | |
| gC | exp(-6.1508+27.923*C-25.6*C^2+3.697*C^3) | | |
| B | (-abs(sin(2*pi*t/3))+sin(2*pi*t/3))/2 | | |
| N1 | (abs(sin(2*pi*t/3)+sin(2*pi*t/1.5)) + (sin(2*pi*t/3)+sin(2*pi*t/1.5))) /2 | | |
| N2 | (-abs(sin(2*pi*t/3)+sin(2*pi*t/1.5)) + (sin(2*pi*t/3)+sin(2*pi*t/1.5))) /2 | | |
| B1 | (-abs(sin(2*pi*t/3+pi/2))+sin(2*pi*t/3+pi/2))/2 | | |

## 5. Geometry

Number of geometries: 1

### 5.1. Geom1

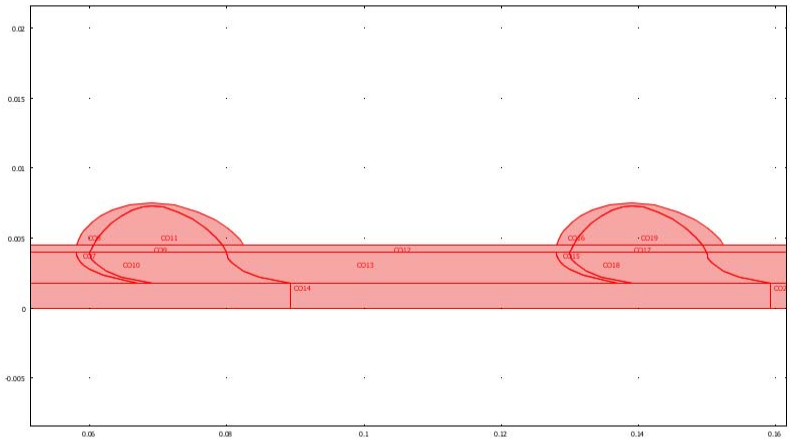

#### 5.1.1. Point mode

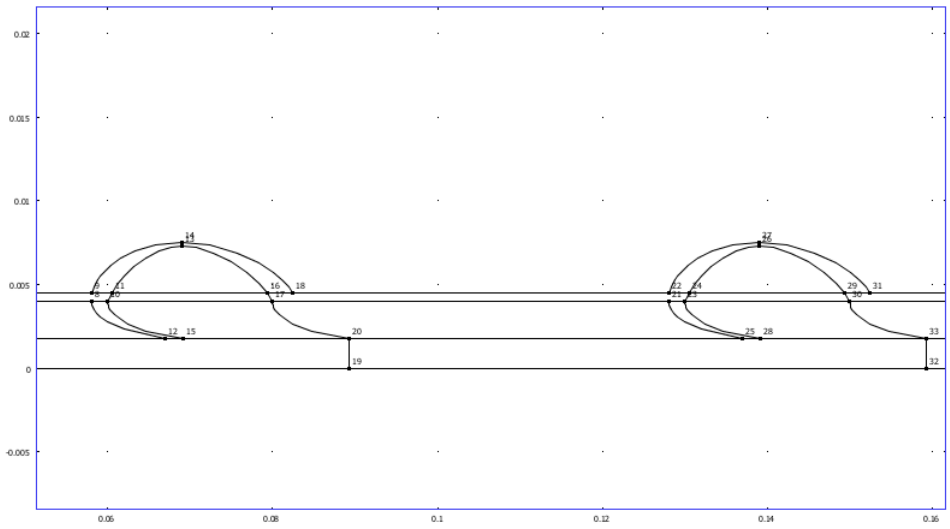

### 5.1.2. Boundary mode

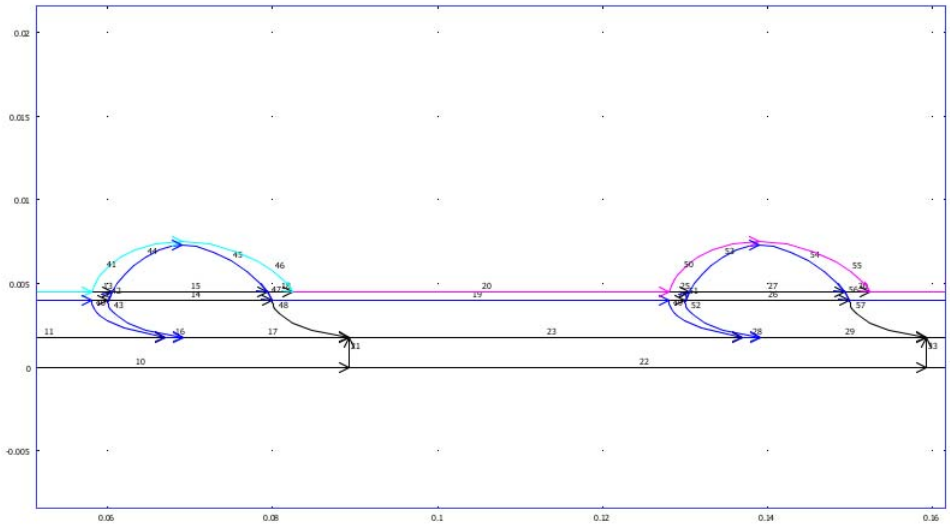

### 5.1.3. Subdomain mode

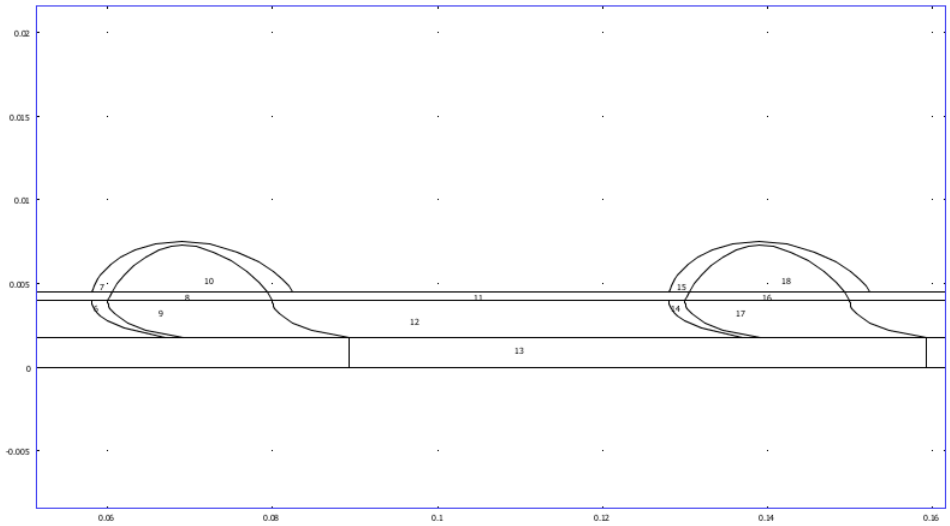


## 6. Geom1

Space dimensions: 2D

Independent variables: X, Y, Z

### 6.1. Expressions

#### 6.1.1. Subdomain Expressions

| | |
|---|---|
| Subdomain | 1-2, 4-5, 8-10, 12-13, 16-18, 20-21 |
| k | (k0+k1*sqrt(sr_chns/gC))/(1+sqrt(sr_chns/gC)) |
| muP | mu37*exp(nu1*(37-T1)) |

### 6.2. Mesh

#### 6.2.1. Mesh Statistics

| | |
|---|---|
| Number of degrees of freedom | 61088 |
| Number of mesh points | 3758 |
| Number of elements | 4171 |
| Triangular | 1108 |
| Quadrilateral | 3063 |
| Number of boundary elements | 716 |

| | |
|---|---|
| Number of vertex elements | 37 |
| Minimum element quality | 0.025 |
| Element area ratio | 0.008 |

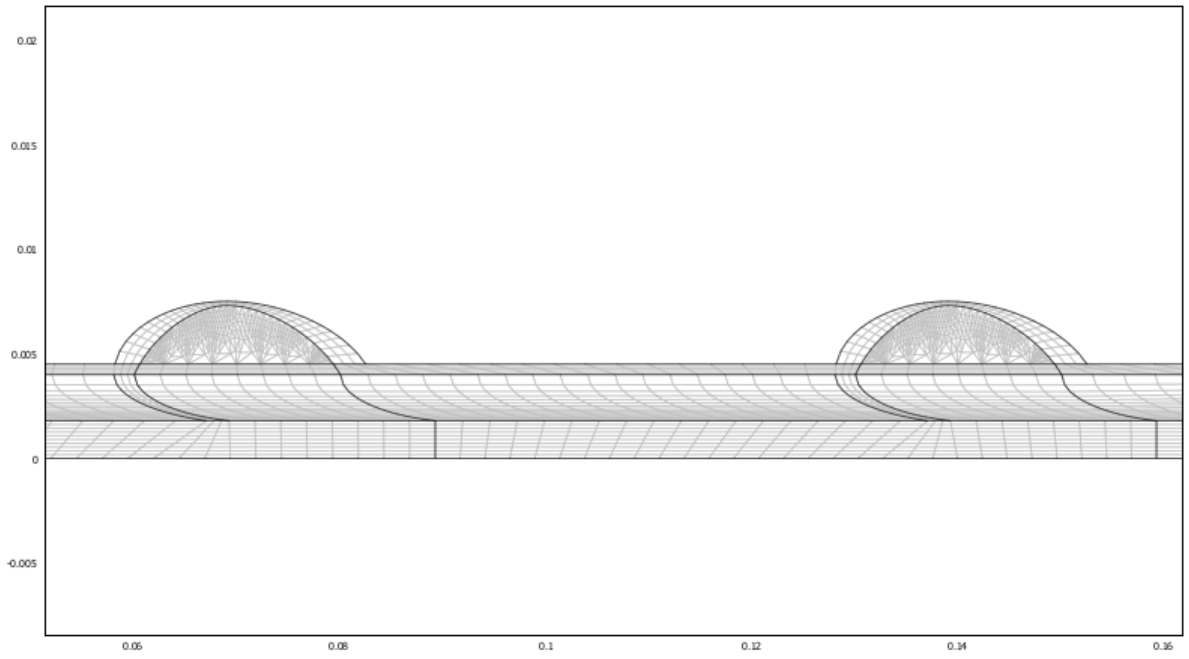


### 6.3. Application Mode: Plane Strain (smpn)

Application mode type: Plane Strain (Structural Mechanics Module)

Application mode name: smpn

#### 6.3.1. Scalar Variables

| Name | Variable | Value | Description |
|---|---|---|---|
| t_old_ini | t_old_ini_smpn | -1 | Initial condition previous time step (contact with dynamic friction) |

#### 6.3.2. Application Mode Properties

| **Property** | **Value** |
|---|---|
| Default element type | Lagrange - Quadratic |

| | |
|---|---|
| Analysis type | Static |
| Large deformation | Off |
| Implementation | Principle of virtual work |
| Specify eigenvalues using | Eigenfrequency |
| Create frame | Off |
| Deform frame | Frame (ref) |
| Frame | Frame (ref) |
| Weak constraints | Ideal |

### 6.3.3. Variables

Dependent variables: u2, v2, p2

Shape functions: shlag(2,'lm7'), shlag(2,'lm8'), shlag(2,'u2'), shlag(2,'v2')

Interior boundaries not active

### 6.3.4. Point Settings

| | | |
|---|---|---|
| Point | | 1-37 |
| Shape functions (wcshape) | 1 | **[1;2]** |

### 6.3.5. Boundary Settings

| | | | |
|---|---|---|---|
| Boundary | | 5, 38 | 6, 8, 16, 19, 28, 31, 40, 42-45, 47, 49, 51-54, 56 |
| Edge load X-dir. (Fx) | 1 | 0 | **-lm1** |
| Edge load Y-dir. (Fy) | 1 | 0 | **-lm2** |
| constrcond | 1 | **fixed** | Free |
| Hx | 1 | 0 | 0 |
| Constraint Y-dir. (Ry) | m | 0 | 0 |
| Hy | 1 | 0 | 0 |

| | | |
|---|---|---|
| Boundary | 7, 41, 46 | 20, 32, 50, 55 |
| Edge load X-dir. (Fx) | 0 | 0 |
| Edge load Y-dir. (Fy) | 0 | 0 |
| constrcond | **displacement** | **displacement** |
| Hx | **1** | **1** |
| Constraint Y-dir. (Ry) | **(delta_max/h1^5)*(B1)*(x*(x-h1)*(x-h1-0.0635)*(x-0.125-h1)*(x-h1-0.1875))** | **(delta_max1/h1^5)*(N2)*(x*(x-h1)*(x-h1-0.0635)*(x-0.125-h1)*(x-h1-0.1875))** |
| Hy | **1** | **1** |

### 6.3.6. Subdomain Settings

| Subdomain | | 3, 11, 15, 19 | 6 |
|---|---|---|---|
| Shape functions (shape) | | **shlag(2,'lm7') shlag(2,'lm8') shlag(2,'u2') shlag(2,'v2')** | **shlag(2,'lm7') shlag(2,'lm8') shlag(2,'u2') shlag(2,'v2')** |
| Integration order (gporder) | | **4 4 4** | **4 4 4** |
| Young's modulus (E) | Pa | **3.3e6** | **15e6** |
| Density (rho) | $kg/m^3$ | **500** | **960** |
| Poisson's ratio (nu) | 1 | **0.44** | **0.44** |
| Thickness (thickness) | m | **0.0005** | **0.0000025** |
| User-defined PML coordinates (userPML) | m | **{x;y}** | **{x;y}** |

| Subdomain | 7 | 14 |
|---|---|---|
| Shape functions (shape) | **shlag(2,'lm7') shlag(2,'lm8') shlag(2,'u2') shlag(2,'v2')** | **shlag(2,'lm7') shlag(2,'lm8') shlag(2,'u2') shlag(2,'v2')** |
| Integration order (gporder) | **4 4 4** | **4 4 4** |
| Young's modulus (E) | **2.3e6** | **20e6** |
| Density (rho) | **500** | **960** |
| Poisson's ratio (nu) | **0.44** | **0.44** |
| Thickness (thickness) | **0.0005** | **0.0000025** |
| User-defined PML coordinates (userPML) | **{x;y}** | **{x;y}** |

## 6.4. Application Mode: Non-Newtonian Flow (chns)

Application mode type: Non-Newtonian Flow (Chemical Engineering Module)

Application mode name: chns

### 6.4.1. Application Mode Properties

| **Property** | **Value** |
|---|---|
| Default element type | Lagrange - $P_2$ $P_1$ |
| Analysis type | Transient |
| Stress tensor | Total |
| Corner smoothing | Off |
| Non-isothermal flow | Off |
| Turbulence model | None |

| | |
|---|---|
| Realizability | Off |
| Non-Newtonian flow | On |
| Brinkman on by default | Off |
| Two-phase flow | Single-phase flow |
| Frame | Frame (ref) |
| Weak constraints | Ideal |

### 6.4.2. Variables

Dependent variables: u, v, p, logk, logd, logw, phi, nxw, nyw

Shape functions: shlag(2,'lm1'), shlag(2,'lm2'), shlag(2,'u'), shlag(2,'v'), shlag(1,'p')

Interior boundaries not active

### 6.4.3. Boundary Settings

| Boundary | | 1, 3 | 2, 10, 22, 34 |
|---|---|---|---|
| Type | | Velocity | Slip/Symmetry |
| X-velocity (u0) | m/s | **u_max*(s-0.5)*(s+0.5)** | 0 |
| Y-velocity (v0) | m/s | 0 | 0 |
| Pressure (p0) | Pa | 0 | 0 |

| Boundary | 6, 8, 16, 19, 28, 31, 40, 42-45, 47, 49, 51-54, 56 | 36-37 |
|---|---|---|
| Type | Velocity | Pressure |
| X-velocity (u0) | **u2t** | 0 |
| Y-velocity (v0) | **v2t** | 0 |
| Pressure (p0) | 0 | **1000** |

### 6.4.4. Subdomain Settings

| Subdomain | | 1-2, 4-5, 8-10, 12-13, 16-18, 20-21 |
|---|---|---|
| Shape functions (shape) | | **shlag(2,'lm1') shlag(2,'lm2') shlag(2,'u') shlag(2,'v') shlag(1,'p')** |
| Integration order (gporder) | | **4 4 2** |
| Constraint order (cporder) | | **2 2 1** |
| Density (rho) | $kg/m^3$ | **1060** |
| Volume force, X-dir. (F_x) | $N/m^3$ | **-rho*g** |
| Zero shear rate viscosity (eta0) | $Pa \cdot s$ | **muP/(1-0.5*k*C)^2** |
| Viscosity model type (type_visc) | $Pa \cdot s$ | **user** |
| Isotropic diffusion switch | $m^2$ | **1** |

| | | |
|---|---|---|
| (idon) | | |

### 6.5. Application Mode: Moving Mesh (ALE) (ale)

Application mode type: Moving Mesh (ALE)

Application mode name: ale

#### 6.5.1. Application Mode Properties

| Property | Value |
|---|---|
| Default element type | Lagrange - Quadratic |
| Smoothing method | Laplace |
| Analysis type | Transient |
| Allow remeshing | Off |
| Defines frame | Frame (ale) |
| Original reference frame | Frame (ale) |
| Motion relative to | Frame (ref) |
| Weak constraints | Non-ideal |

#### 6.5.2. Variables

Dependent variables:

Shape functions: shlag(2,'lm9'), shlag(2,'lm10'), shlag(2,'x'), shlag(2,'y')

Interior boundaries not active

#### 6.5.3. Boundary Settings

| | | | |
|---|---|---|---|
| Boundary | | 1-3, 10, 22, 34, 36-37 | 6, 8, 16, 19, 28, 31, 40, 42-45, 47, 49, 51-54, 56 |
| Type | | Mesh displacement | Mesh displacement |
| Mesh displacement (deform) | m | {0;0} | **{u2;v2}** |
| defflag | m/s | **{1;1}** | **{1;1}** |

#### 6.5.4. Subdomain Settings

| | | | |
|---|---|---|---|
| Subdomain | | 1-2, 4-5, 8-10, 12-13, 16-18, 20-21 | 3, 6-7, 11, 14-15, 19 |
| Shape functions (shape) | | **shlag(2,'lm9') shlag(2,'lm10') shlag(2,'x') shlag(2,'y')** | **shlag(2,'lm9') shlag(2,'lm10') shlag(2,'x') shlag(2,'y')** |

| | | | |
|---|---|---|---|
| Integration order (gporder) | | **4 4** | **4 4** |
| type | | free | **Phys** |
| Displacement variables (physexpr) | m | {0;0} | **{u2;v2}** |

| | | | |
|---|---|---|---|
| Subdomain initial value | | 1-2, 4-5, 8-10, 12-13, 16-18, 20-21 | 3, 6-7, 11, 14-15, 19 |
| Spatial coordinate (x) | m | xinit_ale | xinit_ale |
| Spatial coordinate (y) | m | yinit_ale | yinit_ale |

### 7. Solver Settings

Solve using a script: off

| | |
|---|---|
| Analysis type | Transient |
| Auto select solver | On |
| Solver | Time dependent |
| Solution form | Automatic |
| Symmetric | auto |
| Adaption | Off |

### 7.1. Direct (UMFPACK)

Solver type: Linear system solver

| **Parameter** | **Value** |
|---|---|
| Pivot threshold | 0.1 |
| Memory allocation factor | 0.7 |

### 7.2. Time Stepping

| **Parameter** | **Value** |
|---|---|
| Times | 0:0.1:10 |
| Relative tolerance | 0.01 |
| Absolute tolerance | 0.0010 |
| Times to store in output | Specified times |
| Time steps taken by solver | Free |
| Manual tuning of step size | Off |
| Initial time step | 0.0010 |
| Maximum time step | 1.0 |
| Maximum BDF order | 5 |
| Singular mass matrix | Maybe |
| Consistent initialization of DAE systems | Backward Euler |

| | |
|---|---|
| Error estimation strategy | Exclude algebraic |
| Allow complex numbers | Off |

### 7.3. Advanced

| **Parameter** | **Value** |
|---|---|
| Constraint handling method | Elimination |
| Null-space function | Automatic |
| Assembly block size | 5000 |
| Use Hermitian transpose of constraint matrix and in symmetry detection | Off |
| Use complex functions with real input | Off |
| Stop if error due to undefined operation | On |
| Type of scaling | Automatic |
| Manual scaling | |
| Row equilibration | On |
| Manual control of reassembly | Off |
| Load constant | On |
| Constraint constant | On |
| Mass constant | On |
| Damping (mass) constant | On |
| Jacobian constant | On |
| Constraint Jacobian constant | On |

## 8. Postprocessing

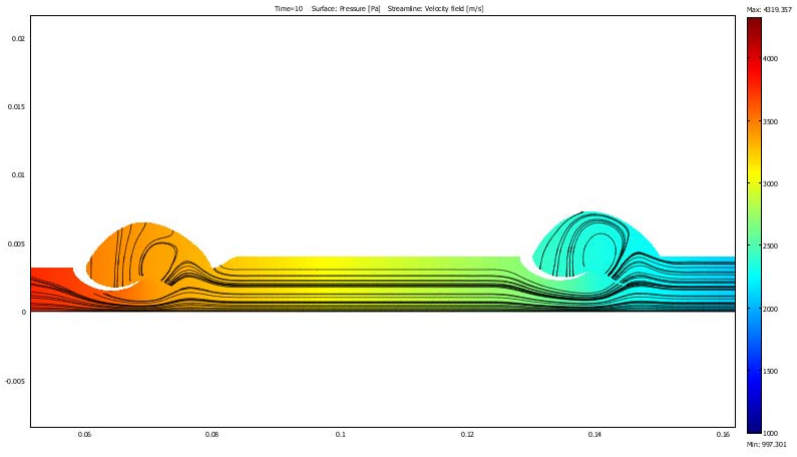


## 9. Variables

### 9.1. Point

#### 9.1.1. Point 1-2, 6-7, 19-20, 32-35

| Name | Description | Expression |
|---|---|---|
| FXg_smpn | Point load in global X-dir. | |
| FYg_smpn | Point load in global Y-dir. | |
| disp_smpn | Total displacement | |

#### 9.1.2. Point 3-5, 8-18, 21-31, 36-37

| Name | Description | Expression |
|---|---|---|
| FXg_smpn | Point load in global X-dir. | 0 |
| FYg_smpn | Point load in global Y-dir. | 0 |
| disp_smpn | Total displacement | sqrt(real(u2)^2+real(v2)^2) |

### 9.2. Boundary

#### 9.2.1. Boundary 1-4, 9-11, 14-15, 17, 21-23, 26-27, 29, 33-37, 39, 48, 57

| Name | Description | Expression |
|---|---|---|
| FXg_smpn | Edge load in global X-dir. | |
| FYg_smpn | Edge load in global Y-dir. | |
| disp_smpn | Total displacement | |
| TaX_smpn | Surface traction (force/area) in X-dir. | |
| TaY_smpn | Surface traction (force/area) in Y-dir. | |
| K_X_chns | Viscous force per area, X component | 2 * nX_chns * eta_chns * uX+nY_chns * eta_chns * (uY+vX) |
| T_X_chns | Total force per area, X component | -nX_chns * p+2 * nX_chns * eta_chns * uX+nY_chns * eta_chns * (uY+vX) |
| K_Y_chns | Viscous force per area, Y component | nX_chns * eta_chns * (vX+uY)+2 * nY_chns * eta_chns * vY |
| T_Y_chns | Total force per area, Y component | -nY_chns * p+nX_chns * eta_chns * (vX+uY)+2 * nY_chns * eta_chns * vY |

#### 9.2.2. Boundary 5, 7, 12-13, 18, 20, 24-25, 30, 32, 38, 41, 46, 50, 55

| Name | Description | Expression |
|---|---|---|
| FXg_smpn | Edge load in global X-dir. | 0 |
| FYg_smpn | Edge load in global Y-dir. | 0 |
| disp_smpn | Total displacement | sqrt(real(u2)^2+real(v2)^2) |

| | | |
|---|---|---|
| TaX_smpn | Surface traction (force/area) in X-dir. | sX_smpn * nX_smpn+sXY_smpn * nY_smpn |
| TaY_smpn | Surface traction (force/area) in Y-dir. | sXY_smpn * nX_smpn+sY_smpn * nY_smpn |
| K_X_chns | Viscous force per area, X component | |
| T_X_chns | Total force per area, X component | |
| K_Y_chns | Viscous force per area, Y component | |
| T_Y_chns | Total force per area, Y component | |

#### 9.2.3. Boundary 6, 8, 16, 19, 28, 31, 40, 42-45, 47, 49, 51-54, 56

| Name | Description | Expression |
|---|---|---|
| FXg_smpn | Edge load in global X-dir. | FX_smpn * thickness_smpn |
| FYg_smpn | Edge load in global Y-dir. | FY_smpn * thickness_smpn |
| disp_smpn | Total displacement | sqrt(real(u2)^2+real(v2)^2) |
| TaX_smpn | Surface traction (force/area) in X-dir. | sX_smpn * nX_smpn+sXY_smpn * nY_smpn |
| TaY_smpn | Surface traction (force/area) in Y-dir. | sXY_smpn * nX_smpn+sY_smpn * nY_smpn |
| K_X_chns | Viscous force per area, X component | 2 * nX_chns * eta_chns * uX+nY_chns * eta_chns * (uY+vX) |
| T_X_chns | Total force per area, X component | -nX_chns * p+2 * nX_chns * eta_chns * uX+nY_chns * eta_chns * (uY+vX) |
| K_Y_chns | Viscous force per area, Y component | nX_chns * eta_chns * (vX+uY)+2 * nY_chns * eta_chns * vY |
| T_Y_chns | Total force per area, Y component | -nY_chns * p+nX_chns * eta_chns * (vX+uY)+2 * nY_chns * eta_chns * vY |

### 9.3. Subdomain

#### 9.3.1. Subdomain 1-2, 4-5, 8-10, 12-13, 16-18, 20-21

| Name | Description | Expression |
|---|---|---|
| FXg_smpn | Body load in global X-dir. | |
| FYg_smpn | Body load in global Y-dir. | |

| | | |
|---|---|---|
| disp_smpn | Total displacement | |
| sX_smpn | sX normal stress global sys. | |
| sY_smpn | sY normal stress global sys. | |
| sZ_smpn | sZ normal stress global sys. | |
| sXY_smpn | sXY shear stress global sys. | |
| eX_smpn | eX normal strain global sys. | |
| eY_smpn | eY normal strain global sys. | |
| eXY_smpn | eXY shear strain global sys. | |
| K_smpn | Bulk modulus | |
| G_smpn | Shear modulus | |
| mises_smpn | von Mises stress | |
| Ws_smpn | Strain energy density | |
| evol_smpn | Volumetric strain | |
| tresca_smpn | Tresca stress | |
| U_chns | Velocity field | sqrt(u^2+v^2) |
| V_chns | Vorticity | vX-uY |
| divU_chns | Divergence of velocity field | uX+vY |
| sr_chns | Shear rate | sqrt(0.5 * (4 * uX^2+2 * (uY+vX)^2+4 * vY^2)+eps) |
| cellRe_chns | Cell Reynolds number | rho_chns * U_chns * h/eta_chns |
| res_u_chns | Equation residual for u | rho_chns * (u * uX+v * uY)+pX-F_x_chns-eta_chns * (2 * uXX+uYY+vXY) |
| res_tst_u_chns | Variational equation residual for u | nojac(rho_chns) * (nojac(u) * uX+nojac(v) * uY)+pX-nojac(eta_chns) * (2 * uXX+uYY+vXY) |
| res_sc_u_chns | Shock capturing residual for u | rho_chns * (u * uX+v * uY)+pX-F_x_chns |
| res_v_chns | Equation residual for v | rho_chns * (u * vX+v * vY)+pY-F_y_chns-eta_chns * (vXX+uYX+2 * vYY) |
| res_tst_v_chns | Variational equation residual for v | nojac(rho_chns) * (nojac(u) * vX+nojac(v) * vY)+pY-nojac(eta_chns) * (vXX+uYX+2 * vYY) |
| res_sc_v_chns | Shock capturing residual for v | rho_chns * (u * vX+v * vY)+pY-F_y_chns |
| beta_X_chns | Convective field, X | rho_chns * u |

| | | |
|---|---|---|
| | component | |
| beta_Y_chns | Convective field, Y component | rho_chns * v |
| Dm_chns | Mean diffusion coefficient | eta_chns |
| da_chns | Total time scale factor | rho_chns |
| xinit_ale | x coordinate initial value | X |
| yinit_ale | y coordinate initial value | Y |
| dx_ale | x-displacement | x-X |
| dy_ale | y-displacement | y-Y |

### 9.3.2. Subdomain 3, 6-7, 11, 14-15, 19

| **Name** | **Description** | **Expression** |
|---|---|---|
| FXg_smpn | Body load in global X-dir. | 0 |
| FYg_smpn | Body load in global Y-dir. | 0 |
| disp_smpn | Total displacement | sqrt(real(u2)^2+real(v2)^2) |
| sX_smpn | sX normal stress global sys. | E_smpn * (1-nu_smpn) * eX_smpn/((1+nu_smpn) * (1-2 * nu_smpn))+E_smpn * nu_smpn * eY_smpn/((1+nu_smpn) * (1-2 * nu_smpn)) |
| sY_smpn | sY normal stress global sys. | E_smpn * nu_smpn * eX_smpn/((1+nu_smpn) * (1-2 * nu_smpn))+E_smpn * (1-nu_smpn) * eY_smpn/((1+nu_smpn) * (1-2 * nu_smpn)) |
| sZ_smpn | sZ normal stress global sys. | E_smpn * nu_smpn * eX_smpn/((1+nu_smpn) * (1-2 * nu_smpn))+E_smpn * nu_smpn * eY_smpn/((1+nu_smpn) * (1-2 * nu_smpn)) |
| sXY_smpn | sXY shear stress global sys. | E_smpn * eXY_smpn/(1+nu_smpn) |
| eX_smpn | eX normal strain global sys. | u2X |
| eY_smpn | eY normal strain global sys. | v2Y |
| eXY_smpn | eXY shear strain global | 0.5 * (u2Y+v2X) |

| | | |
|---|---|---|
| | sys. | |
| K_smpn | Bulk modulus | E_smpn/(3 * (1-2 * nu_smpn)) |
| G_smpn | Shear modulus | 0.5 * E_smpn/(1+nu_smpn) |
| mises_smpn | von Mises stress | sqrt(sX_smpn^2+sY_smpn^2+sZ_smpn^2-sX_smpn * sY_smpn-sY_smpn * sZ_smpn-sX_smpn * sZ_smpn+3 * sXY_smpn^2) |
| Ws_smpn | Strain energy density | 0.5 * thickness_smpn * (eX_smpn * sX_smpn+eY_smpn * sY_smpn+2 * eXY_smpn * sXY_smpn) |
| evol_smpn | Volumetric strain | eX_smpn+eY_smpn |
| tresca_smpn | Tresca stress | max(max(abs(s1_smpn-s2_smpn),abs(s2_smpn-s3_smpn)),abs(s1_smpn-s3_smpn)) |
| U_chns | Velocity field | |
| V_chns | Vorticity | |
| divU_chns | Divergence of velocity field | |
| sr_chns | Shear rate | |
| cellRe_chns | Cell Reynolds number | |
| res_u_chns | Equation residual for u | |
| res_tst_u_chns | Variational equation residual for u | |
| res_sc_u_chns | Shock capturing residual for u | |
| res_v_chns | Equation residual for v | |
| res_tst_v_chns | Variational equation residual for v | |
| res_sc_v_chns | Shock capturing residual for v | |
| beta_X_chns | Convective field, X component | |
| beta_Y_chns | Convective field, Y component | |
| Dm_chns | Mean diffusion | |

| | | |
|---|---|---|
| | coefficient | |
| da_chns | Total time scale factor | |
| xinit_ale | x coordinate initial value | X |
| yinit_ale | y coordinate initial value | Y |
| dx_ale | x-displacement | x-X |
| dy_ale | y-displacement | y-Y |

# APPENDIX F

## ESTIMATING THE DIMENSIONS OF THE VEIN AND VALVE

```
%
clear all clc close all

x=imread('vein1','JPG'); I=x(:,:,1); figure(1), imshow(I)
title('Original image')

% Histogram

h=imhist(I); figure(2),plot(h) ylim('auto')

% filtering

I1=fspecial('unsharp',0.7);
I2=imfilter(I,I1,'conv','replicate','same'); figure(3),imshow(I2)

I3=im2bw(I,[70/255]); figure(4),imshow(I3)



RBH=bwareaopen(I3,12000,4); figure(5), imshow(RBH)

 BH=imfill(RBH,'holes');
 figure(6), imshow(BH)
```

```
  se = strel('disk',1);
  cBH = imclose(BH,se);
  figure(7), imshow(cBH)

I4=double(RBH);

 I5=edge(I4,'canny');
 figure(8), imshow(I5)
```

# BIBLIOGRAPHY

[1] F. E. Hossler and R. F. West. Venous valve anatomy and morphometry: Studies on the duckling using vascular corrosion casting. *The American Journal of Anatomy*, (181):425–432, 1988.

[2] J. Donea, A. Huerta, J.-Ph. Ponthot, and A. Rodriguez-Ferran. *Arbitrary Lagrangian-Eulerian Methods*, volume 1 of *Encyclopedia of computational Mechanics*, chapter 14, pages 1–25. John Wiley & Sons Ltd., 2004.

[3] Programmable flexible-tube flow regulator and use methods. http://ferepatentsonline.com/EP1383570.html.

[4] Y.C. Fung. *Biomechanics:Circulations*. Springer-Verlag, New York, NY, 2 edition, 1996.

[5] J.B. Grotberg and O.E. Jensen. Bio fluidic mechanics in flexible tube. *Annual Review of Fluid mechanics*, 36:121–147, 2004.

[6] X.Y Luo and T.J. Pedley. A numerical simulation of steady flow in 2-d collapsible channel. *J. Fluids and Structures*, 9:149–174, 1995.

[7] A.H. Shapiro. Steady flow in collapsible tube. *J. Biomechanical Engineering*, pages 126–147, 1977.

[8] K.P. Selverov and H.A. Stone. Peristaltically driven channel flows with applications toward micro- mixing. *Physics of Fluids*, 13:1837–1859, 2000.

[9] M. Yi, H. Bau, and H. Hu. Peristaltically induced motion in a closed cavity with two vibrating walls. *Physics of Fluids*, 14(1):184–197, 2002.

[10] E. H. Ibrahim, M. Iregui, D. Prentice, G. Sherman, M. H. Kollef, and W. Shannon. Deep vein thrombosis during prolonged mechanical ventilation despite prophylaxis. *Critical Care Medicine*, 30(4):771–774, 2002.

[11] I. Norkiene, D. Ringaitiene, K. Rucinskas, R. Samalavicius, A. Baublys, S. Miniauskas, and V. Sirvydis. Intra-aortic balloon counterpulsation in decompensated cardiomyopathy patients: bridge to transplantation or assist device. *CardioVasc Thorac Surg*, 6:66–70, 2007.

[12] J. Badilla, C. Haw, and J. Rootman. Superior ophthalmic vein cannulation through a lateral orbitotomy for embolization of a cavernous dural fistula. *Arch Ophthalmol*, 125(12):1700–1702, 2007.

[13] G. Bohle III, J. Rieger, J. Huryn, D. Verbel, F. Hwang, and I Zlotolow. Efficacy of speech aid prostheses for acquired defects of the soft palate and velopharyngeal inadequacy - clinical assessments and cephalometric analysis: A memorial sloan-kettering study. *Head and Neck*, 27(3):195–207, 2005.

[14] R. D. Kamm and A. H. Shapiro. Unsteady flow in collapsible tubes subjected to external pressure or body forces. *J. Fluid Mechanics*, 95:1–78, 1979.

[15] D.J. Griffiths. Urethral elasticity and micturition hydrodynamics in females. *Med. & Biol. Eng.*, 7:201–215, 1969.

[16] D. J. Griffiths. Hydrodynamics of male micturition - i: Theory of steady flow through elastic tube walls. *Med. & Biol. Eng.*, 9:581–588, 1971.

[17] D. M. Gleason, M. R. Bottaccini, and J.C. Byrne. Review of current physical and hydrodynamic concepts and their impact on urodynamics. *Neurourology and Urodynamics*, 6(1):1–9, 2005.

[18] H. Hsiung, C. Lee, J. Lin, and G. Lee. Active micro-mixers utilizing moving wall structures activated pneumatically by buried side chambers. *J. Micromech. Microeng.*, 17(1):129–138, January 2007.

[19] J.K Franklin. A monograph on veins. *J. of Anatomy*, 73(1):64–75, 1938.

[20] Flexible valve for administering constant flow rates of medicine from a nebulizer. http://www.freepatentsonline.com/5655520.html.

[21] R.B. Bird, W.E. Stewart, and E.N. Lightfoot. *Transport Phenomena*. John Wiley & Sons,Inc., 2 edition, 2002.

[22] Q.S. Nguyen. *Stability and Nonlinear Solid Mechanics*. John Wiley & Sons, New York, NY, 2000.

[23] I. Kececioglu, M.E. McClurken, D. Kamm, and A. H. Shapiro. Steady supercritical flow in collapsible tunes. part 1. experimental observations. *J. Fluid Mechanics*, 109:367–389, 1981.

[24] I. Kececioglu, M.E. McClurken, D. Kamm, and A. H. Shapiro. Steady supercritical flow in collapsible tunes. part 2. theoretical studies. *J. Fluid Mechanics*, 109:391–415, 1981.

[25] W.A. Conard, M.L. Cohen, and D.M. Mcqueen. Note on the oscillations of collapsible tubes. *Med. Biol. Engng. & Comput.*, 16:211–214, 1978.

[26] T.J. Pedley. *The Fluid Mechanics of Large Vessels*. Cambridge,U.K, 1980.

[27] C.D. Bertram and T. J. Pedley. A mathematical model of unsteady collapsible tube behavior. *J. Fluid Mech.*, 130:315–345, 1982.

[28] M. Heil and O.E. Jensen. *Flow in Deformable tubes and channels.Flow in collapsible tubes and past other highly compliant boundaries*, chapter Flows in Deformable tubes and channels. Kluwer, New York,NY, 2000.

[29] R.W. Brower and C. Scholten. Experimental evidence on the mechanism for the instability of flow in collapsible vessels. *Med. & Biol. Engng.*, 13:839–845, 1975.

[30] D. J. Griffiths. Oscillations in the outflow from a collapsible tube. *Med. & Biol. Eng.*, 15:357–362, 1977.

[31] C. Cancelli and T.J. Pedley. A separated-flow model for collapsible tube oscillations. *J. Fluid Mechanics*, 157:375–404, 1985.

[32] T. Ikeda and Y. Matsuzaki. Separable and re-attachable flow model for collapsible tube-flow analysis. *J. Biomechanical Engineering*, 121:153–159, 1999.

[33] Y. Matsuzaki, T. Ikeda, T. Matsumoto, and T. Kitagawa. Experiments on steady and oscillatory flows at moderate reynolds numbers in a quasi-two dimensional channel with a throat. *J. Biomechanical Engineering*, 120:594–601, October 1998.

[34] N. S. Wijeratne and K.A. Hoo. An analytical approach to identify fluid flow separation and re-attachment in a collapsible channel. *Computers and Chemical Engineering*, 31:346–360, 2007.

[35] T.J. Pedley and X.Y. Luo. Modeling flow and oscillations in collapsible tubes. *Theoretical and Computational Fluid dynamics*, pages 277–294, 1998.

[36] X.Y Luo and T.J. Pedley. A numerical simulation of unsteady flow in two dimensional collapsible channel. *J. Fluid Mechanics*, 314:191–225, 1996.

[37] M.E. Rosar and S.P. Charles. Fluid flow in collapsible elastic tubes:a three dimensional numerical model. *New York J. Mathematics*, 2001.

[38] P. Alstrom, V. M. Eguluz, M. Colding-Jorgensen, F. Gustafsson, and N. Holstein-Rathlou. Instability and "sausage-string" appearance in blood vessels during high blood pressure. *Physical Review Letters*, 82(9):1995–1998, March 1999.

[39] J. Harris. *Rheology and non-Newtonian flow*. Longman Inc.,, New York, U.S.A., 1 edition, 1977.

[40] S.A. Berger, W. Goldsmith, and E.R. Lewis. *Introduction to Bio Engineering*. Oxford university press, New York, NY, 1996.

[41] F. Lurie, R. L. Kistner, B. Eklof, and D. Kessler. Mechanism of venous valve closure and role of the valve in circulation: A new concept. *J. Vascular Surgery*, 38(5):955–961, 2003.

[42] A.J Fenlon. *Mathematical model for flexible leaflet heart valves*. PhD thesis, University of Leeds, Leeds,England, 1999.

[43] J. Corden. *The fluid mechanics and leaflet dynamics of the Leeds polyurethane trileaflet heart valve*. PhD thesis, University of Leeds, Leeds,England, 1995.

[44] P.S. Bemmelen, G. Bedford, K. Beach, and D. E. Strandness. Quantitative segmental evaluation of venous valver reflux with duplex ultrasound scanning. *J. Vascular Surgery*, 10(4):425–431, October 1989.

[45] S. Raju, C. A. Hudson, R. Fredericks, P. Neglen, A.B. Greene, and E.F. Meydrech. Studies in calf venous pump function utilizing a two-valve experimental model. *Eur. J. Vascular and endovasclualr surgery*, 17:521–532, June 1999.

[46] J.J. McCaughan, D.B. Eash, L.P. Edgcomb, and H.E. Garrett. In vitro observations of greater saphenous vein valves during pulsatie and nonpulsatile flow following lysis. *J. Vasc. Sura.*, 1:356–361, 1984.

[47] Z.J. Huang, S. Merkle, C.L. Abdallah, and J.M. Tarbell. Numerical simulation of unsteady laminar flow through a tilting disk heart valve: prediction of vortex shredding. *J. Biomechanics*, 4:391–402, 1994.

[48] T.H. Reif and M.C. Huffstutler Jr. Design considerations for the omniscience pivoting disc cardiac valve prosthesis. *Int. J. Artif. Organs*, 6:131–138, 1983.

[49] C.D. Buescher, B. Nachiappan, J. Brumbaugh, K. A. Hoo, and H. F. Jansen. Experimental studies of the effects of abnormal bicuspid valves on fluid flow. *Bio Technology in Progress*, 21, 2005.

[50] R. Chiesa, E.M. Marone, C. Limoni, M. Volont, E. Schaefer, and O. Petrini. Effect of chronic venous insufficiency on activities of daily living and quality of life: correlation of demographic factors with duplex ultrasonography findings. *Angiology*, 58(4):440–449, 2007.

[51] O. E. Jensen. An asymptotic model of viscous flow limitation in a highly collapsed channel, October 1997.

[52] O. E. Jensen and M. Heil. High frequency self -excited oscillations in a collapsible-channel flow. *J. Fluid Mechanics*, 481:235–268, 2003.

[53] X.Y Luo and T.J. Pedley. The effects of wall inertia on flow in a two-dimensional collapsible channel. *J. Fluid Mechanics*, 363:253–280, 1998.

[54] J. V. White, M. L. Katz, P. Cisek, and J. Kreithren. Venus outflow of the leg: Anatomy and physiologic mechanism of the plantar venous plexus. *J. Vasc. Sura.*, 24:819–824, 1996.

[55] M.J. Piovoso, K.A. (Hoo) Kosanovich, and R.K. Pearson. Monitoring process performance in real-time. In *Proc. American Automatic Control Conf*, volume III, pages 2359–2363, June 1992.

[56] E.C. Zachmanoglou and W.T. Dale. *Introduction of partial differential equations with applications*. The William and Wilkins company, Baltimore, MD, 1976.

[57] X. Y. Luo. Steady and unsteady flow in collapsible tube. *Advances in Biomechanics*, 20:192–199, June 2001.

[58] T.J. Pedley and T.W. Lowe. Computation of stoke flow in a channel with a collapsible segment. *J. Fluids and Structures*, 9:885–905, 1995.

[59] N. S. Wijeratne and K.A. Hoo. Non-newtonian fluid flow model of blood flow around venous valves. *submitted to Journal of Biomechanical Engineering*, 2007. under review.

[60] B.A.Finlayson. *Nonlinear Analysis in Chemical Engineering*. McGraw-Hill, 1980.

[61] P.S. Bemmelen, K. Beach, G. Bedford, and D. E. Strandness. The mechanism of venous valve closure. *Arch. Surgery*, 125:617–619, May 1990.

[62] F.J.H. Gijsen, F.N. Van De Vosse, and J.D. Janssen. The influence of non-newtonian properties of blood on the flow in large arteries:steady flow in a carotid bifurcation model. *Journal of Biomechanics*, 32:601–608, 1999.

[63] A.L. Zydney, J.D. Oliver III, and C.K.Colton. A constitutive equation for the viscosity of stored red cell suspensions:effect of hematocrit, shear rate, and suspending space. *Journal of Rheology*, 35(8):1639–1680, November 1991.

[64] J.A. Long, A. Ündar, K.B. Manning, and S. Deutsch. Viscoelsaticity of pediadtic blood and its implications for the testing of a pulsatile pediatric blood pump. *ASAIO Journal*, 10:563–566, 2005.

[65] D. Quemada. Rheology of concentrated disperse systems and minimum energy dissipation principle. 1. viscosity -concentration relationship. *Rheol. Acta*, 16:82–84, 1977.

[66] G.R Cokelet. *Handbook of Bioengineering*, chapter The Rheology and Tube Flow of Blood. McGraw-Hill,New York.

[67] S. De Grottela, K. Boomsma, and D. Poulikakos. Computational simulation of a non-newtonian model of the blood separation process. *Artificial Organs*, 29(12):949–959, 2005.

[68] C. D. Buescher, K.A. Hoo, and H. F Janssen. Experimental characterization of in vitro veins and venous valve tissue. AICHE, 2007. Poster Presentation to American Institute of Chemical Engineers National Meetings.

[69] R.C. Gonzalez and R.E. Woods. *Digital Image Processing*. Prentice Hall,Inc., Upper Saddle River,New Jersey, 07458, 2002.

[70] J.S. Ackroyd, M. Pattision, and N.L. Browse. A study of the mechanical properties of fresh and preserved human femoral vein wall and valve cusps. *Br.J. Surg.*, 72:117–119, February 1985.

[71] K. Cho, W. Kolch, and O. Wolkenhauer. Experimental design in systems biology based on parameter sensitivity analysis using a monte carlo method: A case study for the tnf$\alpha$ - mediated nf-$\|\beta$ signal transduction pathway. *Simulation*, 79(12):726–739, 2003.

[72] D. Basmadjian. The hemodynamic and embolizing forces acting on thrombi- ii the effect of pulsatile blood flow. *J. Biomechanics*, 19(10):837–845, 1986.

[73] J. Belytschko and J. Kennedy. Finite element approach to pressure wave attenuation by reactor fuel sub-assemblies. *J.Press.Technol.*, pages 172–175, 1975.

[74] R.M. Berne and M.N. Levy. *Cardiovascular Physiology*. Mosbe, St. Louis, MO, 7th edition, 1997.

[75] C.D. Bertram. Unstable equilibrium behavior in collapsible tubes. *J. Biomechanics*, 19(1):61–69, 1986.

[76] C.D. Bertram and M.D. Shepperd. Prediction and measurement of the area-distance profile of collapsed tubes during self-excited oscillation. *J. Fluid and Structures*, 8:637–660, 1994.

[77] C.D. Bertram and N.S.J. Elliott. Aqueous flow limitation in uniform collapsible tubes: Multiple flow-limited flow rates at the same pressure drop and upstream transmural pressure. volume 50, pages 383–384. ASME, 2001.

[78] B.S. Brook and T.J. Pedley. A model for time-dependent flow in (giraffe jugular) veins: uniform tube properties. *J. Biomechanics*, 35:95–107, 2002.

[79] A. Caggiati, M. Phillips, A. Lametschwandtner, and C. Allegra. Valves in small veins and venules. *European Journal Of Vascular And Endovascular Surgery*, 32(4):447–452, October 2006.

[80] H.C. Chang and E.A. Demekhin. *Complex Wave Dynamics on Thin Films*. Elsevier Science Ltd., 2002.

[81] C. P. Cheng, D. Parker, and C. A. Taylor. Quantification of wall shear stress in large blood vessels using lagrangian interpolation functions with cine phase-contrast magnetic resonance imaging. *Annals of Biomedical Engineering*, 30:1020–1032, 2002.

[82] S.A. Conard and A. Bidini. Finite element mathematical model of fluid and solute transport in hemofiltration membranes. In *Proceedings of 25$^{th}$ Annual International Conference of the IEEE EMBS*, Cancun,Mexico, September 2003. IEEE.

[83] J. Crank. *Free and moving boundary problems*. Clarendon press,Oxford, New York, NY, 1994.

[84] G. Dai, P. Gertler, and R. D. Kamm. The effects of external compression on venous blood flow and tissue deformation in the lower leg. *J.Biomechanical Engineering*, 121:557–564, December 1999.

[85] E.A. Demekhin. *Instability and Nonlinear Waves in Thin Films of Viscous Films*. PhD thesis, Univ. Moscow, 1990. Academic Degree Doctor of Mathematics and Physics.

[86] D.V. Djordjević. On the fluid flow over the compliant wall. *Scientific j. Facta Universitatis*, 2(10):1219–1232, 2000.

[87] J. Donea, P. Fasoli-Stella, and S. Giuliani. Finite element solution of transient fluid structure problems in lagrangian co-ordinates. volume 3, pages 1427–1435, 1976. Proceedings of the international meeting of fast reactor safety and related physics.

[88] J. Donea, S. Giuliani, and J. Halleux. An arbitrary lagrangian-eulerian finite element method for transient dynamic fluid-structure interactions. *Comput. Methods Appl. Mech. Engrg.*, 33:689–723, 1982.

[89] G. Dubini, R. Literalists, and R. Fumero. Computational fluid dynamics of artificial heart valves. *Cardiovascular implants*, 14(6):338–342, 1991.

[90] K. Demount, J.M.A. Sticken, J. Viceregents, E.N. Van De Rose, and P.R. Verdonck. Validation of fluid-structure interaction model of a heart valve using dynamic mesh method in fluent. *Computer methods in Biomechanics and Biomedical Engineering*, 7(3):139–146, June 2004.

[91] J.E. Flaherty, J.B. Keller, and S.I. Rubinow. Post buckling behavior of elastic tubes and rings with opposite sides in contact. *SIAM J. Applied Mathematics*, 23(4):446–455, 1972.

[92] C. Frederiksen and A. Watts. Finite element method for time-dependent incompressible free surface flow. *J.Comp.Phys.*, 39:282–304, 1981.

[93] Y.C. Fung. *Biomechanics:Mechanical Properties of Living Tissues*. Springer-Verlag, New York, NY, 2 edition, 1993.

[94] F.J.H. Gijsen, E. Allanic, F.N. Van De Vosse, and J.D. Janssen. The influence of non-newtonian properties of blood on the flow in large arteries:unsteady flow in a 90°*curvedtube*. *Journal of Biomechanics*, 32:705–713, 1999.

[95] D.J. Griffiths. Steady fluid flow through veins and collapsible tubes. *Med. & Biol. Eng.*, 9:597–602, 1971.

[96] J. De Hart, G.W.M. Peters, P.J.G. Schreurs, and F.P.T Baaijens. A two-dimensional fluid-structure interaction model of aortic valve. *Journal of Bio mechanics*, 33:1079–1088, March 2000.

[97] S. Hayashi, T. Hayase, and H. Kawamura. Numerical analysis for stability and self excited oscillation in collapsible tube flows. *J. Biomechanical Engineering*, 120:468–475, August 1998.

[98] C. Hirt and B. Nichols. Volume of fluid vof method for dynamics of free surface boundaries. *J. Computational Physics*, 39:210–225, 1981.

[99] G. A. Holzapfel and R. W. Ogden. *Mechanics of Biological Tissue*. Springer-Verlag, Berlin Heidelberg, Germany, 2006.

[100] O. E. Jensen and T. Pedley. The existence of steady flow in a collapsible tube. *J. Fluid Mechanics*, 206:339–374, 1989.

[101] O. E. Jensen. Instabilities of flow in a collapsible tube. *J. Fluid Mechanics*, 220:623–659, 1990.

[102] J.P. Ku, M.T. Draney, F.R. Arko, W.A. Lee, F.P. Chan, N. J. Pelc, C.K. Zarins, and C.A Taylor. In vivo validation of numerical prediction of blood flow in arterial bypass grafts. *Annals of Biomedical Engineering*, 30:743–752, 2002.

[103] R.D. Kamm. Bioengineering studies of periodic external compression as prophylaxis against deep vein thrombosis-part i : Numerical studies. *Journal of Bio Mechanical Engineering*, 104:87–95, 1982.

[104] M. Kleiber. *Incremental finite element modeling in non-linear solid mechanics*. Chichester, West Sussex, England : E. Horwood, 1989.

[105] D. Lee, A. H. Abolfathi, G. A. DeLaria, T. J. Phifer, A. S. Nashef, and R.C. Quijano. In vitro testing of venous valves. *Trans. Amer. Soc. Artif. Intern. Organs*, 37:266–268, 1991.

[106] J. Liandart, V. Perrier, and P.H. Tchamitchain. Numerical resolution of nonlinear partial differential equations using wavelet approach. pages 227–238. 1989.

[107] E. Lillberg, R. Kamakoti, and S. Wei. Computation of unsteady interaction between viscous flows and flexible structure with finite inertia. volume 142, pages 1–17. American Institute of Aeronautics and Astronautics,Inc., 2000.

[108] J.C. Lin, M.D. Iafrati, T.F. O'Donnell, J.M. Estes, and W.C. Mackey. Correlation of duplex ultrasound scanning-derived valve closure time and clinical classification in patients with small saphenous vein reflux: Is lesser saphenous vein truly lesser? *Journal Of Vascular Surgery*, 39(4):1053–1058, May 2004.

[109] X. Y. Luo, Z. X. Cai, and T. J. Pedley. Modeling flow in a collapsible tubes. volume 50, pages 83–84. ASME, 2001.

[110] Y. Matsuzaki, T. Ikeda, T. Kitagawa, and S. Sakata. Analysis of flow in a two-dimensional collapsible channel using universal tube law. *J. Biomechanical Engineering*, 116:469–476, 1994.

[111] Y. Matsuzaki and T. Matsumoto. Flow in a -two dimensional collapsible channel with rigid inlet and outlet. *J. Biomechanical Engineering*, 120:181–184, August 1989.

[112] A.H. Moreno, A.I. Katz, L.D. Gold, R.V. Reddy, and M. Tech. Mechanics of distention of dog veins and other very thin walled tabular structure. *Circulation Research*, XXVII:1069–1080, December 1970.

[113] J.A. Moore, D. A. Steinman, S. Prakash, K.W. Johnston, and C.R. Ethier. A numerical study for blood flow patterns in anatomically realistic and simplified end-to-side anastomoses. *J. Biomechanical Engineering*, 121:265–272, April 1999.

[114] L.B. Notowitz. Normal venous anatomy and physiology of the lower extremity. *Journal of Vascular Nursing*, XI:39–42, 1993.

[115] D.A. Olsen, R.D. Kamm, and A.H. Shapiro. Bioengineering studies of periodic external compression as prophylaxis against deep vein thrombosis-part ii: Experimental studies on simulated leg. *Journal of Bio Mechanical Engineering*, 104:96–106, December 1982.

[116] M. S. Olufsen. Structured-tree out flow condition for blood flow in larger systemic arteries. *American j. Physiological*, 276:H257–H268, 1999.

[117] M. S. Olufsen, C. S. Peskin, W. Y. K. Pedersen, A. Nadim, and J. Larsen. Numerical simulation and experimental validation of blood flow in arteries with structured-tree outflow conditions. *Annals of Biomedical Engineering*, 28:1281–1299, 2000.

[118] M. S. Olufsen, A. Nadim, and A.L. Lewis. Dynamics of cerebral blood flow regulation explained using a lumped parameter model. *American J. Physiol regulatory integrative comp Physiol*, 282:R611–R622, 2001.

[119] L. Pascarella, G.W. Schmid-Schonbein, and J. Bergan. An animal model of venous hypertension: The role of inflammation in venous valve failure. *Journal Of Vascular Surgery*, 41(2):303–311, February 2005.

[120] S. Petkova, A. Hossain, J. Naser, and E. Palombo. Cfd modeling of blood flow in portal vein hypertension with and without thrombosis. In *Third International Conference on CFD in the Mineral and Processes Industries*, pages 10–12, Melbourne,Australia, December 2003. CSIRO.

[121] M.N. Phillips, G.T. Jones, A.M. van Rij, and M. Zhang. Micro-venous valves in the superficial veins of the human lower limb. *Clinical Anatomy*, 17(1):55–60, January 2004.

[122] S. Raju, R. Fredericks, P. Lishman, P. Neglen, and J. Morano. Observations on the calf venous pump mechanism: Determinants of postexercise pressure. *Journal of Vascular Surgery*, 17:459–469, 1993.

[123] S. Raju, A.B. Green, R.K. Fredericks, P.N. Neglen, C.A. Hudson, and K. Koenig. Tube collapse and valve closure in ambulatory venous pressure regulation: studies with mechanical model. *J.Endovasclualr surgery*, 5:542–552, 1998.

[124] H. Satoru, T. Hayase, and Y. Miura. Stability analysis of collapsible tube flow.

[125] Z.I. Stefanov, C. D. Buescher, K. A. Hoo, and H. F. Jansen. Stereo-imaging of collapsible tubes with embedded one-way bicuspid membrane structures. *Biomedical Imaging*, 2003. Submitted.

[126] W.M. Swanson and R.E Clark. Dimensions and geometric relationships of the human aortic valve as a function of pressure. *Circulation Research*, 35:871–882, 1974.

[127] S.A. Unhale, G. Marino, and S. Parameswaran. A one dimensional model to predict steady flow through a collapsible tube. *Intl J. Computational Science*, 0(0):1–12, 1999.

[128] S. Wei, M.M. Francois, and H.S. Udaykumar. Computational moving boundary problems in engineering and biomechanics. In *The 7th national computational fluid dynamics conference*, pages 1–8, August 2000.

[129] R.L.R. Wesly, R.N. Vaishnav, J.C.A. Fuchs, D.J. Patel, and J.C. Greenfiled Jr. Static linear and non linear elastic properties of normal and arterialized venous tissue in dog. *Circulation Research*, 37, October 1975.

[130] N. M. Wilson, D. L. Rutt, and N. L. Browse. In situ venous valve construction. *British J. of Sura.*, 78:595–600, 1991.

[131] F.M. White. *Fluid Mechanics*. McGraw-Hill, 4 edition, 1999.

[132] Zhong-shi Wu, Jing-chao Zhang, and Cheng Duan. Morphologic and hydrodynamic characteristics of bovine jugular venous conduit with valves. *Hunan Yike Daxue Xuebao*, 28(3):298–300, June 2003.

[133] Y.L. Yeow, S.R. Wickramasinghe, Y. Leong, and B. Han. Model- independent relationship between hematocrit, blood viscosity, and yield stress derived from couette viscometry data. *Biotechnology in Progress*, 18:1068–1075, 2002.

[134] D. Zheng. Phenomenological modeling of venous and valvular hemodynamics. Internal report, Texas Tech University, Dept. Of Chemical Engineering, P.O.Box 3121,Lubbock,TX,U.S.A, 2001.